ISPH Modelling of Solitary Wave Interaction with Permeable Beaches

Chiaki Tsurudome

St Edmund's College

UNIVERSITY OF CAMBRIDGE
Department of Engineering

January 2020

This thesis is submitted for the degree of Doctor of Philosophy.

Declaration

This thesis is the result of my own work and includes nothing which is the outcome of work done in collaboration except as declared in the Preface and specified in the text. It is not substantially the same as any that I have submitted, or, is being concurrently submitted for a degree or diploma or other qualification at the University of Cambridge or any other University or similar institution except as declared in the Preface and specified in the text. I further state that no substantial part of my thesis has already been submitted, or, is being concurrently submitted for any such degree, diploma or other qualification at the University of Cambridge or any other University or similar institution except as declared in the Preface and specified in the text. It does not exceed the prescribed word limit for the relevant Degree Committee.

Abstract

ISPH Modelling of Solitary Wave Interaction with Permeable Beaches

Chiaki Tsurudome

Coastal areas are vulnerable to natural disasters such as storm surges and tsunamis. Dykes, wave-absorbing blocks, and forests, are typical solutions to mitigate coastal disasters. In coastal engineering, these protections and beaches are considered as porous media. Accurate prediction of wave motion around porous structures is necessary for the effective design of stable and durable coastal protections. Although mesh-based methods have been conventionally utilised to simulate porous flows, they often suffer from numerical diffusion due to large deformation of a grid. Mesh-free methods are more suitable for simulating violent free-surface flows. Smooth Particle Hydrodynamics (SPH) is a meshless and particle method, which can be applied to simulations of moving free surface flows with porous structures.

This thesis presents an incompressible SPH (ISPH) model that can simulate violent porous flows. In the present ISPH model, dummy particles were used to implement porous structures. These dummy particles have information on porosity, mass and density. A new water-porous interface was proposed so that the model does not need any transition zone at the water-porous boundary. Porosity was defined linearly by the amount of porous particles included in the support domain of a target particle. A new free surface condition was presented to search for free surface particles correctly even if they exist in a porous region. To obtain smooth pressure fields, the source term of the pressure equation was modified with the higher-order source term. The present ISPH model was validated

through the simulation of dambreaking with a porous block. The simulation results agreed strongly with the experiment.

To investigate wave interactions with porous media, the present ISPH model was applied to simulations of solitary wave runup on permeable slopes. In these simulations, triangle and parallelogram porous structures with various mean grain sizes were focused. Two different scale slopes were considered to generate both nonbreaking and breaking waves. For nonbreaking waves, runup height decreased nearly linearly as the mean grain size of a permeable slope became logarithmically larger. When the grain size became larger, runup height on the thickest parallelogram porous structure was smaller than that on the thinner parallelogram porous media. This phenomenon indicates that the shape and grain size of porous structures can be essential factors to determine runup height of nonbreaking waves. Meanwhile, for breaking waves, nearly the same runup height was obtained in any shape of permeable slopes even with the large grain size of porous media. This result implies that the mean grain diameter predominantly determines runup height of breaking waves.

All the above-mentioned results demonstrate that the present ISPH model is capable of simulating violent porous flows and investigating wave interactions with porous structures. The findings in this thesis can contribute to a better understanding of permeability effects on coastal disaster mitigation and to more accurate prediction of runup height on porous structures.

Acknowledgement

Completing this study was not straightforward for me. I had to learn the basics of the SPH method and Fortran codes when starting this study, because I had no experience of using mesh-free methods. I am grateful to everyone who helped and supported me during my PhD study.

First and foremost, I would like to express the deepest appreciation to my supervisor, Dr Dongfang Liang, for his constant support and guidance on the research project. I especially appreciate his suggestions for model applications and insights on fluid-soil mechanics. His encouragement kept me working on the PhD study and helped me to complete it.

I would like to express my gratitude to Prof Abbas Khayyer at Kyoto University, for technical discussions, where I learnt some essential principles and improved methods of SPH. I also would like to thank Prof Hitoshi Gotoh for his feedback when I published the proceeding papers. I am deeply grateful to Dr Yuma Shimizu for discussions on porous media implementation.

The past and present members in the geotechnical research group have helped and encouraged me a lot. I would like to thank all of them.

Last but not the least, I would like to express my sincere gratitude to my family. My parents strongly encouraged me for over three years. My brother kindly funded my PhD

study as well as my parents. He was considerate to me living away from home. Without

my family's support and love, this thesis could not be completed.

Contents

List of Figures

List of Tables

Nomenclature

$\boldsymbol{u}$	velocity
t	time
P	pressure
$\boldsymbol{f}$	external force
$\boldsymbol{g}$	gravity
$\Delta\boldsymbol{u}_*$	velocity increment
Δt	time increment
$\Delta\boldsymbol{u}_{**}$	velocity increment
$\overline{S_{\iota J}}$	SPS strain rate
k	SPS turbulence kinetic energy
Cs	Smagorinsky constant
Δx	particle spacing
$|\bar{S}|$	local strain rate
A($\boldsymbol{r}$)	arbitrary function
$\boldsymbol{r}$	position vector
W	kernel function
h	smoothing length
V	volume
m	mass
q	relative distance
X	position of a wave paddle
H	wave amplitude

h_0	mean water depth
c	wave phase speed
$f(\theta)$	wave function
S	total stroke of paddle movement
C	Courant number
Cm	amplitude
k_m	a number of waves
G	ratio of the amplitudes
d_0	initial particle spacing
$\boldsymbol{R}$	resistance force
Kp	permeability
Nw	porosity
Dc	mean grain diameter
Nw_i	apparent porosity of the particle i
m_p	mass of porous particles
b	free surface coefficient
R	maximum runup height
M_F	wave momentum flux
M	coefficient for wave momentum flux
N	coefficient for wave momentum flux
t^*	nondimensional time
k_1	coefficient for runup height law
k_2	coefficient for runup height law
k_3	coefficient for runup height law

R_s		runup height on a solid slope

Greek Symbols

ρ		density
ν		laminar kinetic viscosity
ρ_0		initial fluid density
$\vec{\tau}$		SPS stress tensor
ν_t		turbulence eddy viscosity
δ_{ij}		Kronecker delta
Ω		domain
Φ		arbitrary physical property
κ		scaling factor
α		dimension
η		wave elevation
β		outskirts decay coefficient
ε		relative wave height
μ		dynamic viscosity
ρ_w		density in a pure fluid region
ρ_p		density of porous particles
ρ_w		density of a pure fluid
γ		combination ratio
φ		slope angle

Acronyms

computational fluid dynamics	CFD
Courant-Friedrichs-Levy	CFL
Discrete Element Method	DEM
Distinct Element Method	DEM
Dynamic Stabilized	DS
Error-Compensating Source	ECS
Finite Different Method	FDM
Finite Element Method	FEM
Finite Volume Method	FVM
grid-scale	GS
Higher-order Source	HS
incompressible Smoothed Particle Hydrodynamics	ISPH
Lagrangian Blocks on Eulerian Mesh	LBEM
Large Eddy Simulation	LES
Marker and Cell	MAC
Material Point Method	MPM
Navier-Stokes	NS
Particle in Cell	PIC
Poisson Pressure Equation	PPE
Reynolds Averaged Navier-Stokes	RANS
sub-grid scale	SGS
successive order-relaxation	SOR
Smoothed Particle Hydrodynamics	SPH

Sub Particle Scale   SPS

Stanford University Modified Marker and Cell   SUMMAC

Volume-average Reynolds Averaged Navier-Stokes   VARANS

Volume of Fluid   VOF

weakly compressible Smoothed Particle Hydrodynamics   WCSPH

Chapter 1   Introduction

1.1   Coastal disasters and defences

More than half of the world's population today resides in urban cities, and the majority of them are located in coastal zones (Glasow et al. 2013). Figure 1.1 shows that coastal zones in the world are crowded with urban cities in 2018 (United Nations Development of Economic and Social Affairs). Coastal zones are inseparable from human lives as these areas provide many benefits such as marine food and mineral resources. Moreover, coastal zones offer areas for socio-economic activities, marine leisure, and transportation.

Figure 1.1 Map of the world population in 2018 (https://population.un.org/wup/Maps/)

Conversely, coastal zones are vulnerable to natural hazards. Nearly 60% of cities with 300,000 inhabitants are highly likely to suffer from at least one of six natural hazards: cyclones, droughts, floods, earthquakes, landslides and volcanic eruptions (United

1

Nations, 2018). Natural hazards sometimes become severe disasters in coastal areas. One of the most catastrophic recent events was the Sumatra Tsunami. An earthquake of Mw 9.3 struck Sumatra on 26 December 2004, causing massive tsunamis (Yeh et al. 2005). These tsunamis hit Indonesia, Thailand, Malaysia, Myanmar, Bangladesh, India, Sri Lanka, Maldives, and African countries; the total number of the dead and missing people is over 226,000. Another extraordinary event was Hurricane Katrina. In August 2005, extremely high waves and storm surge caused flooding and loss of life throughout the southern part of Louisiana and Mississippi (Ebersole et al. 2010). Inundation was particularly severe in the coastal area of St Bernard Polder in New Orleans. Similarly, a Mw 9.0 earthquake occurred off the Pacific coast of Tohoku, Japan on 11 March 2011. The resulting tsunami inundated over 400 km^2 of land with more than 20,000 people killed or missing (Mori et al. 2011). These examples stress the importance of effective management of coastal areas and mitigation plans for disasters.

Coastal forests are a possible solution to mitigate natural disasters. The vegetation on the coast of Kuji, for example, has successfully attenuated the Tohoku Great Tsunami in 2011 (Tsuchiya, 2013). When tsunami waves reached the coastline, the trees split them into several smaller waves. The flows propagating between the trees dissipated their energies, providing that a narrow path of flows is a crucial concept in disaster mitigation. Another possible solution is to construct coastal protections, such as dykes, rubble-mound breakwaters, and revetments. Coastal dykes are structures protecting land areas from flooding and overflowing waves. They are built with fine materials such as sand, silty sand and clay, and thus the permeability of the dykes is low (Burcharth and Hughes, 2003). The seaside slope is generally mild to reduce wave runup and impact. The surface of the

dyke is often armoured with grass, asphalt, stones or concrete slabs (Figure 1.2). Seawalls are constructed to prevent wave overtopping and to protect low-lying areas from storm surges and waves. These walls are either vertical structures with concrete and steel or sloping structures with concrete slabs and stone rubble (Figure 1.3). Revetments are onshore structures protecting the shoreline from erosion. They consist of a cladding of stone, concrete or asphalt (Figure 1.4). In the technical context, revetments are often not distinguished from seawalls. Detached breakwaters are usually rubble-mound structures and concrete caisson covered with rock or concrete armour units, and wave-absorbing blocks are placed with them (Figure 1.5). While approaching the shore, waves run up a slope of the seabed, and their height increases as water become shallow. Finally, waves break when they reach coastal structures, and wave energies are dissipated efficiently because of pores. However, coastal structures can be damaged by wave attacks, and they sometimes fail to dissipate wave energies. Oumeraci (1994) listed and reviewed faulty structures in several countries such as India, Spain, and Italy. The causes of failure include breaking waves and wave overtopping, scouring, and erosion of seabed. Shimizu (2011) examined the coastal dykes in Taro that were destroyed when Tohoku Great Tsunami reached the eastern coastline of Japan. The seawalls were demolished because of wave overtopping and backwash. In coastal engineering, accurate prediction of wave motion around structures is necessary for the effective design of stable and durable coastal protections.
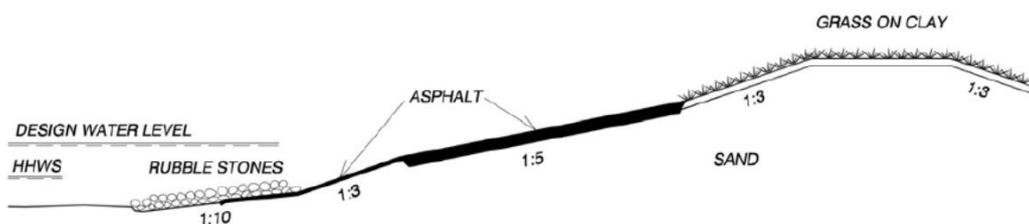
Figure 1.2 Example of sea dyke (Burcharth and Hughes, 2003)

3
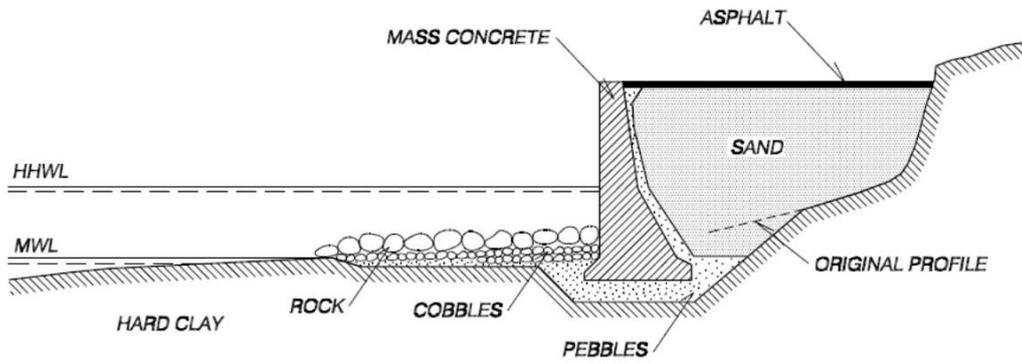
Figure 1.3 Example of a vertical seawall (Burcharth and Hughes, 2003)
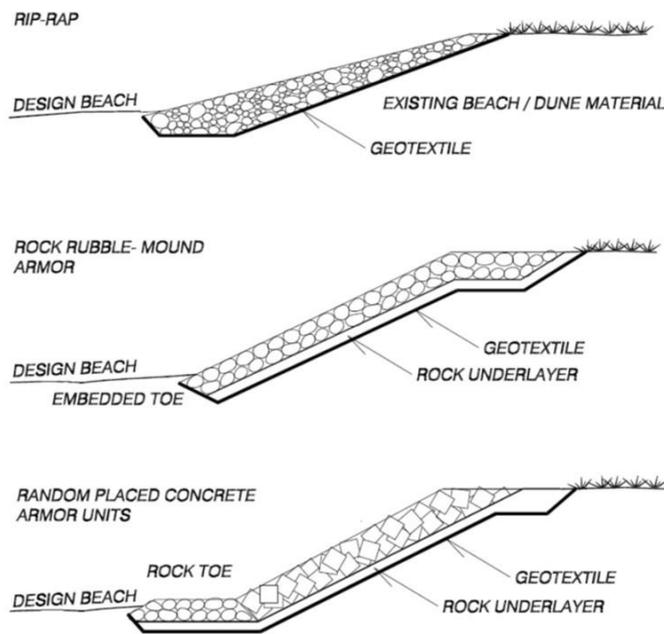
Figure 1.4 Examples of revetments (Burcharth and Hughes, 2003)
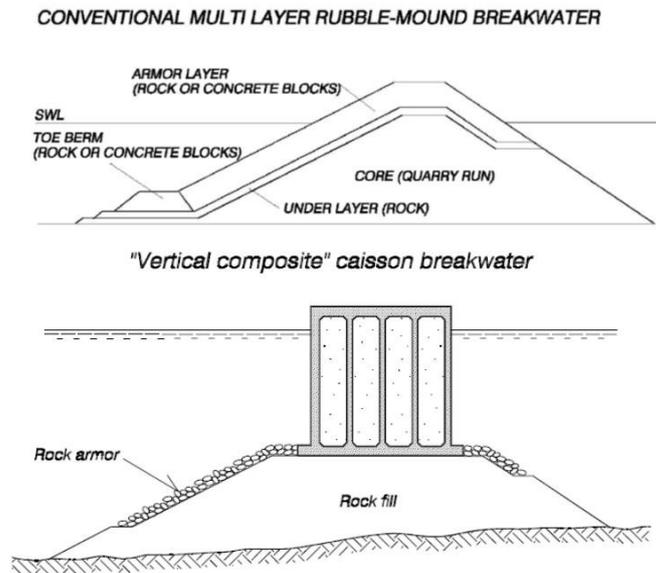
Figure 1.5 Examples of breakwaters (Burcharth and Hughes, 2003)

Studies on flows through permeable structures were traditionally conducted according to empirical laws and hydraulic experiments. Owing to the advent and advancement of computing technology in the past few decades, numerical modelling is now utilised where equations on porous flows are numerically solved, and flows are tracked on a fixed grid. However, since waves attacking porous media have a violently moving free surface, conventional mesh-based methods suffer from numerical diffusions due to grid distortion. Smoothed Particle Hydrodynamics (SPH), one of the mesh-free methods, overcomes the drawbacks of mesh-based methods because of the sets of particles describing fluids. The Lagrangean scheme of SPH modelling enables the simulation of complex flows through porous structures. Many researchers have thus attempted to predict wave motion around porous structures using the SPH method. Nevertheless, these studies are based on wave propagation on a solid slope with porous media. This solid slope has smooth and impermeable properties, which is idealised, but not practicable.

This study focuses on solitary wave propagation on permeable beach. A slope is considered as porous media based on the assumption that actual beaches, in reality, consist sediment, gravel, and soil. Those materials are classified by the grain size as listed in Table 1.1 (Iso, 2017). Generally, sandy beaches are not immovable unless they are stabilized by vegetation. Very coarse soil, such as cobbles and boulders, may be static except in large storms and massive waves. The porous materials in this thesis are assumed as fixed and movable sediment is not included to focus on the wave motion. An impermeable slope covered with some porous layers is also examined. This structure describes coastal dykes, revetments, sloping walls or breakingwaters protected with wave-absorbing blocks. Considering the materials of coastal defences and beaches, the grain size of porous media in this thesis ranges from 0.20 mm to 200 mm. Wave interactions with porous media are investigated using the incompressible SPH (ISPH) method. This work aims to predict wave motion and runup on porous beaches more accurately, improving the assessment and design of coastal protections.

Table 1.1 International scale of soil (ISO 14688-1:2017)

Soil group	Particle size fractions	Grain size [mm]
Very coarse soil	Large boulder	630-
	Boulder	200-630
	Cobble	63-200
Coarse soil	Gravel	2.0-63
	Sand	0.063-2.0
Fine soil	Silt	0.002-0.063
	Clay	-0.002

1.2   Aims

The present study aims to develop an ISPH model that can accurately predict accurate pressure fields and solitary wave runup height. The present work also examines the relationship between solitary wave runup height and physical properties of porous media. The main contributions of this study are summarised as follows:

(1) Development of the ISPH model for porous flows: The original ISPH is improved so that it is able to simulate complex porous flows with smooth pressure fields. New treatment for a water-porous interface is presented. The new boundary condition for free-surface is also proposed.

(2) Numerical treatments in SPH implementation: Optimal choice of a kernel function, source term of pressure equation, and wave generation theory are investigated to obtain accurate pressure and solitary wave runup height.

(3) Simulation of solitary waves considering sand gravel or cobble beaches: Solitary wave propagation over permeable beaches is investigated using the improved ISPH modelling in two dimensions. The relationship between runup height, mean grain size and shape of porous media is analysed.

1.3   Thesis outline

The thesis is divided into seven chapters.

- Chapter 1 provides a brief background on the research topic and explains the motivation of the present study.

- Chapter 2 reviews the development history of porous flow studies and discusses the current issues in SPH modelling for porous flows.

- Chapter 3 explains governing equations, fundamental SPH formulae, and wave generation theories.

- Chapter 4 proposes the ISPH model to simulate porous flows and expounds some new techniques and boundary treatments. The model is validated through a dam breaking simulation.

- Chapter 5 presents the numerical simulations of solitary wave runup on a relatively steep slope. Runup laws are estimated from the results of runup height on a triangle permeable slope. Runup height on various porous layers between is compared.

- Chapter 6 discusses the solitary wave runup on a relatively mild slope. A runup law is obtained through the results of the triangle permeable slope cases. Runup height of breaking waves is discussed in detail.

- Chapter 7 summarises the entire work and provides some concluding remarks.

Chapter 2   Review of porous flow studies

2.1   Experimental and empirical studies

2.1.1   Empirical laws

Studies about water flows through porous media date back to the 19th century. Darcy (1856) formulated the law stating that the velocity of fluid in the ground is proportional to the hydraulic gradient. Many researchers and engineers tried to verify Darcy's law with experiments or hydraulic theories. While some cases of seepage flow satisfied the law, it was determined that Darcy's law is not applicable if porosity is large and the velocity of seepage flow is high - in other words, when the Reynolds number is large. Forchcheimer (1901) modified Darcy's law by adding a nonlinear term into the equation. Brinkman (1949) pointed out that a viscous stress tensor was not taken account in Darcy's law, and he added a viscous shearing stress term to the Darcy equation. After the 1960s, some experiments revealed that fluid propagating through mud or silt, that is, flows with a low Reynolds number, also do not satisfy Darcy's law (Yasuhara and Kaihotsu, 1981). To generalise for both steady and unsteady flows, a comprehensive law for non-Darcy flows has been investigated.

2.1.2   Experimental studies

In contrast to studies of seepage flows, the interaction between waves and porous media has became to be focused relatively recently. Savage (1953) is one of the earliest experimental studies to investigate wave height attenuation and energy losses due to bottom friction and percolation. Goda et al. (1975) performed some measurements of irregular waves to model seawalls with and without concrete block mounds. They proposed 12 diagrams for estimating overtopping rates based on their experimental results. To investigate wave damping, Özhan and Shi-Igai (1977) observed solitary waves of

9

various heights travelling over smooth and rough bottoms. They found that the friction factor depends on the instantaneous wave height even if the bottom is entirely rough. Sawaragi and Deguchi (1992) examined the applicability of the Forchheimer equation and conducted a number of steady-state and unsteady-state permeability tests to analyse wave damping over a permeable layer. They found that the wave attenuation can be predicted precisely when the incident wave has strong linearity. Sakakiyama and Liu (2001) focused on wave behaviour and turbulence flows in front of a caisson breakwater, covered with wave absorbing blocks and supported by a rubble mound. They concluded that turbulence is generated during a wave breaking process inside the armour layer. This generated turbulence significantly affects wave impacts and the scouring process in front of the breakwater.

The understanding of wave motion and its characteristics has been significantly improved because of advancement in measuring techniques. Nevertheless, although many experiments have been conducted and have shown apparent results, one of the major difficulties with laboratory experiments is the scale effect. Since the wavelength of a real tsunami can reach up to 20 kilometres in water shallower than 30 metres in depth, extremely long flumes at 1/100 to 1/200 scale are necessary to avoid distortion in the waveform. Another limitation of experimental studies is little flexibility. Wave flumes and laboratory equipment must be set up for each experimental case, which is costly and time-consuming. Numerical experiments using coastal protections at a real scale are also problematic since a long integration time is required. Recently, laboratory experiments with basic physical problems rather than specific problems, such as dam-breaking and

solitary wave propagation, have been conducted. Those results can be compared with simulations to validate numerical models.

2.2   Mesh-based methods
2.2.1   Numerical models

Sollitt and Cross (1972) proposed a general numerical model describing non-Darcy wave transmission through a permeable breakwater. They added inertial and nonlinear resistance force terms into the momentum equation. Based on their work, various numerical models have been proposed. For instance, Sulisz (1985) utilised a boundary-element method based on potential flow theory. They investigated wave reflection and transmission processes at permeable breakwaters. Similarly, Yu and Chwang (1994) applied linear potential theory to analyse wave motion through a two-layer porous structure. It has been pointed out, however, that potential theory cannot completely treat the breaking of a wave. Wurjanto and Kobayashi (1993) developed a numerical model based on the shallow water equations to investigate a wave reflection and runup on a permeable slope. Their model needs to calibrate the empirical parameters to obtain better agreement with measured results.

A more general model was developed by van Gent (1995), in which flows are divided into two equations for outside and inside porous media, and for each flow, the Navier-Stokes (NS) equations are applied. Additional force terms are added into the NS equations of porous flow. The coefficients of the porous force terms were obtained from van Gent's (1994) experiments. Later, Liu et al. (1999) proposed a model based on the Reynolds Averaged Navier-Stokes (RANS) equations. Similar to the van Gent (1995) model, the flows outside and inside porous structures are modelled separately: the RANS equations

11

are applied for the mean flow outside and spatially averaged NS equations for the flow inside. The authors modelled the turbulence field outside porous structures using an improved *k-ε* model. They assumed that the turbulence in a porous flow should be low, since the maximum intensity of turbulence depends on pore size, and the NS equations are averaged over a length scale, which is much larger than pore size. Therefore, the mean and average velocity and pressure fields of the outside flow are applied to the inside flow.

Following Liu et al. (1999), the NS equations model has been further developed and modified to investigate water-porous media interactions. Lara et al. (2006) simulated irregular wave interaction with submerged rubble-mound breakwaters based on the RANS model. Later, Lara et al. (2011) investigated solitary wave evolution over a porous step, including breaking and damping. Unlike the earlier models, Karunarathna and Lin (2006) presented a model which explicitly represents the flow resistance based on the Reynolds number to cover various porous flows. Wu et al. (2014) coupled Large Eddy Simulation (LES) and the RANS model, and they applied their model to produce three-dimensional simulations of the interaction between solitary waves and porous breakwaters. Hsu et al. (2002) enhanced Liu et al.'s (1999) model by using volume-average of RANS (VARANS) equations describing flows both inside and outside porous structures. This VARANS model was utilized by Wu and Hsiao (2013) to simulate solitary waves which propagate over a submerged permeable breakwater. del Jesus et al. (2012) and Higuera et al. (2014) extended the VARANS model to three-dimensional problems.

2.2.2   Free-surface tracking techniques

The numerical models mentioned in the previous section require an additional method to solve the equations and track a free surface. Traditionally, mesh-based approaches have been widely adopted in computational fluid dynamics (CFD). In mesh-based methods, a space containing fluid is divided into a grid, where governing equations are presented in a finite-difference form. Hence, physical properties are stored in each cell.

One of the most common mesh-based methods is the Marker and Cell (MAC) method developed by Harlow and Welch (1965). In MAC, the NS equations for a viscous incompressible flow are used in a finite-difference form. This method uses marker parcels to define a free surface. A cell without a marker means that there is no fluid, whereas a cell with markers next to an empty cell describes a free surface. A cell with a marker surrounded with marked cells represents fluid. Chan and Street (1970) improved the original MAC and proposed the Stanford University Modified MAC (SUMMAC) code, which is suitable for incompressible flows with a free surface. Sakai et al. (1987) applied the MAC method to simulate a violent free surface over a plunging breakwater. Huang et al. (2003) developed an approach based on unsteady two-dimensional NS equations to model the interaction between a solitary wave and a submerged breakwater, with free surface tracked by MAC and SUMMAC. Similarly, a solitary wave over porous beds was simulated by Huang et al. (2008) using the combination of MAC and SUMMAC methods. Huang et al. (2003) indicated that the fluid motion near the bottom would cause scouring in front of a breakwater. However, this water-soil interaction was not investigated at that time since it is not feasible to use MAC to describe soil displacement. Moreover, the

major drawback of the MAC method is the number of markers required in each cell to track a free surface accurately, which leads to significant computing time and load.

Hirt and Nichols (1981) developed the Volume of Fluid (VOF) method to reduce computational loads of MAC. In VOF, a function F is defined to represent the fractional volume of fluid occupying each cell. The function F becomes a unity value if a cell is fully occupied by fluid, whereas a free surface is represented by an F value between zero and one. By introducing an F function instead of markers, VOF is more efficient than MAC. The VOF method has been utilized to track a free surface and complex wave motions with structures. For instance, van der Meer (1992) succeeded in simulating plunging waves on coastal structures with VOF. Kawasaki (1999) developed a numerical model to simulate a breaking wave and investigated a wave deformation process using the VOF method.

In many simulations of porous flows, including Liu et al. (1999), a free surface was tracked by VOF and the models were validated. However, del Jesus et al. (2012) pointed out that the numerical resolution is an essential factor in such approaches and that lower resolutions cause uncertainty in wave discharge calculations when waves overtop structures.

As for the discretising schemes, Finite Difference Method (FDM), Finite Element Method (FEM), and Finite Volume Method (FVM) are widely used in CFD (Kumar et al. 2015). For instance, a computational domain is divided into small cells, and a central point of each cell, which is called "control volume", is defined in FVM. Unlike FDM and FEM,

differential equations are integrated over the control volume, and thus physical properties can be conserved. FVM allows users to utilise unstructured meshing, which can capture the surface boundary of objects, and adaptive mesh refinement (developed by Berger, 1982) can be coupled to track a sharp surface in high resolution (Jasak et al. 2000 and Liu and Hu, 2018). The mesh-based methods are free from the distortion of coordinate as long as their grid is fixed where governing equations are discretised. However, difficulties on meshing and numerical diffusion arise if boundaries are largely deformable, interfaces are violently moving, or there is a fragmentation of water (Kumar et al. 2015 and Khayyer et al. 2018). Jasak and Tukovic (2006) developed the moving-mesh unstructured FVM to simulate flows where domain shape changes at each time step. Although they tried to minimise mesh distortion effects and tested the method on a simple deformation case, Khayyer et al. (2018) pointed out that the inaccuracy and instability of the calculation in moving coordinate are problematic when the distortion is significant.

2.3   Mesh-free methods
2.3.1   Overview
Unlike the mesh-based methods, mesh-free methods do not require a grid for computation. They are instead based on the Lagrangian form of governing equations and those equations are discretised. A material is described by a set of particles which carry physical properties such as mass, density and velocity. For example, Distinct Element Method or Discrete Element Method (DEM) is a numerical method for computing the motions of a large number of particles. DEM was originally developed by Cundall (1971) for rock mechanics and improved by Cundall and Strack (1979). It has been widely applied to engineering problems such as granular flows (Renzo and Maio, 2004) and concrete cracks (Beckmann et al., 2012). Meanwhile, Material Point Method (MPM) is a numerical

technique which was developed by Sulsky (1994), based on the Particle In Cell (PIC) method (Harlow, 1964). In MPM, while physical properties are given to particles, referred to as material points, a background mesh is used to solve the momentum balance equation. MPM is suitable for simulating multi-phase interactions (Martinelli and Rohe, 2015). In CFD, Moving Particle Semi-implicit (MPS) and Smoothed Particle Hydrodynamics (SPH) are widely adopted. They are free from grid distortion and numerical diffusion due to the advection term (Gotoh et al. 2005). Generally, tens to hundreds of thousands of particles are needed to obtain satisfactory results in these methods. The calculation process must be done for each particle, and this causes a high computational load. The particle size needs to be uniform in the computational domain because of integral interpolation (see Chapter 3), and thus multi-resolution is challenging to reduce computation time (Gotoh, 2018). Consequently, mesh-free particle methods are more expensive than mesh-based methods, particularly in a domain at a large scale. In the following section, MPS and SPH are discussed.

2.3.2   MPS

The MPS method was developed by Koshizuka et al. (1995) and Koshizuka and Oka (1996) to simulate a free surface flow. Physical properties of one particle are approximated from those of the neighbouring particles using a weight function. The name "MPS" is derived from a semi-implicit algorithm to enforce the incompressibility of the flow. First, temporal velocity is calculated with the given sets of viscosity and gravity terms. After temporal velocity values are obtained, they are corrected by considering pressure terms and particle positions are updated.

Koshizuka et al. (1998) applied MPS to simulations of breaking waves on slopes and demonstrated its applicability to fluid-structure problems. Although artificial friction was observed in their simulations, which is derived from a disturbed motion of particles and causes errors, MPS has been utilized to simulate a violent free-surface flow. Gotoh and Sakai (1999) applied MPS to simulate waves breaking over a uniform slope, a permeable slope, and a vertical wall. Wave overtopping was investigated by Gotoh et al. (2005). In their simulations, the wave overtopping process produced by MPS agreed well with experimental data. They also proposed an improved listing system for searching neighbouring particles and succeeded in reducing the computational load. However, Khayyer and Gotoh (2009) pointed out that MPS was not suitable for predicting wave impacts due to pressure fluctuations. To address this, they modified the MPS formulations by introducing a new pressure gradient term, considering conservation of momentum, and adding a stabilising term to the Poisson Pressure Equation (PPE). The proposed MPS method demonstrated it was capable of estimating wave impacts.

On another track, Gotoh et al. (2001) extended the original MPS to include a turbulence model. They referred the LES concept (Rogallo and Moin, 1984) and proposed the Sub-Particle Scale (SPS) turbulence model, which calculates flow and turbulence on two scales: the particle scale (PS) and the SPS. Gotoh and Sakai (2006) presented the applicability of the SPS-coupled MPS to simulations of breaking waves. They also modelled gas-liquid and solid-liquid two-phase flows including sediment transport and floating bodies problems. The model of fluid-structure interactions was further developed by Hwang et al. (2014). They simulated a dam breaking with an elastic gate accompanying a violent sloshing flow. Fu and Jin (2018) focused on channel flows over

a porous bed with MPS. They added Darcy's and Forchcheimer's terms into the NS equations to simulate laminar and turbulent flows.

2.3.3   SPH

SPH was originally developed by Lucy (1977) and Gingold and Monaghan (1977) for collision problems in astrophysics. The basic concept of SPH is that the physical properties of each particle can be interpolated from those of neighbour particles. The major differences between SPH and MPS are the interpolation process and the pressure equation. Monaghan (1992) reviewed the SPH formulae and demonstrated the applicability of SPH to astrophysical, magnetics, and thermal dynamics problems. Since Monaghan (1994) applied SPH to free-surface flows, SPH has been widely used in the field of CFD. Monaghan and Kos (1999) utilized SPH to simulate a solitary wave run-up travelling over a slope with a vertical wall. It is noteworthy that these structures were regarded as solid materials, and that SPH in the early stage assumed flows to be slightly compressible. This type of SPH is classified as Weakly Compressible SPH (WCSPH). Rogers et al. (2010) simulated a wave breaking around caisson breakwaters in a coastal area using the open-source code SPHysics. The interactions between waves and impermeable coastal structures were also investigated by Altomare et al. (2015) and Didier et al. (2014). Dao et al. (2013) simulated solitary waves with WCSPH and estimated wave impacts on a vertical wall.

In one of the earliest work to simulate porous flows with SPH, Zhu et al. (1999) developed the pore-scale model. They modified the numerical model for low Reynolds number

scenarios by considering treatment of viscosity, the equation of state, and non-slip boundary conditions. Ren et al. (2014, a) simulated wave interactions with a rubble mound breakwater with WCSPH. Subsequently, Ren et al. (2014, b) and Ren et al. (2016) further improved the WCSPH method to simulate wave motions and turbulent flows around porous media. In their model, porosity information is defined by background porosity points. They proposed a transition zone between pure fluid and porous areas, where porosity changes gradually. Valizadeh and Rudman (2017) modelled a thin perforated plate and investigated a solitary wave's interaction with a vertical porous screen. They concluded that wave energy absorption can be predicted as a function of permeability. Peng et al. (2017) proposed a WCSPH method based on the governing equations with the mixture theory. Their model enables the volume fraction to reproduce spatially varying porous media. Altomare et al. (2014) extended WCSPH to three-dimensional fluid-structure problems. They investigated the interactions between waves and rubble mound breakwaters using the open-source code, DualSPHysics. Zhang et al. (2017) also used DualSPHysics to simulate wave runup against smoothed and armoured dykes. The key features of their study are the realistic dimensions, bathymetry and coastal conditions in Chougwn, China, that they incorporated. Although WCSPH has been improved and applied to water-porous structure problems, it is not an all-purpose method, since it assumes flows to be weakly compressible and the formulae do not ensure the conservation of fluid volume. Moreover, pressure fields are not always accurate due to the explicit algorithm.

Cummins and Rudman (1999) introduced a new formulation that enforces incompressibility in SPH by adopting a fractional step method. The intermediate velocity

field obtained at the fractional time step is projected to divergence-free space by solving the Poisson Pressure Equation (PPE). This type of SPH is classified as incompressible SPH (ISPH). Later, Shao and Lo (2003) presented a strictly incompressible SPH. In their simulation, dam-breaking problems were considered for both Newtonian and non-Newtonian flows with a free surface. However, the ISPH formulations do not generally conserve angular momentum, which strongly influences computational stability, particularly for violent free-surface flows (Bonet and Lok, 1999). Khayyer et al. (2008) modified ISPH to satisfy the conservation of angular momentum with a correction matrix, which technique was originally suggested by Bonet and Lok (1999). Khayyer et al. (2009) further improved this ISPH by applying a source term of the PPE in a higher order. The modified source term is defined as Higher-order Source (HS) term. They assumed wave impact pressure on a vertical wall in the case of a dam break and wave propagation over a solid slope. While this Khayyer et al. (2009) model did not include any turbulent effects, the SPS turbulence model had been coupled with ISPH by Gotoh et al. (2004) and Shao and Gotoh (2005), which is similar to MPS coupled with the SPS model. After the HS scheme was presented, a hybrid source term was proposed by Asai et al. (2012), Koh et al. (2013) and Gui et al. (2013) to obtain accurate pressure fields and numerical stability. They combined the velocity divergence-free formulations, that is, the HS term, and the density-invariant term, which is the original form of the PPE source term, called the "standard source term." The numerical accuracy and errors of the hybrid source term were analysed by Gui et al. (2015, a).

While many applications of ISPH to wave-structure interaction problems assumed structures to be solid in the early stage, Shao (2010) is an innovative work applying ISPH

to flows through porous media. In his model, the flow outside porous media is represented by the unsteady two-dimensional NS equations, and the porous media is described by additional friction forces in the equations. An imaginary grid line is defined at the interface between a porous medium and a fluid region and the boundary conditions proposed by Huang et al. (2003) are used to enforce the continuity of velocity and stresses. Shao (2010) applied this ISPH to the wave damping problem over a porous bed and a submerged porous breakwater. He assumes that the turbulence effect can be negligible for the flow outside porous structures, which is similar to assumptions by Liu et al. (1999) and Huang et al. (2003). Akbari and Namin (2013) proposed a technique in which porosity information is defined in a finer background mesh. They also presented the apparent density concept to consider solid skeleton of porous structures, which enables the changing of particle size and smoothing length inside porous media. However, a varying smoothing length adversely affects the calculation of physical properties, since neighbour particles are identified depending on the smoothing length. Akbari (2014) further refined the Akbari and Namin (2013) method with the consideration of turbulence effects inside porous media. Gui et al. (2015, b) proposed an water-porous interface that has a thickness equal to four times the smoothing length to satisfy the continuity conditions presented in Huang et al. (2003). The pressure inside the interface zone is averaged using the kernel function. Pahar and Dhar (2016) defined the Brinkman equations as the governing equations for a flow through porous media, whereas the NS equations govern the pure fluid region. In their method, the representative volume of fluid particles was used, and the density of particles never changed. Pahar and Dhar (2017) improved the method by modifying the pressure gradient model and the implicit free-surface conditions. Khayyer et al. (2018) developed an ISPH method without any

transition zone or averaging processes. They adopted the fractional volume concept, where the fractional volume of the target fluid particles can be calculated based on the neighbouring solid particles of porous media. They coupled the HS scheme, Error-Compensating Source (ECS) scheme (Khayyer and Gotoh, 2011), the improved gradient model (Khayyer and Gotoh, 2010), the modified Laplacian operator (Khayyer and Gotoh, 2011) and the Dynamic Stabilised (DS) scheme (Tsuruta et al., 2013).

Many efforts have been made to develop an ISPH approach that can model flows propagating through porous structures. Areas of great interest include how to describe porous media within particle method schemes, and how to treat the interface between fluid and porous media to maintain the continuity of velocity, shear stresses and pressure fields.

Chapter 3   SPH methodology for incompressible flows

3.1   Governing equations

The governing equations of SPH are the momentum conservation equation and the mass conservation equation written in the following Lagrangian form:

$$\frac{D\boldsymbol{u}}{Dt} = -\frac{1}{\rho}\nabla P + \boldsymbol{f} + \nu\nabla^2\boldsymbol{u} \qquad (3.1.1)$$

$$\frac{1}{\rho}\frac{D\rho}{Dt} + \nabla \cdot \boldsymbol{u} = 0 \qquad (3.1.2)$$

where $\boldsymbol{u}$ is a velocity of a particle, P is pressure, $\boldsymbol{f}$ is an external force and ν is a laminar kinetic viscosity. If gravity is the only external force considered, the term $\boldsymbol{f}$ in Equation (3.1.1) can be replaced by $\boldsymbol{g}$.

3.2   Poisson Pressure Equation

Suppose that the position of a particle and any physical properties such as velocity, density and pressure are obtained at the current time step t. To compute those values at the next time step $t+1$ under the condition of incompressible flows, the time increment between t and $t+1$ should be divided into two phases: the prediction step t^* and the correction step t^{**}.

In the initial step, only the gravitational term and the viscous term on the right-hand side of Equation (3.1.1) are considered. This step is described by

$$\Delta\boldsymbol{u}_* = (\boldsymbol{g} + \nu\nabla^2\boldsymbol{u})\Delta t \qquad (3.2.1)$$

where $\Delta\boldsymbol{u}_*$ is the velocity increment during the prediction step and Δt is a time increment. The temporal particle velocity and position are obtained from the following two equations

$$\boldsymbol{u}_* = \boldsymbol{u}_t + \Delta\boldsymbol{u}_* \qquad (3.2.2)$$

$$\boldsymbol{r}_* = \boldsymbol{r}_t + \boldsymbol{u}_*\Delta t \qquad (3.2.3)$$

where the subscript * and t denote the quantities at the prediction step and at the time step

t, respectively.

In the second step, the pressure term in Equation (3.1.1) omitted in the prediction step is

considered, so that fluid density is adjusted. Similar to Equation (3.2.1), this is written as

$$\Delta \boldsymbol{u}_{**} = -\frac{1}{\rho_*} \nabla P_{t+1} \Delta t \qquad (3.2.4)$$

where $\Delta \boldsymbol{u}_{**}$ is the velocity increment during the correction step, and the subscript $t+1$

denotes the quantity at the coming time step $t+1$.

Based on Equation (3.2.4), the velocity at the next time step is obtained by

$$\boldsymbol{u}_{t+1} = \boldsymbol{u}_* + \Delta \boldsymbol{u}_{**} \qquad (3.2.5)$$

The particle position at time step $t+1$ can be updated as follows

$$\boldsymbol{r}_{t+1} = \boldsymbol{r}_t + \frac{\boldsymbol{u}_t + \boldsymbol{u}_{t+1}}{2} \Delta t \qquad (3.2.6)$$

To calculate $\Delta \boldsymbol{u}_{**}$ in Equation (3.2.4), the pressure in the next time step P_{t+1} must be

identified in advance.

The discrete form of the mass conservation equation is

$$\frac{1}{\rho_0} \frac{\rho_0 - \rho_*}{\rho_0 \Delta t^2} + \nabla \cdot (\Delta \boldsymbol{u}_{**}) = 0 \qquad (3.2.7)$$

where ρ_0 is the initial fluid density.

Combining Equations (3.2.4) and (3.2.7),

$$\nabla \cdot \left(\frac{1}{\rho_*} \nabla P_{t+1} \right) = \frac{\rho_0 - \rho_*}{\rho_0 \Delta t^2} \qquad (3.2.8)$$

is obtained. Equation (3.2.8) is the PPE of the ISPH method, and the term on the right-hand

side is called the standard source term. Equation (3.2.8) can be discretised using the

derivative formulae that are explained later in this chapter. Taking the coefficients of P_{t+1}

and the terms on the right-hand side, the discretised PPE can be described as a set of

simultaneous linear equations. They are solved by successive over-relaxation (SOR), which is one of the iterative methods.

3.3   Turbulence model

The SPS turbulence model (Gotoh et al. 2004) is coupled with the present ISPH method. The idea of the SPS turbulence model is similar to LES. LES is one of the spatially averaged models, where the sub-grid scale (SGS) is considered to model turbulence flows (Gotoh, 2018). If an eddy is sufficiently large, in other words, larger than the size of the computational grid, the NS equations are directly solved. In contrast, the turbulence model will be applied in the SGS when an eddy is smaller than the grid-scale (GS). LES is more suitable for unsteady and complex flows than the RANS model, although a high computational load is implied because resolution needs to be sufficiently high. Gotoh et al. (2004) proposed SPS following SGS as SPH can track violent free-surface and SPH coupled with time-averaged models such as the RANS model would yield limited results.

In the SPS turbulence model, the additional stress tensor is added into the filtered governing equation as follows:

$$\frac{D\overline{\boldsymbol{u}}}{Dt} = -\frac{1}{\rho}\nabla\overline{P} + \boldsymbol{g} + \nu\nabla^2\overline{\boldsymbol{u}} + \frac{1}{\rho}\nabla\cdot\vec{\tau} \tag{3.3.1}$$

where $\vec{\tau}$ is the SPS stress tensor and $\overline{}$ denotes filtering. Filtering in LES is a mathematical operation to remove a range of small scales. Each element of $\vec{\tau}$ is defined by

$$\tau_{ij} = \rho\left(\overline{u_\iota}\,\overline{u_J} - \overline{u_\iota u_J}\right) \tag{3.3.2}$$

The SPS stress tensor can be described by the eddy viscosity assumption as shown in the following equation:

$$\frac{\tau_{ij}}{\rho} = 2\nu_t\overline{S_{\iota J}} - \frac{2}{3}k\delta_{ij} \tag{3.3.3}$$

25

where ν_t is the turbulence eddy viscosity, $\overline{S_{ij}}$ is the SPS strain rate, k is the SPS turbulence kinetic energy and δ_{ij} is the Kronecker delta. The Smagorinsky model (Smagorinsky, 1963) has been widely used to model turbulence eddy viscosity and can be written as follows:

$$\nu_t = (Cs\Delta x)^2|\bar{S}| \tag{3.3.4}$$

where Cs is the Smagorinsky constant and Δx represents the particle spacing. The local strain rate $|\bar{S}|$ is defined by

$$|\bar{S}| = \left(2\overline{S_{ij}}\,\overline{S_{ij}}\right)^{\frac{1}{2}} \tag{3.3.5}$$

Cs is set to 0.1 in this study.

3.4   SPH formulae

3.4.1   Fundamentals

SPH formulae are based on the theory of integral interpolation which can be represented with the Dirac function $\delta(|\mathbf{r} - \mathbf{r}'|)$. For an arbitrary function $A(r)$ with a domain Ω, this can be written as follows:

$$A(\mathbf{r}) = \iiint_{\Omega} A(\mathbf{r}')\delta(|\mathbf{r} - \mathbf{r}'|)dV \tag{3.4.1}$$

Replacing the Dirac function with the function W which has a certain range h,

$$A(\mathbf{r}) \approx \iiint_{\Omega} A(\mathbf{r}')W(|\mathbf{r} - \mathbf{r}'|, h)dV \tag{3.4.2}$$

is obtained. The right-hand side of Equation (3.4.2) describes a function $A(r)$ taking a weighted average. In SPH, an arbitrary physical property $\Phi(\mathbf{r})$ of the target particle i is interpolated from that of its neighbour particles j. Based on Equation (3.4.2), this can be written as

$$\Phi(\mathbf{r}_i) = \iiint_{\Omega} \Phi(\mathbf{r}_j)W_{ij}dV \tag{3.4.3}$$

26

where W_{ij} denotes $W(|\boldsymbol{r}_j - \boldsymbol{r}_i|, h)$ and the range h is a smoothing length. Ω is a support domain, which is included in an entire problem domain. Information of all points inside a support domain is used to calculate a physical property of the target point. The right-hand side of Equation (3.4.3) is discretised by summation of $\Phi(\boldsymbol{r}_j)$ as follows:

$$\Phi(\boldsymbol{r}_i) \approx \sum_j \Phi(\boldsymbol{r}_j) W_{ij} \Delta V_j \tag{3.4.4}$$

Suppose that the volume, density and mass of a particle j are represented by ΔV_j, ρ_j and m_j, respectively. The relationship among volume, density, and mass is described as

$$m_j = \Delta V_j \rho_j \tag{3.4.5}$$

Combining Equation (3.4.4) and Equation (3.4.5),

$$\Phi(\boldsymbol{r}_i) = \sum_j \frac{m_j}{\rho_j} \Phi(\boldsymbol{r}_j) W_{ij} \tag{3.4.6}$$

is obtained. Equation (3.4.6) is the fundamental formula of approximation in SPH.

3.4.2　　　　　Kernel function

The function W_{ij} included in Equation (3.4.6) is called a kernel function or a smoothing function, and it must satisfy the following seven criteria (Liu and Liu, 2003, Gotoh. 2018).

(1) *Normalisation*: The kernel function can be normalised over the support domain, which means that

$$\iiint_\Omega W_{ij} dV = 1 \tag{3.4.7}$$

This normalisation property ensures that the integral of the kernel function will be unity.

(2) *Compact support*: A support domain should have a limited range, and the value of the kernel function should be zero outside the range. This is described by the following equation

$$W_{ij} = 0, \ \text{for} \ |\boldsymbol{r}_j - \boldsymbol{r}_i| > \kappa h \tag{3.4.8}$$

27

where κ is a scaling factor, that determines the spread of the kernel function. Due to the compact support, neighbouring particles outside the support domain can be ignored when Equation (3.4.6) is calculated, significantly reducing computational loads.

(3) *Positivity*: A kernel function must take positive value within its support domain, as expressed in Equation (3.4.9):

$$W_{ij} \geq 0, \ \ \text{for} \ |\boldsymbol{r}_j - \boldsymbol{r}_i| \leq \kappa h \tag{3.4.9}$$

A negative value for the kernel function will result in negative values for physical properties such as density and energy. The positivity property ensures that this physically impossible result is avoided.

(4) *Decay*: The value of the kernel function should decrease monotonically as neighbouring particles become further away from the target particle i. The decay criterion follows the physical principle that nearer particles should influence the target particle more strongly.

(5) *Convergence property*: The kernel function will converge towards the Dirac function if the smoothing length takes a limit of zero, which can be written as

$$\lim_{h \to 0} W_{ij} = \delta(|\boldsymbol{r}_j - \boldsymbol{r}_i|) \tag{3.4.10}$$

When the smoothing length approaches zero, the approximated value of the reference particle will be the original value of the particle.

(6) *Symmetry property*: The kernel function should be an even function. The symmetry property ensures that particles that are located at the same distance from the target particle but at different positions should interact with the target particle equally. However, the gradient takes different sign between the close two positions, i.e.,

$$\nabla W_{ij}|_{\boldsymbol{i}} = -\nabla W_{ij}|_{\boldsymbol{j}} \tag{3.4.11}$$

(7) *Smoothness*: The kernel function and its derivative should be continuous and smooth. Smoother kernel functions are expected to yield more precise approximations. The second derivative of the compactly supported kernel function can be continuous, which

means that the kernel function is not sensitive to particle disorders (Monaghan, 1992). Errors in the approximation of integral interpolants will not be severe provided that particle disorders are small.

In the original SPH, Lucy (1977) proposed the following quartic kernel:

$$W_L(q,h) = \alpha \begin{cases} (1+3q)(1-q)^3 & (0 \leq q \leq 1) \\ 0 & (1 < q) \end{cases}$$

$$q \equiv \frac{r}{h} \tag{3.4.12}$$

$$\alpha^{2D} = \frac{5}{\pi h^2}; \qquad \alpha^{3D} = \frac{105}{16\pi h^3}$$

while Gingold and Monaghan (1977) applied the Gaussian kernel

$$W_g(q,h) = \alpha e^{-q^2}$$

$$\alpha^{2D} = \frac{1}{\pi h^2}; \qquad \alpha^{3D} = \frac{1}{\pi^{\frac{3}{2}} h^3} \tag{3.4.13}$$

where the superscript of α represents the dimension.

Monaghan and Lattanzio (1985) introduced the following cubic B-spline kernel:

$$W_{BS}(q,h) = \alpha \begin{cases} 1 - \frac{3}{2}q^2 + \frac{3}{4}q^3 & (0 \leq q \leq 1) \\ \frac{1}{4}(2-q)^3 & (1 \leq q \leq 2) \\ 0 & (2 < q) \end{cases}$$

$$\alpha^{2D} = \frac{10}{7\pi h^2}; \qquad \alpha^{3D} = \frac{1}{\pi h^3} \tag{3.4.14}$$

which has been widely used in SPH.

Wendland (1995) proposed the fifth-order polynomial kernel as follows:

$$W_W(q,h) = \alpha \begin{cases} \left(1 - \frac{q}{2}\right)^4 (1+2q) & (0 \leq q \leq 2) \\ 0 & (2 < q) \end{cases}$$

$$\alpha^{2D} = \frac{7}{4\pi h^2}; \qquad \alpha^{3D} = \frac{21}{16\pi h^3} \tag{3.4.15}$$

The kernel functions for two dimensions are shown in Figure 3.1. As the figure illustrates, only the quartic kernel (Lucy, 1977) reaches zero at $q = 1$ and shows a rapid and significant decrease. Other kernels decrease more gradually as q goes to 2. The higher-order kernel such as the Wendland kernel may lead to expensive computational load whereas such kernel function yields more precise SPH approximations. Although the Gaussian kernel (Gingold and Monaghan, 1977) is sufficiently smooth including its high order derivatives, it is not compact (Liu and Liu, 2003). Theoretically, the Gaussian kernel never goes to zero unless the value of q is infinity. However, in practical terms, it appears compact because it approaches zero rapidly.

In SPH, spatial derivatives are obtained by using kernel derivatives, as shown in the following section. Hence, the kernel function must be chosen carefully through evaluation of its derivatives. Although there are many other kernels and mathematically they may be possible choices, the studies reviewed in Chapter 2 adopted either the B-spline or the Wendland kernel. Here these two kernels are focused and examined to see whether they are desirable. Figures 3.2 and 3.3 describe the first and the second derivatives, respectively, of the kernel functions. The quartic and Gaussian kernels are included just for reference. While the first derivative of the B-spline kernel (Monaghan and Lattanzio, 1985) is sufficiently smooth and acceptable (Figure 3.2), the second derivative is obviously not smooth at $q = 1.0$ (Figure 3.3). Based on the derivatives, the B-spline and the Wendland functions are candidates for use as smoothing functions, but the B-spline is less stable and thus less desirable. The choice of kernel function in terms of the pressure field will be further discussed in Chapter 4.
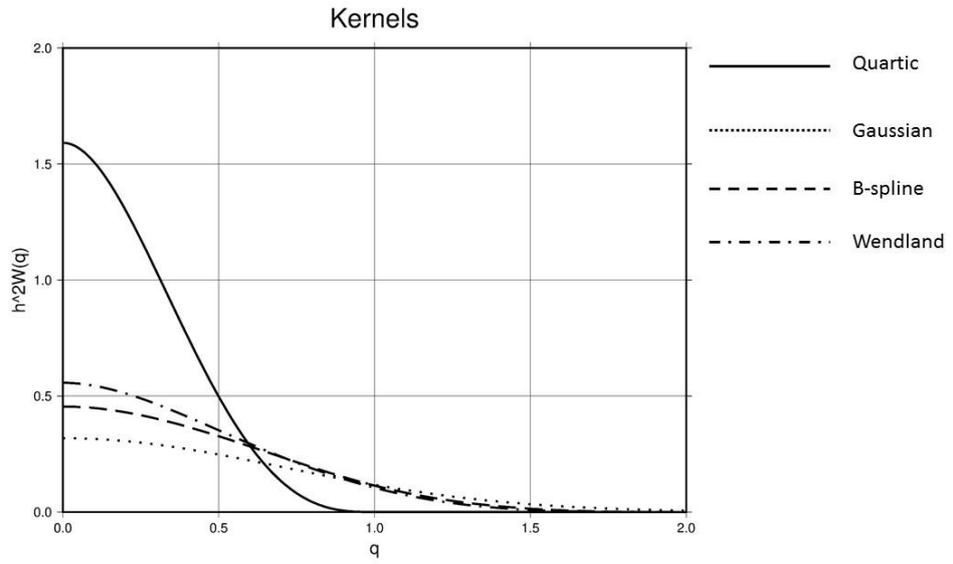
Figure 3.1 Kernel functions
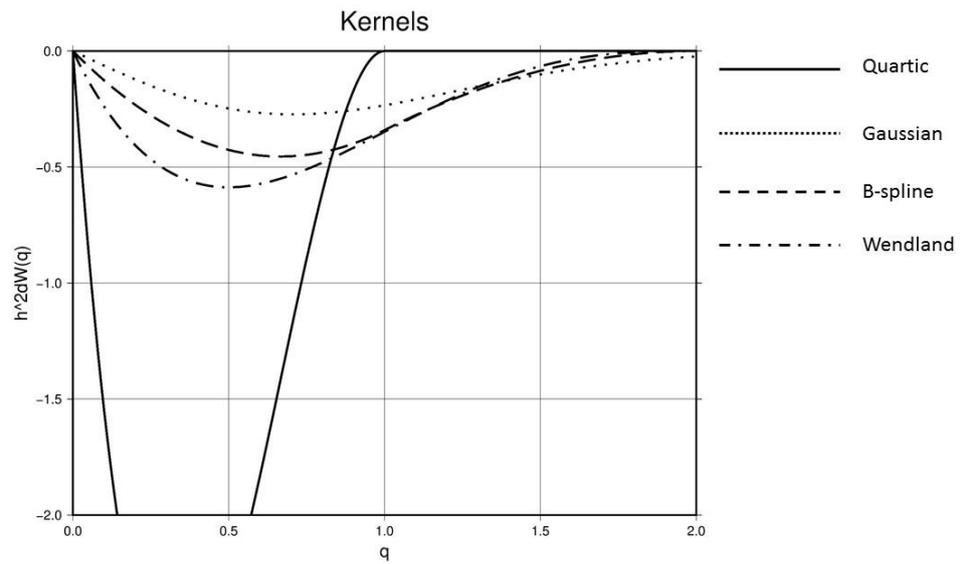
Figure 3.2 First derivatives of kernel functions
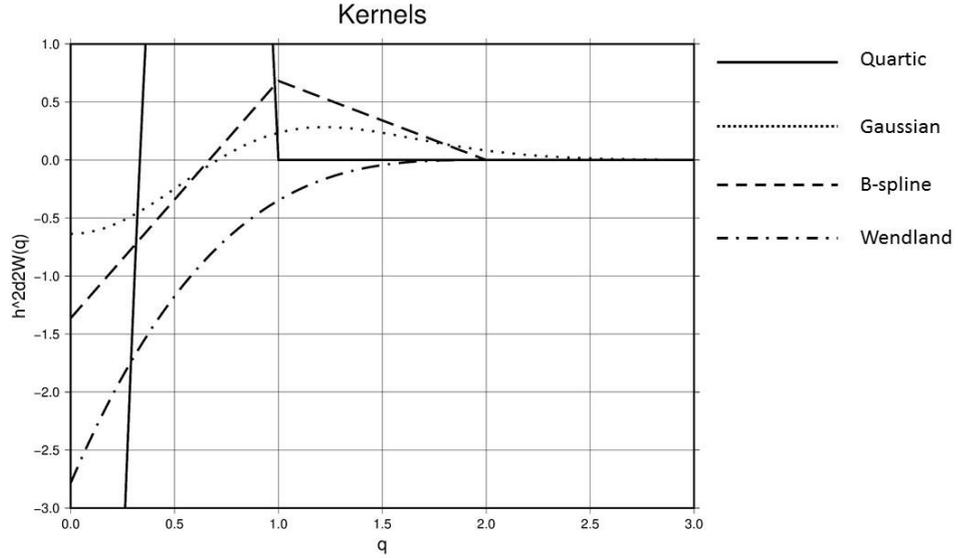
Figure 3.3 Second derivatives of kernel functions

3.4.3　　　　　Derivatives

Based on Equation (3.4.3), an approximation for the gradient of an arbitrary physical property can be deduced as follows:

$$\nabla \Phi(\boldsymbol{r}_i) = \iiint\limits_{\Omega} \nabla \Phi(\boldsymbol{r}_j)\big|_j W_{ij} dV \tag{3.4.16}$$

Considering the right-hand side of Equation (3.4.16), the term inside the integral is included in the following equation:

$$\nabla\{\Phi(\boldsymbol{r}_j)W_{ij}\}\big|_j = \nabla \Phi(\boldsymbol{r}_j)\big|_j W_{ij} + \Phi(\boldsymbol{r}_j)\nabla W_{ij}\big|_j \tag{3.4.17}$$

Equation (3.4.17) can be written as

$$\nabla \Phi(\boldsymbol{r}_j)\big|_j W_{ij} = \nabla\{\Phi(\boldsymbol{r}_j)W_{ij}\}\big|_j - \Phi(\boldsymbol{r}_j)\nabla W_{ij}\big|_j \tag{3.4.18}$$

Since the kernel function is an even function, the second term of the right-hand side in Equation (3.4.18) can be replaced with the positive gradient around i based on Equation (3.4.11) as follows:

32

$$\nabla\Phi(\pmb{r}_j)\big|_j W_{ij} = \nabla\{\Phi(\pmb{r}_j)W_{ij}\}\big|_j + \Phi(\pmb{r}_j)\nabla W_{ij}\big|_i \qquad (3.4.19)$$

The right-hand side of Equation (3.4.16) becomes

$$\iiint_\Omega \nabla\Phi(\pmb{r}_j)\big|_j W_{ij}dV = \iiint_\Omega \nabla\{\Phi(\pmb{r}_j)W_{ij}\}\big|_j dV + \iiint_\Omega \Phi(\pmb{r}_j)\nabla W_{ij}\big|_i dV \qquad (3.4.20)$$

Applying Gauss's gradient theorem to Equation (3.4.20), the first term on the right-hand side in Equation (3.4.20) can be expressed as a surface integral, and thus Equation (3.4.20) can be written as

$$\iiint_\Omega \nabla\Phi(\pmb{r}_j)\big|_j W_{ij}dV = \iint_S \Phi(\pmb{r}_j)W_{ij}\pmb{n}dS + \iiint_\Omega \Phi(\pmb{r}_j)\nabla W_{ij}\big|_i dV \qquad (3.4.21)$$

where S is the boundary surface of Ω and $\pmb{n}$ is the unit normal vector, which is perpendicular to the surface S. Since the kernel will be zero on the boundary surface S, the first term on the right-hand side of Equation (3.4.21) vanishes:

$$\iiint_\Omega \nabla\Phi(\pmb{r}_j)\big|_j W_{ij}dV = \iiint_\Omega \Phi(\pmb{r}_j)\nabla W_{ij}\big|_i dV \qquad (3.4.22)$$

Substituting Equation (3.4.22) into Equation (3.4.16),

$$\nabla\Phi(\pmb{r}_i) = \iiint_\Omega \Phi(\pmb{r}_j)\nabla W_{ij}\big|_i dV \qquad (3.4.23)$$

is obtained.

The approximation of the divergence for a vector function can be deduced by

$$\nabla \cdot \pmb{\Phi}(\pmb{r}_i) = \iiint_\Omega \nabla \cdot \pmb{\Phi}(\pmb{r}_j)W_{ij}dV \qquad (3.4.24)$$

Following a similar procedure to the gradient form,

$$\nabla \cdot \pmb{\Phi}(\pmb{r}_i) = \iiint_\Omega \pmb{\Phi}(\pmb{r}_j) \cdot \nabla W_{ij}\big|_i dV \qquad (3.4.25)$$

is obtained.

3.4.4 Operators

From Equation (3.4.6), the discretised forms of Equations (3.4.23) and (3.4.25) are expected to be written as

$$\nabla_i \Phi(\boldsymbol{r}_i) = \sum_j \frac{m_j}{\rho_j} \Phi(\boldsymbol{r}_j) \nabla_i W_{ij} \tag{3.4.26}$$

and

$$\nabla_i \cdot \boldsymbol{\Phi}(\boldsymbol{r}_i) = \sum_j \frac{m_j}{\rho_j} \boldsymbol{\Phi}(\boldsymbol{r}_j) \cdot \nabla_i W_{ij} \tag{3.4.27}$$

respectively, where $\nabla_i W_{ij}$ denotes the gradient of the function W_{ij} with respect to the position of particle i. However, these equations are not necessarily accurate because the force on a particle i due to particle j may not equal the force on a particle j due to particle i when the Equations (3.4.26) and (3.4.27) are applied to the governing equations. The SPH formulae can be transformed so that the density is placed inside the operators (Monaghan, 1992) as follows:

$$\nabla \left(\frac{\Phi}{\rho} \right) = \frac{\rho \nabla \Phi - \Phi \nabla \rho}{\rho^2} \tag{3.4.28}$$

Considering this rule, Equation (3.4.26) can be written as

$$\nabla \Phi(\boldsymbol{r}_i) = \rho_i \sum_j m_j \left(\frac{\Phi(\boldsymbol{r}_i)}{\rho_i^2} + \frac{\Phi(\boldsymbol{r}_j)}{\rho_j^2} \right) \nabla_i W_{ij} \tag{3.4.29}$$

Similarly, Equation (3.4.27) can be modified to the following form

$$\nabla \cdot \boldsymbol{\Phi}(\boldsymbol{r}_i) = \rho_i \sum_j m_j \left(\frac{\boldsymbol{\Phi}(\boldsymbol{r}_i)}{\rho_i^2} + \frac{\boldsymbol{\Phi}(\boldsymbol{r}_j)}{\rho_j^2} \right) \cdot \nabla_i W_{ij} \tag{3.4.30}$$

The Laplacian of $\Phi(\boldsymbol{r}_i)$ is derived by taking the divergence of the gradient model

$$\nabla^2 \Phi(\boldsymbol{r}_i) = \nabla \cdot (\nabla \Phi(\boldsymbol{r}_i)) \tag{3.4.31}$$

Combining Equation (3.4.26) and Equation (3.4.27), Equation (3.4.31) can be expressed as follows:

$$\nabla_i{}^2\Phi(\boldsymbol{r}_i) = \sum_j \frac{m_j}{\rho_j} \nabla_j\Phi(\boldsymbol{r}_j) \cdot \nabla_i W_{ij} \tag{3.4.42}$$

Considering the following Taylor series expansion of $\Phi(\boldsymbol{r}_i)$ around the position of the particle j,

$$\Phi(\boldsymbol{r}_i) = \Phi(\boldsymbol{r}_j) + \nabla_j\Phi(\boldsymbol{r}_j) \cdot (\boldsymbol{r}_i - \boldsymbol{r}_j) \tag{3.4.43}$$

The gradient approximation of $\Phi(\boldsymbol{r}_j)$ can be written as

$$\nabla_j\Phi(\boldsymbol{r}_j) = \left(\Phi(\boldsymbol{r}_j) - \Phi(\boldsymbol{r}_i)\right)\frac{\boldsymbol{r}_j - \boldsymbol{r}_i}{|\boldsymbol{r}_j - \boldsymbol{r}_i|^2} \tag{3.4.44}$$

Note that the second term is ignored in Equation (3.4.43).

Substituting Equation (3.4.44) into Equation (3.4.42),

$$\nabla_i{}^2\Phi(\boldsymbol{r}_i) = \sum_j \frac{m_j}{\rho_j}\left(\Phi(\boldsymbol{r}_j) - \Phi(\boldsymbol{r}_i)\right)\frac{(\boldsymbol{r}_j - \boldsymbol{r}_i) \cdot \nabla_i W_{ij}}{|\boldsymbol{r}_j - \boldsymbol{r}_i|^2} \tag{3.4.45}$$

is obtained.

As with the gradient operator and the divergence operator, the density should be included inside the Laplacian operator:

$$\nabla \cdot \left(\frac{\nabla\Phi}{\rho}\right) = \nabla\left(\frac{1}{\rho}\right) \cdot \nabla\Phi + \frac{1}{\rho}\nabla^2\Phi \tag{3.4.46}$$

The first term in Equation (3.4.46) can be written as follows

$$\left(\nabla\left(\frac{1}{\rho_i}\right) \cdot \nabla\Phi(\boldsymbol{r}_i)\right)_i = \sum_j \frac{m_j}{\rho_j}\frac{1}{\rho_j}\nabla_i W_{ij} \cdot \left(\Phi(\boldsymbol{r}_j) - \Phi(\boldsymbol{r}_i)\right)\frac{\boldsymbol{r}_j - \boldsymbol{r}_i}{|\boldsymbol{r}_j - \boldsymbol{r}_i|^2} \tag{3.4.47}$$

Combining Equation (3.4.45) and Equation (3.4.47), the Laplacian operator will be

$$\left(\nabla \cdot \left(\frac{\nabla\Phi(\boldsymbol{r}_i)}{\rho_i}\right)\right)_i = \sum_j \frac{m_j}{\rho_j}\left(\frac{1}{\rho_j} + \frac{1}{\rho_i}\right)\left(\Phi(\boldsymbol{r}_j) - \Phi(\boldsymbol{r}_i)\right)\frac{(\boldsymbol{r}_j - \boldsymbol{r}_i) \cdot \nabla_i W_{ij}}{|\boldsymbol{r}_j - \boldsymbol{r}_i|^2} \tag{3.4.48}$$

The calculated density of particles i and j should be replaced by their arithmetic averages so that the formula satisfies the symmetry property:

$$\rho_i \to \frac{\rho_i + \rho_j}{2}; \qquad \rho_j \to \frac{\rho_j + \rho_i}{2} \tag{3.4.49}$$

Therefore, the symmetric Laplacian operator is obtained in the following form

$$\left(\nabla \cdot \left(\frac{\nabla \Phi(\mathbf{r}_i)}{\rho_i} \right) \right)_i = \sum_j \frac{8 m_j}{(\rho_i + \rho_j)^2} (\Phi(\mathbf{r}_j) - \Phi(\mathbf{r}_i)) \frac{(\mathbf{r}_j - \mathbf{r}_i) \cdot \nabla_i W_{ij}}{|\mathbf{r}_j - \mathbf{r}_i|^2} \qquad (3.4.50)$$

Based on Equations. (3.4.29), (3.4.30) and (3.4.50), the governing equations (3.1.1) and (3.1.2) can be discretised as follows:

$$\left(\frac{1}{\rho} \nabla P \right)_i = \sum_j m_j \left(\frac{P_i}{\rho_i{}^2} + \frac{P_j}{\rho_j{}^2} \right) \nabla_i W_{ij} \qquad (3.4.51)$$

$$\nabla \cdot \mathbf{u}_i = \rho_i \sum_j m_j \left(\frac{\mathbf{u}_i}{\rho_i{}^2} + \frac{\mathbf{u}_j}{\rho_j{}^2} \right) \cdot \nabla_i W_{ij} \qquad (3.4.52)$$

$$\nabla \cdot \left(\frac{1}{\rho} \nabla P \right)_i = \sum_j m_j \frac{8}{(\rho_i + \rho_j)^2} \frac{(P_j - P_i)(\mathbf{r}_j - \mathbf{r}_i) \cdot \nabla_i W_{ij}}{|\mathbf{r}_j - \mathbf{r}_i|^2} \qquad (3.4.53)$$

$$(\nu \nabla^2 \mathbf{u})_i = \sum_j m_j \frac{2(\nu_i + \nu_j)(\mathbf{r}_j - \mathbf{r}_i) \cdot \nabla_i W_{ij}}{|\mathbf{r}_j - \mathbf{r}_i|^2} \qquad (3.4.54)$$

3.5 Wave generation theory

A solitary wave is a single bulge of water entirely above still water depth, which was discovered by Russell (1844). Theories to describe the wave profile was later proposed by Boussinesq (1872), McCowan (1891), and Laitone (1963). A solitary wave can be generated in a wave flume by a piston (Goring, 1978) or a heavy box (Monaghan and Kos, 2000). In this study, a piston-type wavemaker is used. The basic concept is to match the velocity of the wavemaker plate at all position in time t with the corresponding velocity of the wave at each time, which can be described mathematically as follows:

$$\frac{dX}{dt} = \bar{u}(x, t) \qquad (3.5.1)$$

where $x = X$ is the position of the wave paddle in the horizontal axis and $\bar{u}(x, t)$ is the depth-averaged horizontal velocity of the wave.

For the waves in the permanent form, Equation (3.5.1) can be written as:

$$\bar{u}(x,t) = \frac{c\eta(x,t)}{h_0 + \eta(x,t)} \qquad (3.5.2)$$

(Svendsen, 1974), where c is the wave phase speed, h_0 is the mean water depth and $\eta(x,t)$ is a function of the free surface elevation. The velocity of the paddle is

$$\dot{X} = \frac{c\eta(X,t)}{h_0 + \eta(X,t)} \qquad (3.5.3)$$

$X(t)$ can be obtained by integrating Equation (3.5.3).

It is assumed that the wave has the following form

$$\eta(x,t) = Hf(\theta); \qquad \theta = \frac{\beta}{2}(ct - X) \qquad (3.5.4)$$

where H is the wave amplitude, β is the outskirts decay coefficient, and $f(\theta)$ is the wave function. The total derivative of X is

$$\frac{dX}{d\theta} = \frac{\dfrac{dX}{dt}}{\dfrac{d\theta}{dt}} = \frac{2\dot{X}}{\beta(c - \dot{X})} \qquad (3.5.5)$$

Substituting Equation (3.5.3) into Equation (3.5.5),

$$\frac{dX}{d\theta} = \frac{2\varepsilon f(\theta)}{\beta}; \qquad \varepsilon = \frac{H}{h_0} \qquad (3.5.6)$$

is obtained. The integration of Equation (3.5.6) is

$$X(t) = \frac{2\varepsilon}{\beta} \int_0^\theta f(w)dw; \qquad \theta \to w \qquad (3.5.7)$$

where w is the dummy variable of integration.

Equation (3.5.7) is an implicit equation and it can be solved numerically if the particular time t is given. The function $f(\theta)$ and the coefficient β need to be determined to obtain the position of the wavemaker.

Goring (1978) investigated methods of generating waves with the piston-type wavemaker in an experimental flume and proposed some equations for paddle movement. Goring's

(1978) theory of solitary wave generation is based on the Boussinesq (1871) solitary wave expression:

$$f_B(\theta) = sech^2(\theta); \qquad \theta = \frac{\beta_B}{2}(c_B t - X) \tag{3.5.8}$$

The wave phase speed and the outskirts decay coefficient are

$$c_B = \sqrt{g(H + h_0)}$$
$$\beta_B = \frac{1}{h_0}\sqrt{3\varepsilon} \tag{3.5.9}$$

Substituting Equation (3.5.8) into Equation (3.5.7) and integrating it, the position of the wavemaker can be obtained as follows

$$X_B(t) = \frac{2\varepsilon}{\beta_B} tanh\left[\frac{\beta_B(c_B t - X_B(t))}{2}\right] \tag{3.5.10}$$

The total stroke of the paddle movement S_B can be estimated by integrating Equation (3.5.10) from $t = -\infty$ to $t = +\infty$, which yields

$$S_B = \frac{4\varepsilon}{\beta_B} \tag{3.5.11}$$

Katell and Eric (2002) proposed another law based on the Rayleigh solution of a solitary wave. Serre (1953) had found the following solitary wave solution

$$\beta_R = \frac{1}{h_0}\sqrt{\frac{3\varepsilon}{1 + \varepsilon}}$$
$$c_R = \sqrt{g(H + h_0)} \tag{3.5.12}$$

This is, in fact, the solution which was found by Rayleigh (1876) for the steady progressive solution. From this solution, Katell and Eric (2002) presented the following new equation for the paddle position:

$$X_R(t) = \frac{2\varepsilon}{\beta_R} tanh\left[\frac{\beta_R(c_R t - X_R(t))}{2}\right] \tag{3.5.13}$$

Equation (3.5.13) can be solved numerically using Equation (3.5.7). If the displacement of the paddle is assumed to be small, Equation (3.5.13) will be solved explicitly after linearisation:

$$X_R(t) = \frac{2\varepsilon}{\beta_R} \frac{\tanh(\frac{\beta_R c_R t}{2})}{1 + \varepsilon\left[1 - \tanh^2\left(\frac{\beta_R c_R t}{2}\right)\right]} \tag{3.5.14}$$

The total stroke of the wave paddle will be

$$S_R = 4\sqrt{\frac{H(H + h_0)}{3}} \tag{3.5.15}$$

Farhadi et al. (2016) reviewed and compared six different theories of solitary wave generation, including the Goring law and the Katell law, in an ISPH-based wave flume. They found that the wave generated by the Rayleigh-based theory reduced the least height of its amplitude. In other methods, either wave became too attenuated as it propagated, or the initial wave height was too great and the wave profile was not in good agreement with the analytical one. Moreover, the Rayleigh-based solitary waves yielded the most accurate results for wave runup height. Since runup height will be focused on in Chapters 5 and 6, the Katell law is adopted in this study.

Figure 3.4 shows the position of the wave paddle to generate the wave $H = 0.0588$ [m]. The initial water depth is 0.21 m. The solid line is an explicit solution expressed in Equation (3.5.14) and the dashed line is a numerical solution obtained through Equations (3.5.7) and (3.5.13). Notably, the graphs are shifted so that the wave paddle can move rightward after $t = 0$ [s]. The explicit solution drives the wave paddle faster than the numerical solutions at the initial phase of the wave generation process, which means that more particles are pushed and the generated wave is expected to be larger than the intended wave amplitude. When a

relatively large solitary wave is considered in simulations, the numerical solution must be

used.
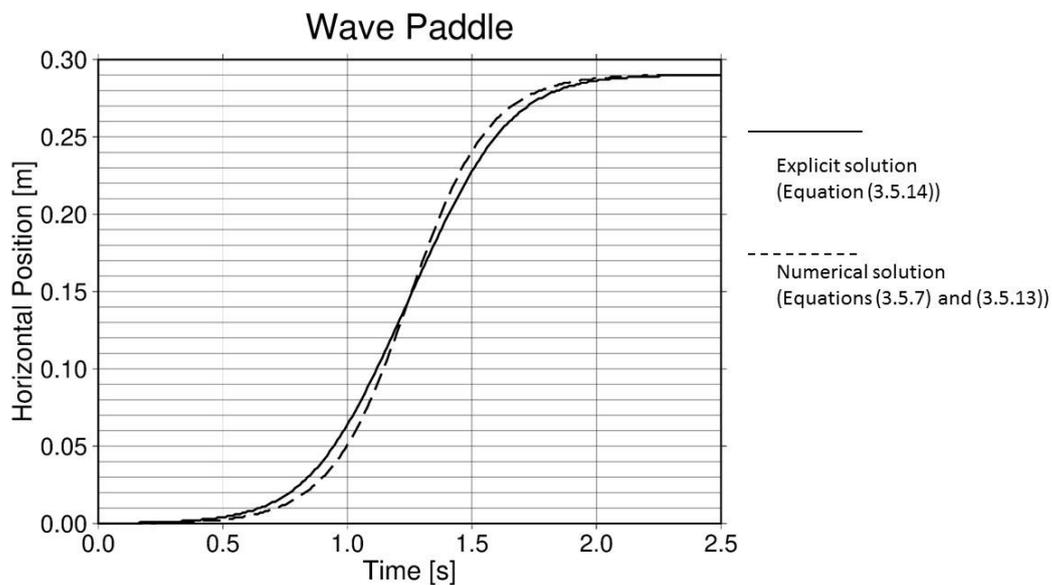
Figure 3.4 Paddle movement profile for a solitary wave of height H = 0.0588 [m] and

initial water depth h_0 = 0.21 [m]

Figure 3.5 describes the wave generation process using Equations (3.5.7) and (3.5.13). The

initial water depth was 0.21 m and the intended wave amplitude was 0.0588 m. In Figure

3.5 (d), the solid line represents the analytical wave profile. Although the wave crest was

slightly higher than the intended wave amplitude, the generated wave agreed strongly with

the analytical wave profile.

(a) $t = 0.50$ [s]

(b) $t = 1.00$ [s]

Solitary Wave

(c) t = 1.50 [s]
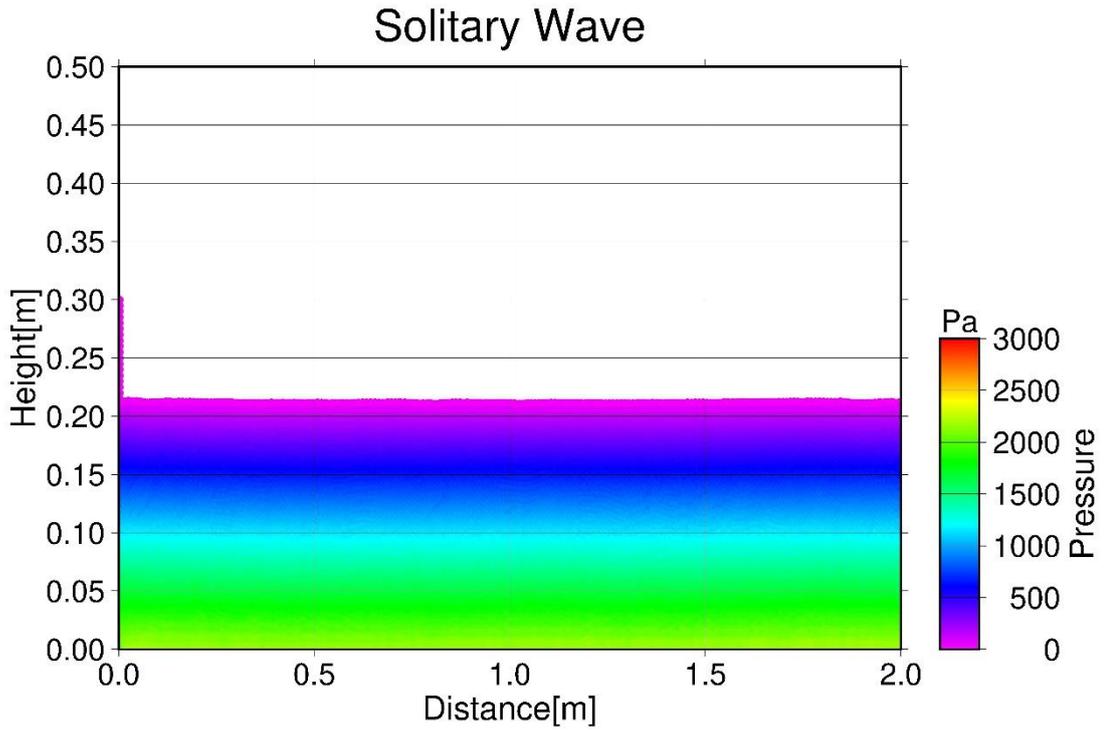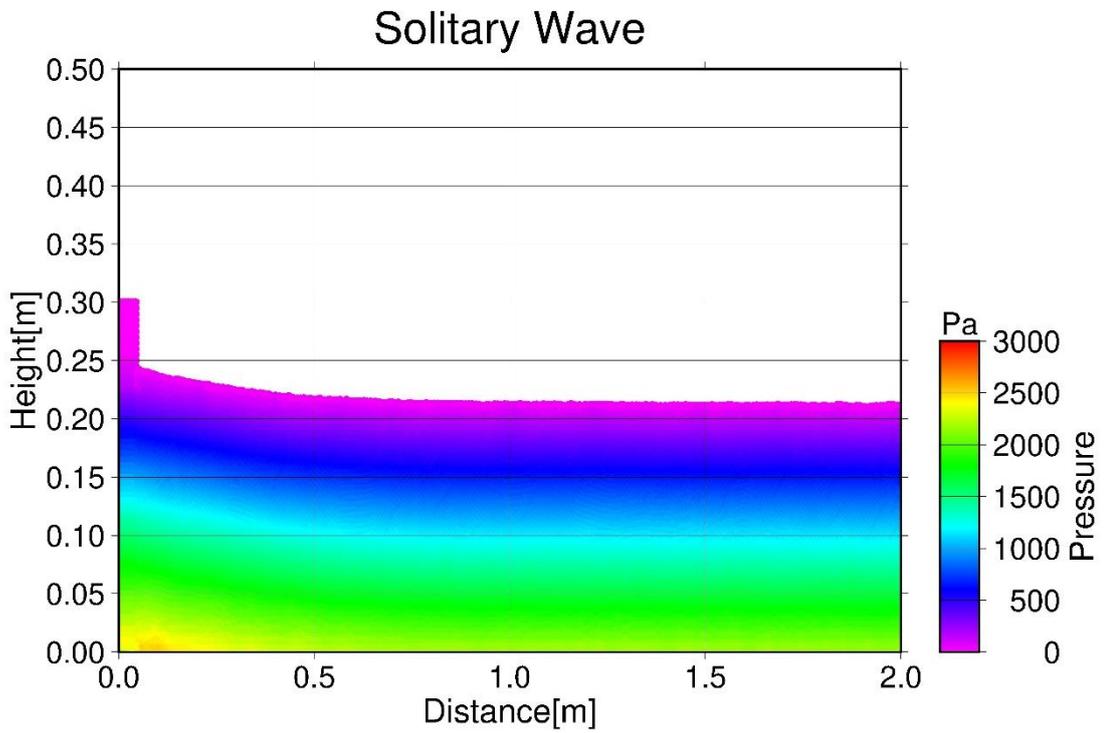
Solitary wave

(d) t = 2.0 [s]
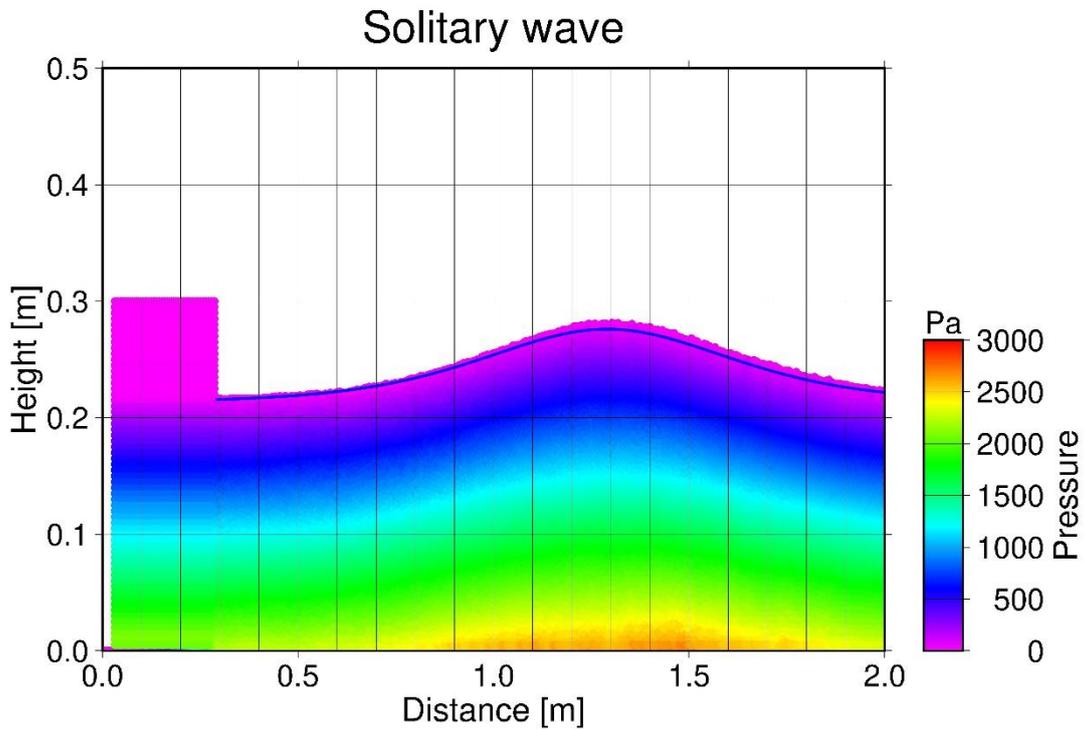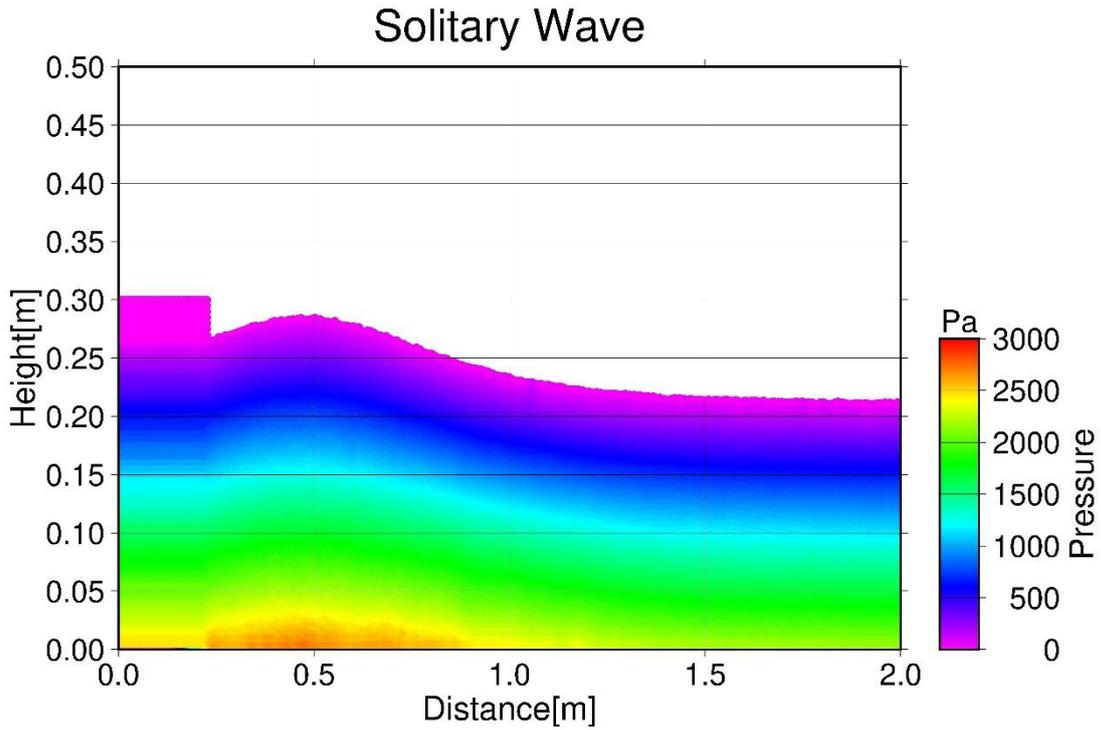
Figure 3.5 Solitary wave generation and profiles of the wave with H = 0.00588 [m] and

h_0 = 0.21 [m]

42

3.6   Time integration

In CFD, the time step needs to be adjusted to satisfy a stability constraint, namely, the Courant-Friedrichs-Levy (CFL) condition (Courant et al. 1928). Consider the solution of the following advection equation within the scheme of the grid method:

$$\frac{\partial \Phi}{\partial t} + u\frac{\partial \Phi}{\partial x} = v\frac{\partial^2 \Phi}{\partial x^2} \tag{3.6.1}$$

Taking a first-order backward difference for the spatial derivative and a first-order forward difference for the timely derivative, respectively, Equation (3.6.1) becomes

$$\frac{\Phi_j^{k+1} - \Phi_j^k}{\Delta t} + u\frac{\Phi_j^k - \Phi_{j-1}^k}{\Delta x} = 0 \tag{3.6.2}$$

where the subscript denotes the position of the grid and the superscript denotes the time step. Equation (3.6.2) can be written as

$$\Phi_j^{k+1} = \Phi_j^k - C(\Phi_j^k - \Phi_{j-1}^k); \quad C = \frac{u\Delta t}{\Delta x} \tag{3.6.3}$$

where C is the Courant number.

Taking the backward and forward differences affects numerical errors to obtain the solution of the advection equation. Thus, it was of great importance whether the estimations would converge to the correct solution. In the explicit methods of solving partial differential equations, computation may break down due to the accumulation of numerical errors as the time step proceeds. The numerical stability of those methods can be evaluated by the von Neumann analysis. It is notable that comprehensive methods of numerical analysis for mesh-based methods are not possible for SPH, and analytical methods have not been developed for particle methods (Matsubara et al. 2010).

Considering the following Fourier expansion of the solution

$$\Phi_j^k = \sum_m C_m^k \exp(ik_m j\Delta x) \tag{3.6.4}$$

where i is an imaginary number unit, Cm is amplitude, and k_m is a number of waves, the ratio of the amplitudes

$$G = \frac{C_m^{k+1}}{C_m^k} \qquad (3.6.5)$$

is defined as the amplitude factor. Numerical errors will be bounded if the amplitude factor is less than one:

$$C = \frac{u\Delta t}{\Delta x} < 1 \qquad (3.6.6)$$

Equation (3.6.6) is called the CFL condition, which specifies that the propagation speed of information must be greater than the propagation speed of physical properties to ensure numerical stability of computation. In WCSPH, the velocity scale is based on the speed of sound, while ISPH bases the velocity scale on the fluid velocity (Violeau and Leroy, 2015). In this study, the velocity scale refers to the velocity of the fluid, and the initial particle spacing will be considered to be Δx to satisfy the CFL condition. Lo and Shao (2002) suggested that the Courant number should be the order of 0.1 and it is set at 0.1 in many works (for instance, Khayyer et al. 2008 and Akbari and Namin, 2013). Violeau and Leroy (2015) examined the optimal choice of the Courant number and reported that it should be 0.2 for ISPH. Following their recommendation, the Courant number is set at 0.2 in this thesis.

3.7   Boundary conditions
3.7.1   Solid boundary

The walls and the bottom of the computational flume are described by visible solid particles. Hereafter, these particles are referred to as wall particles. The wall particles are given constant values for mass and density, but are not movable. Once they are placed at the initial particle spacing d_0 in the initial configuration of the simulation, wall particles will be fixed, and their positions will never be updated. If a fluid particle approaches wall particles within the distance of the smoothing length h, the PPE will be solved including wall particles to ensure repulsion of the fluid particle from wall particles.

3.7.2   Boundary treatment

Near the solid boundary, the density of fluid particles drops because few neighbouring particles are included in the support domain. Truncation of the integral interpolation results in fluid particles penetrating and crossing the wall boundaries, which is not physically possible. To prevent fluid particles from leaking, three different methods are commonly applied: mirror particle, repulsive force, and dummy particle methods (Figure 3.6).
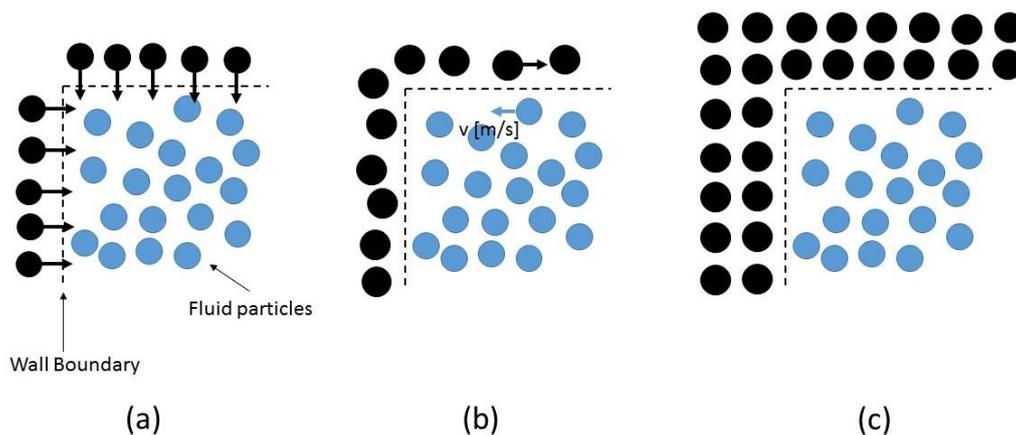
Figure 3.6 Boundary treatment techniques of SPH: (a) repulsive forces, (b) mirror particles, and (c) dummy particles

Monaghan (1994) used a single layer of wall particles that exert central forces on fluid particles. The force between a wall particle and a fluid particle is considered to be the force between molecules, as described by the Lennard-Jones potential. Wall particles exert massive repulsive forces to prevent fluid particles from penetrating. Lee et al. (2008) pointed out that particles may be unsteady and wobbling when they move in parallel with the walls.

Cummins and Rudman (1999) used mirror particles that cannot be seen but have physical properties. When a fluid particle is close to the boundary, mirror particles are generated outside the domain and placed either symmetrically or asymmetrically relative to the fluid particle. While they are given the same density and pressure, their velocity is set to be opposite to that of the fluid particle. The mirror particle method is not suitable for complicated domains, such as a curved boundary or a sharp corner. Moreover, it is necessary to update the position and the properties of mirror particles at each time step.

In this study, a few layers of dummy particles (Shao and Lo, 2003) are placed alongside the wall particles. Dummy particles are virtual and, like mirror particles, are assigned mass and density. However, dummy particles are generally unmovable. When dummy particles are included in the support domain of a fluid particle, they help to increase particle density and keep fluid particles inside the flume.

3.7.3   Neumann condition

The homogeneous Neumann boundary condition is applied to the pressure gradient. The pressure gradient between a wall particle and a dummy particle must be zero. The homogeneous Neumann boundary condition will be met by giving the same pressure value to a dummy particle as the normal direction of the wall particle at a correction time step.

3.7.4   Dirichlet condition

For the pressure calculation, the reference value of the pressure must be determined. The Dirichlet boundary condition specifies that the pressure of free surface particles will be fixed at zero.

3.7.5 No-slip condition

In this study, the velocity on the boundary is assumed to be zero. To meet the no-slip boundary condition, the velocity of wall particles in the first layer and of the dummy particles is fixed at zero. This is a practical technique in SPH and the no-slip condition is approximately satisfied (Asai et al. 2013).

3.7.6 Wave generation boundary

The piston-type wavemaker is described by visible solid particles. Unlike wall particles, these solid particles can move according to the Katell law of solitary wave generation. The position of the wavemaker particles is calculated and updated at each prediction time step. These solid particles are given a velocity. The thickness of the wave generation plate must be sufficient so that the paddle can push fluid particles without leak from the wavemaker boundary. In the following simulations, twenty layers of solid particles are placed to model a wavemaker.

On the left side of the paddle, two layers of dummy particles are arranged. These dummy particles are exceptionally movable though dummy particles are generally unmovable as mentioned in Section 3.7.2. Their positions are updated to keep their initial particle spacing d_0 as the wavemaker particles move right-ward.

Chapter 4   ISPH solver for flows through porous media

4.1   Porous flow

4.1.1   Resistance force

The effect of porous media can be considered as an additional force. Thus, the resistance

force R is added into the momentum equation:

$$\frac{Du}{Dt} = -\frac{1}{\rho}\nabla P + \nu\nabla^2 u + g + \frac{R}{\rho}$$

(4.1.1)

R can be calculated in the following equations (Peng et al. 2017 and Khayyer et al. 2018)

$$R = -\frac{\mu}{Kp}u - \frac{1.75}{\sqrt{150}}\frac{\rho}{\sqrt{Kp}Nw^{\frac{3}{2}}}|u|u$$

$$Kp = \frac{Nw^3 Dc^2}{150(1-Nw)^2}$$

(4.1.2)

where μ is dynamic viscosity, Kp is permeability, Nw is the porosity of porous material,

Dc is a mean grain diameter of porous media.

For a flow inside a porous structure, Kp will be defined and R will be calculated. In

contrast, R becomes zero and vanishes for flow outside a porous medum. In a pure fluid

region, Equation (4.1.1) corresponds to Equation (3.1.1).

4.1.2   Porous media implementation

In this study, porous media are described by dummy particles which have porosity

information. Hereafter, these dummy particles are referred to as porous particles. Figure

4.1 is a model of porous particles comprising a porous block used for a dam breaking

simulation. Wall particles compose solid walls of a water tank and porous particles are

placed in the tank at a particle spacing $\frac{d_0}{\sqrt{Nw}}$. Although the actual mass and density of a

porous medium itself may differ from those of a fluid, the same mass and density values

as fluid particles are given to porous particles for technical practice. This technique can

be accepted since the mass and density of porous structures do not appear in the governing equations and since porous particles will be excluded from the calculation processes of fluid-particle density, velocity and pressure. Porous particles are referred to only when the density of porous media around a target fluid particle is calculated. The details of the calculation processes are presented in Section 4.2.1.
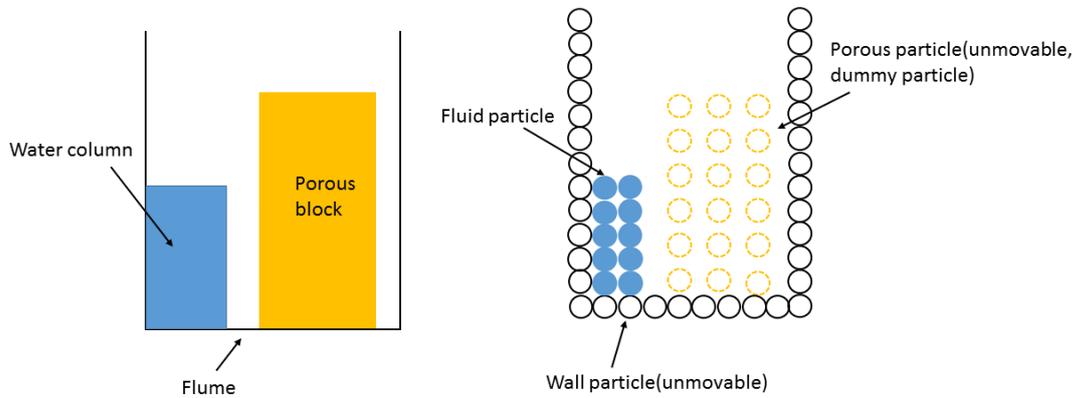
Figure 4.1 Model of porous particles comprising a porous block

4.1.3 Apparent density

Since porous particles cannot be seen physically in a computational domain, fluid particles will occupy the solid skeleton of porous media. To avoid this unphysical situation, the apparent density concept (Akbari, 2014) is adopted. This is a technique to modify the density by

$$\rho_i = Nw\rho_w \tag{4.1.3}$$

where ρ_w is the density in a pure fluid region.

If a fluid particle is in porous media, the apparent density becomes less than ρ_w, which increases the apparent volume of the target particle (Figure 4.2). The particles appear

more sparsely in a porous structure than in a pure fluid region. The density appearing in the SPH operators (see Chapter 3) will be modified by Equation (4.1.3).
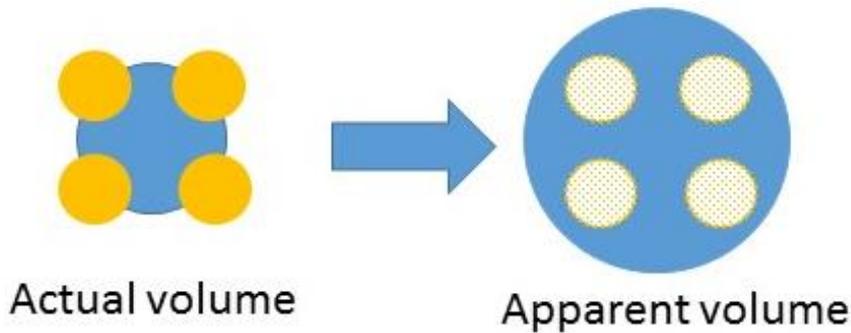
Figure 4.2 Apparent density

4.2   Improved boundary conditions
4.2.1   Water-porous interface

Porosity *Nw* in Eq. (4.1.2) will be problematic if the value of the porosity is fixed. A sudden change of porosity will cause discontinuous velocity and pressure fields. As reviewed in Chapter 2, the transition zone has been developed to conserve the smooth fields, where the porosity is varied manually depending on the smoothing length. Although the thickness of the transition zone is discussed above, the optimal thickness is not consistently determined. Normally, thickness is defined as between two times and four times of the smoothing length (Ren et al., 2016, Gui et al., 2015,b). Since the transition zone is manually established in a computational domain, it is not suitable for the complicated shape of porous media.

In this study, a simpler interface is proposed as a solution that is easy to implement. Similar to Ikari et al. (2015), the apparent porosity of a target water particle *i* is linearly defined in the following equation:

$$Nw_i = 1 - (1 - Nw)\frac{\rho_{pi}}{\rho_w} \tag{4.2.1}$$

where Nw_i is the apparent porosity of the particle i, ρ_{pi} is the density of porous media around the particle i, and ρ_w is the density of a pure fluid.

ρ_{pi} is given by

$$\rho_{pi} = \sum_j m_{pj} W_{ij} \tag{4.2.2}$$

where m_{pj} is the mass of the porous particle j.

If porous particles are found within the compact support, the density of porous media will be calculated.

Nw in Equation (4.2.1) is the physical property and the fixed value of a porous structure, which is given to porous particles and which is different from Nw_i. Equation (4.2.1) means that the apparent porosity is determined how much a porous structure occupies the space around the target particle. Now, Nw in Equation (4.1.2) and Equation (4.1.3) is replaced with Nw_i, except when there is no porous particle around the target particle i. If Equation (4.2.2) yields zero, R is given zero as explained in Section 4.1.1.

The present interface does not need to manually establish any transition and buffer zone. The implementation procedure is simply to add Equation (4.2.1) and Equation (4.2.2) to the programming code. Even if the physical setup of porous media and the smoothing length change, the present interface can be applied flexibly.

4.2.2 Free surface

Particle density is often used to search for free surface particles. If the density satisfies the equation

$$\rho_i^* < b\rho_0 \tag{4.2.3}$$

the particle i is identified as a particle on the free surface, and the pressure of the particle will be zero. b is a free surface coefficient, and it is generally set to be around 0.96-0.99. The initial density is generally fixed at any time step. However, due to the apparent density, the particle density always becomes smaller than $b\rho_0$ in a porous region, even though the target particle is not on a free surface. As stated in Section 3.7.4, the pressure of a free surface particle must be zero to satisfy the Dirichlet boundary condition. Consequently, the pressure inside porous media becomes entirely zero.
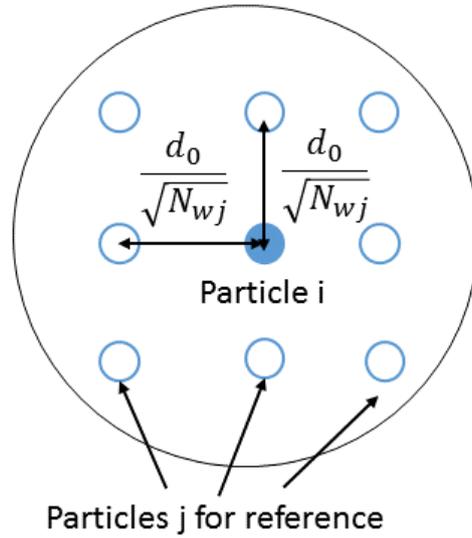
Figure 4.3 Virtual neighbouring particles for calculating reference density

In this study, the new boundary condition is presented to detect free surface particles correctly. At each time step, reference particles j are virtually and regularly placed around the target particle i with the porosity-corrected particle spacing $\dfrac{d_0}{\sqrt{Nw_j}}$ (Figure 4.3). The density of the target particle i density is calculated at each time step as follows:

$$\rho_i{}^{Reference} = \sum_j \rho_j \left(\frac{d_0}{\sqrt{N_{wj}}}\right)^2 W_{ij}{}^{Reference}$$

(4.2.4)

$$W_{ij}{}^{Reference} = W\left(\left|r_j{}^{Reference} - r_i\right|, h\right)$$

The density $\rho_i^{Reference}$ is considered as a reference of the inner particle density. The new condition is

$$\frac{\rho_i}{\rho_i^{Reference}} < 1.0 \tag{4.2.5}$$

If Equation (4.2.5) is met, the particle i is identified as a free surface particle.

4.3   Setting of smoothing length

In the simulations with porous media, the smoothing length is defined as $\frac{h}{\sqrt{Nw}}$ no matter where a fluid particle is. This definition is different from Akbari's (2014) who states that the smoothing length varies depending on porosity.

As explained in Chapter 3, the smoothing length is an essential factor to determine the range of the support domain. The smoothing length needs to be set by taking symmetry into consideration for the consistent integral interpolation. If the kernel length varies according to different degrees of porosity, particle j might not be a neighbour to particle i, while particle i can be regarded as a neighbouring particle of particle j. Consequently, the integral calculations will fail in the conservation of physical properties.

4.4   Hybrid source term in PPE

The standard source term of PPE has been widely used in ISPH as stated in Chapter 3. However, it has been pointed out that the calculated density of particle i would not be exactly equal to ρ_0 at each time step due to the numerical errors of the SPH approximation and discretization (Khayyer et al. 2009). This discrepancy can result in severe fluctuation of the pressure field. Khayyer et al. (2009) proposed a new approach,

the HS scheme, to eliminate numerical errors and to obtain a more accurate pressure field.

The HS source term is derived from the derivative of Equation (3.4.6)

$$\left(\frac{D\rho}{Dt}\right)_i^* = \left(\sum_j m_j \frac{DW_{ij}}{Dt}\right)_i^*$$

$$= \left(\sum_j m_j \nabla_i W_{ij} \cdot \boldsymbol{u}_{ij}\right)_j^* \tag{4.4.1}$$

The PPE can be written as

$$\nabla \cdot \left(\frac{1}{\rho_*}\nabla P_{t+1}\right)_i = \frac{1}{\rho_0 \Delta t}\left(\sum_j m_j \nabla_i W_{ij} \cdot \boldsymbol{u}_{ij}\right)_i^* \tag{4.4.2}$$

Since the HS source term does not contain any density calculation process, pressure fluctuations can be eliminated. However, the fluid volume cannot be exactly conserved in the HS scheme; thus, the calculation becomes unstable for a long computational time. To overcome the weakness of both the Standard source term and the HS source term, the hybrid source term was developed (Asai et al. 2012, Koh et al. 2013, Gui et al. 2015). The modified PPE can be

$$\nabla \cdot \left(\frac{1}{\rho_*}\nabla P_{t+1}\right)_i = \gamma \frac{1}{\rho_0 \Delta t}\left(\sum_j m_j \nabla_i W_{ij} \cdot \boldsymbol{u}_{ij}\right)_i^* + (1 - \gamma)\frac{\rho_0 - \rho_*}{\rho_0 \Delta t^2} \tag{4.4.3}$$

Where γ is the combination ratio. The effect of the hybrid source term is discussed in Chapter 5 and Chapter 6.

4.5   Algorithm

In this study, simulations are performed by Fortran codes. Figure 4.4 summarises the algorithm of the present ISPH model. First of all, the initial conditions of simulation are set up. The parameters of computation are given, such as the diameter of the particle, the

smoothing length and, the mean grain size of porous media. These values are fixed and will never change during computation. Particles are placed at the initial particle spacing. Once all particles are configured, the neighbouring particles of each particle are searched. If porous particles are included in a support domain of a target fluid particle, the apparent particle porosity is defined.

At the prediction step, temporal velocity and position are obtained from the viscous terms and from the external (gravitational) terms of the governing equation. If porous media interact with fluid, the additional resistance force can be calculated in the prediction step. At the end of the prediction step, the CFL condition is checked. If a particle moves too fast, the time increment will be automatically adjusted to satisfy the CFL condition, and the prediction step will be done all over again. When the prediction time step is completed, neighbouring particles of the target particle are searched again. The initial density is calculated assuming that all the fluid particles are inner particles. In the correction step, the PPE is solved to obtain the pressure. Using the solution of the PPE, velocity and position at the next time step is modified. If the CFL condition is met, the calculation process at the current time step will be completed. The loop will be repeated for the determined time step.

```
┌─────────────────────────┐
│  Set up initial conditions │
└─────────────────────────┘
             │
             ▼
┌─────────────────────────┐ ◄──────┐
│   Search neighbouring   │        │
│        particles        │        │
└─────────────────────────┘        │
             │                     │
             ▼                     │
┌─────────────────────────┐        │
│   Define the particle   │        │
│        porosity         │        │
└─────────────────────────┘        │
             │                     │
             ▼                     │
┌─────────────────────────┐        │
│  Calculate the temporal │        │
│  velocity and position  │        │
└─────────────────────────┘        │
             │                     │
             ▼                     │
┌─────────────────────────┐        │
│  Obtain the information  │        │
│ of neighbouring particles │      │
└─────────────────────────┘        │
             │                     │
             ▼                     │
┌─────────────────────────┐        │
│ Update the initial density │     │
└─────────────────────────┘        │
             │                     │
             ▼                     │
┌─────────────────────────┐        │
│      Solve the PPE      │        │
└─────────────────────────┘        │
             │                     │
             ▼                     │
┌─────────────────────────┐        │
│   Modify the velocity and │      │
│        porisition       │        │
└─────────────────────────┘        │
             │                     │
             ▼                     │
┌─────────────────────────┐        │
│   Reset the relevant    │ ───────┘
│        variables        │
└─────────────────────────┘
             │
             ▼
┌─────────────────────────┐
│     Stop calculation    │
└─────────────────────────┘
```
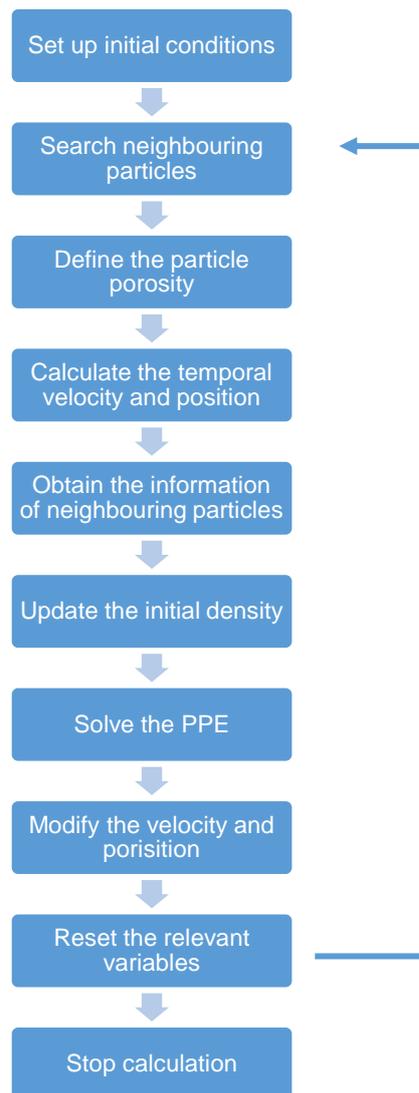
Figure 4.4 Code structure of the present ISPH

4.6   Discussion of kernels and source term

4.6.1   Non-breaking wave

The basics of kernel functions are explained in Chapter 3. In this section, the combination

of the kernels and the source term is discussed. As reviewed in Chapter 2, the hybrid

source term has been developed by some researchers. For instance, Asai et al. (2012) used

the quintic spline kernel, while the B-spline kernel was adopted in the research of Gui et

al. (2015, a). In this section, the Wendland kernel is compared to the B-spline kernel to

reveal the effects of the kernel and the source term in terms of the accurate pressure field. A solitary wave was generated in the two different wave flumes to observe both non-breaking and breaking waves on a slope. The computational domain is much smaller than actual coastal defences because of computational load. The initial water depth and the wave height are set to match existing experimental data. The following four sets of a kernel and a source term were tested for each wave:

(1) B-spline kernel and standard source term only

(2) B-spline kernel and hybrid source term

(3) Wendland kernel and standard source term only

(4) Wendland kernel and hybrid source term

The setting of the computational domain is described in Figure 4.5. All of the walls and bottoms are solid. The bottom is 2.07 m long and the scale of the slope is 1:2.08. The total horizontal length of the wave flume is approximately 3.0 m. The mean water depth was set to be 0.21 m. The wave is generated at the left side of the flume, and the normalised wave height H/h_0 will be 0.163. The wave is expected not to break while it propagates on the slope. Following the work of Gui et al. (2015, a), the combination ratio γ of the hybrid source term was fixed at 0.97. Although other values such as 0.99 and 0.95 were tested, they resulted in computational instability and eventually computation stopped. The parameters of computing are listed in Table 4.1. Practically, around 20-30 particles are needed in the vertical direction to describe water in a flume, so that those particles are not affected by the unphysical interaction with wall particles. The particle diameter is set to be 0.005 m to satisfy this condition and to make the size round number. The smoothing length is set to be around 1.2-1.4 times as the particle diameter. Once the particle size and

the smoothing length are determined, the initial time step should be 1/5 to 1/20 of the particle size because particles might penetrate the walls if the initial time is too large. Smagorinsky coefficient is set at 0.1, following Gotoh et al. (2004) who developed the SPS model for SPH. 0.15 and 0.2 were also tested. However, they did not affect the results.
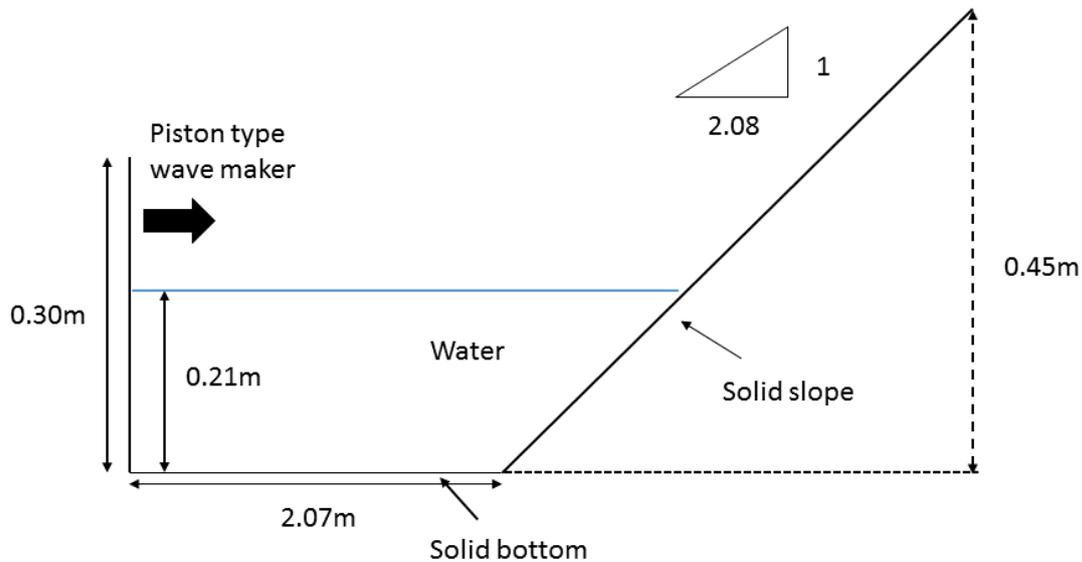

Figure 4.5 Setting of a 1:2.08 slope flume

Table 4.1 Computational parameters for non-breaking waves on a solid slope

Parameters	Value
Diameter of particles	0.005 m
Initial particle spacing	0.005 m
Smoothing length	0.006 m
Initial time step	0.00025 sec
Smagorinsky coefficient	0.1
Courant number	0.2

Figure 4.6 shows the pressure field of the B-spline kernel with the standard source term. At $t = 2.00$ [s], the pressure of the wavemaker particles unphysically exceeds 3000 Pa at the bottom. After $t = 2.50$ [s], the pressure looks discontinuous at the left side and there are some pressure fluctuations around the free surface. If the HS source term is added, the pressure will never exceed 3000 Pa, and the continuous pressure fields are yielded (Figure 4.7). However, even with the HS source term, the pressure fluctuations of particles around the free surface cannot be eliminated completely.

(a) $t = 1.50$ [s]

(b) $t = 2.00$ [s]

(c) $t = 2.50$ [s]

Solitary Wave

(d) $t = 3.00$ [s]

Solitary Wave

(e) $t = 3.50$ [s]

## Solitary Wave

(f) $t = 4.00$ [s]

Figure 4.6 Pressure fields produced by the B-spline kernel and the standard source term

for a 1:2.08 solid slope

Solitary Wave

(a) $t = 1.50$ [s]
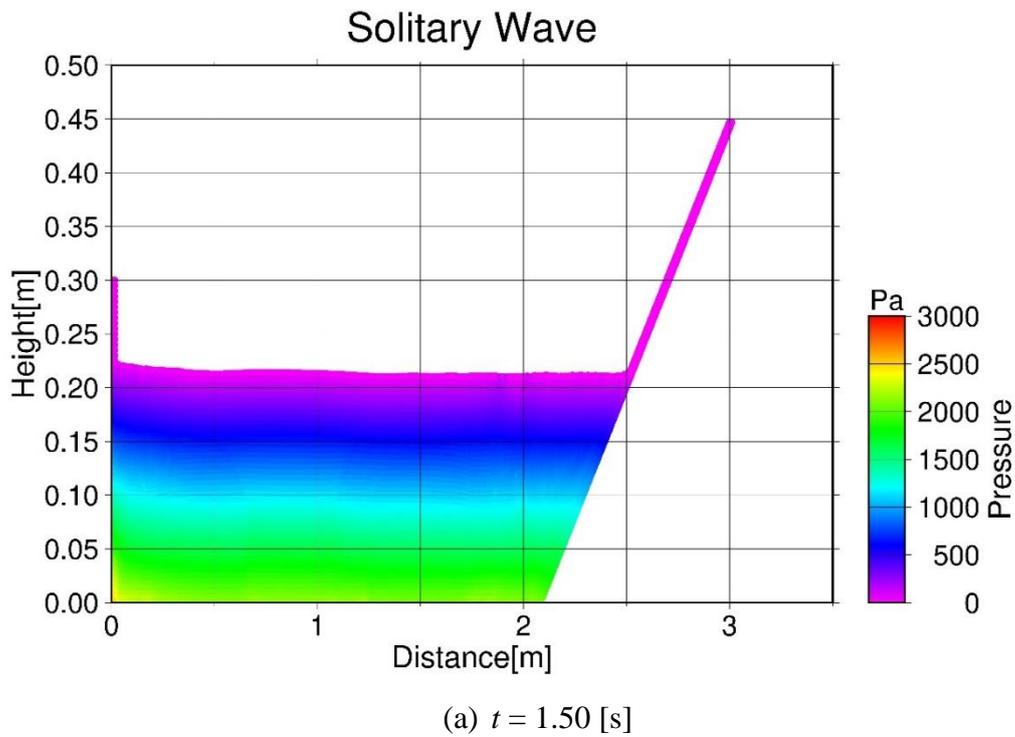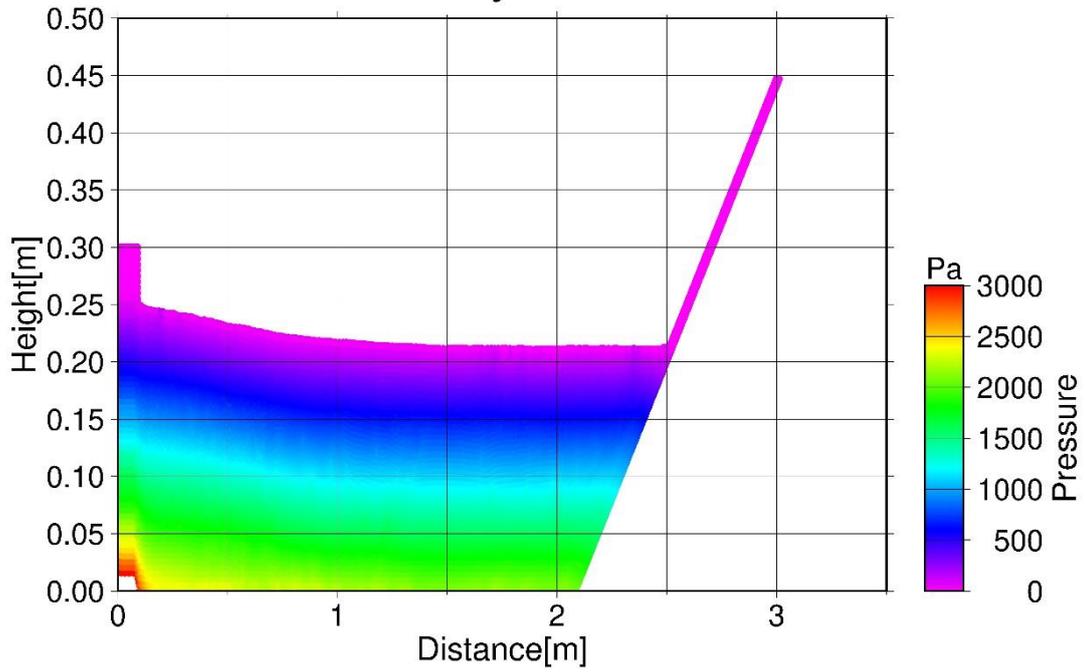
Solitary Wave

(b) $t = 2.00$ [s]

Solitary Wave

(c) $t = 2.50$ [s]

63
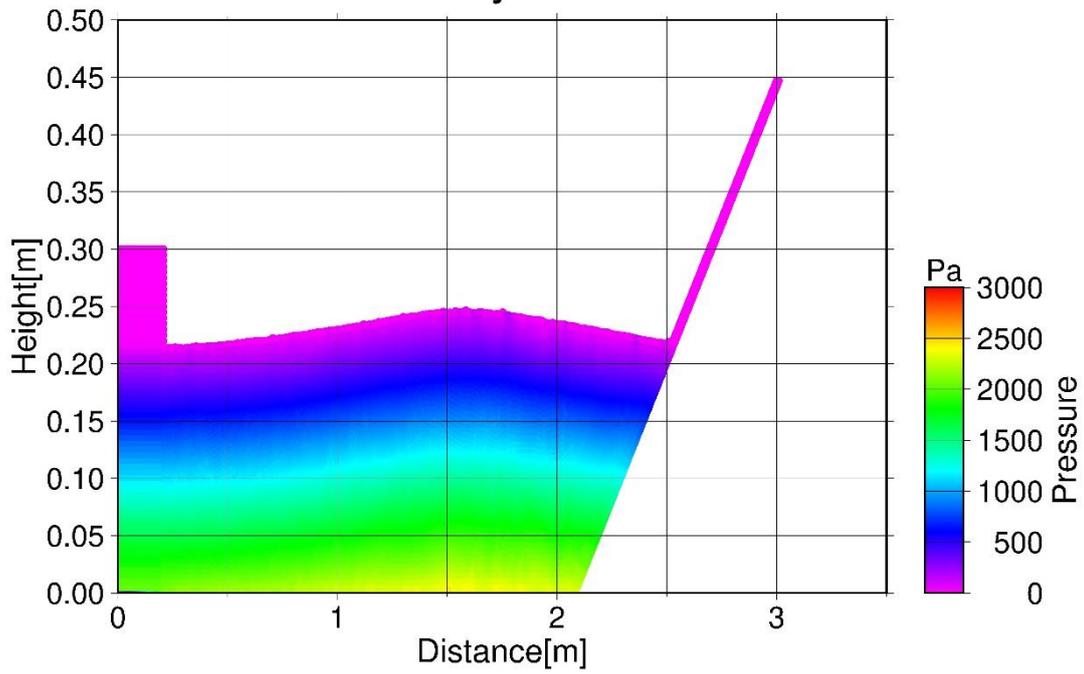
(d) $t = 3.00$ [s]
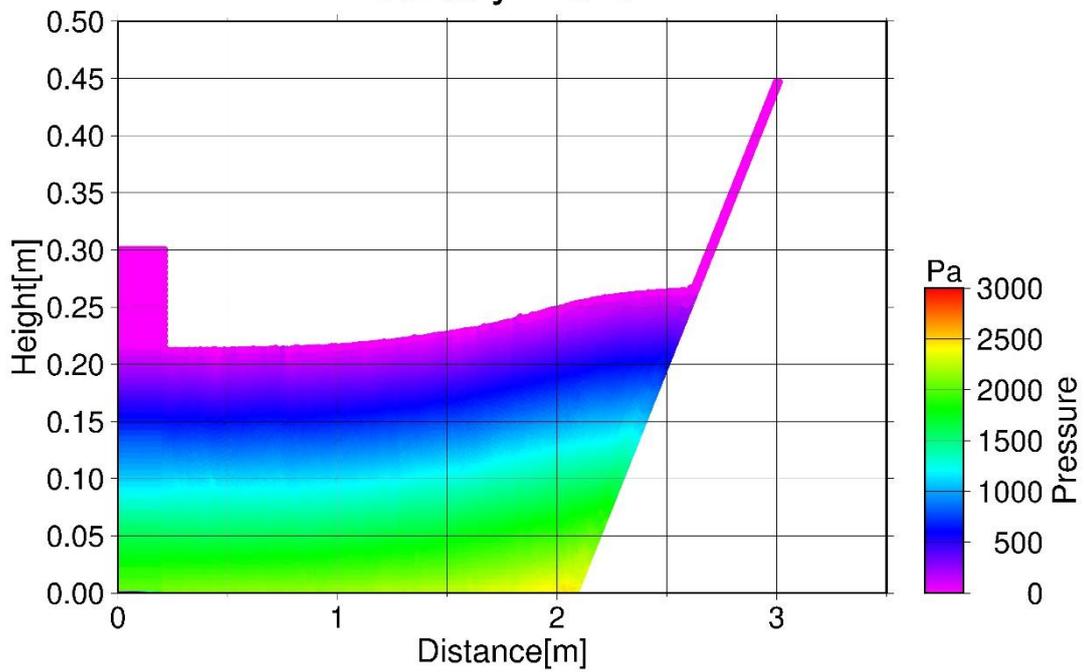
(e) $t = 3.50$ [s]

(f) $t = 4.00$ [s]
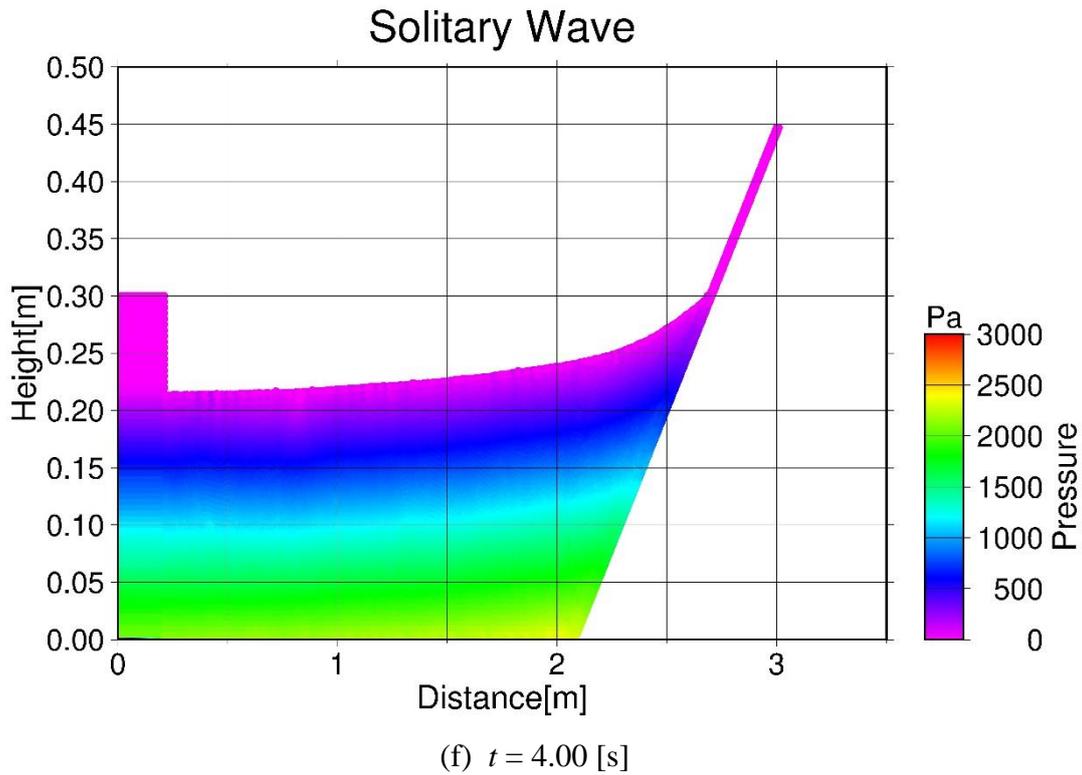
Figure 4.7 Pressure fields produced by the B-spline kernel and the hybrid source

term for a 1:2.08 solid slope

The results of the Wendland kernel with the standard source term and with the hybrid

source term are shown in Figure 4.8 and Figure 4.9, respectively. Figure 4.8 (c) shows

that the Wendland kernel was successful in preventing the excess pressure at the bottom

of the wavemaker particles compared to the pressure field presented in Figure 4.6 (c).

However, there is almost no difference of the pressure field between Figure 4.8 and Figure

4.9. For non-breaking waves, the source term of the PPE does not affect the smooth

pressure field in a dominant way, whereas the Wendland kernel is superior to the B-spline

kernel.
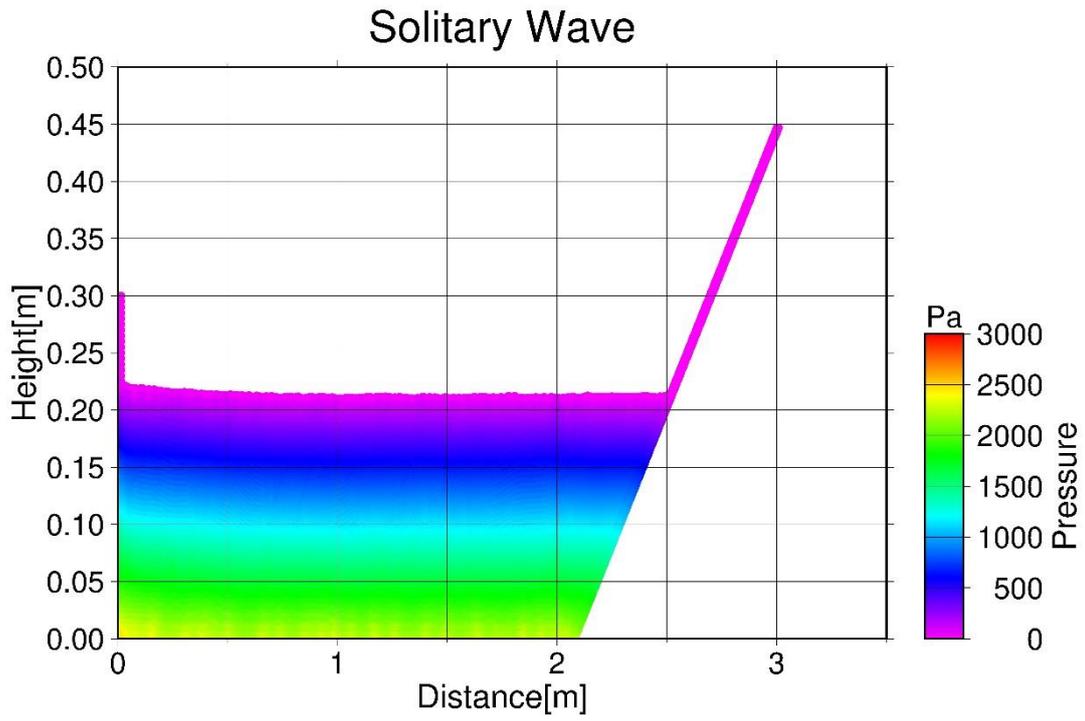
(a) $t = 1.50$ [s]
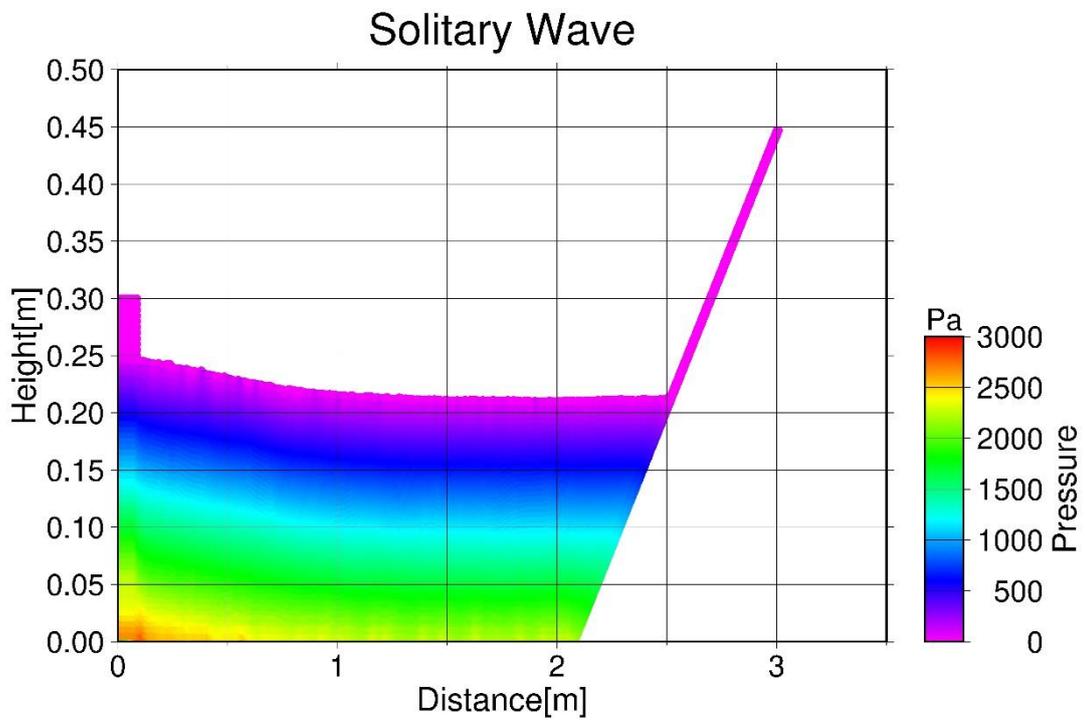
(b) $t = 2.00$ [s]
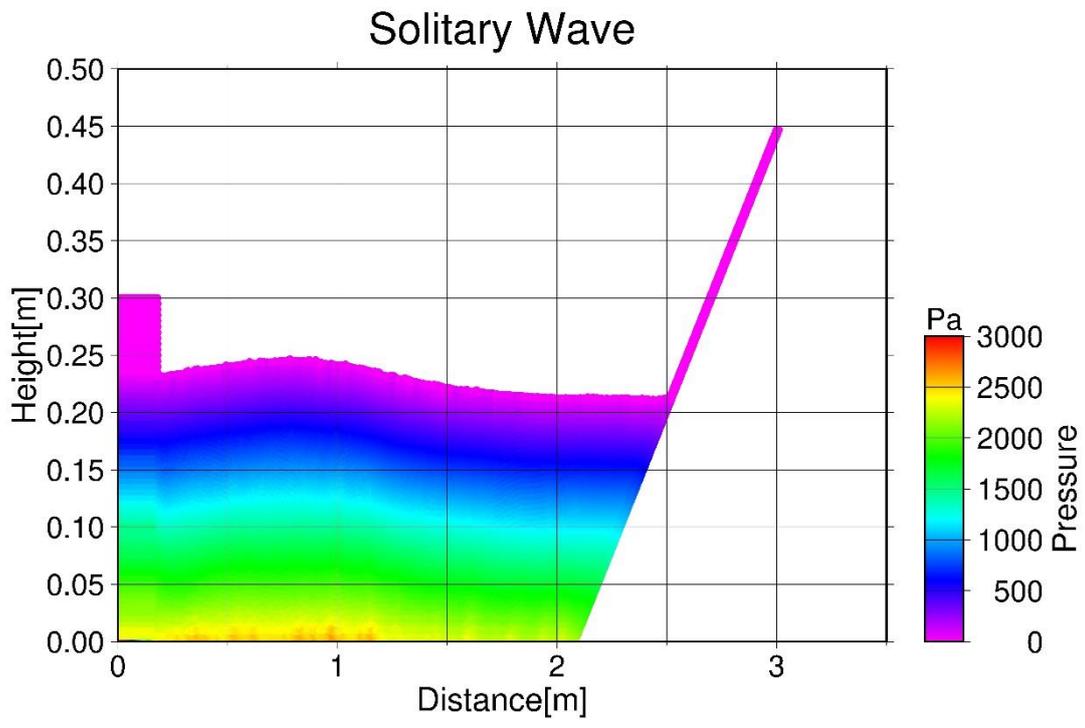
(c) $t = 2.50$ [s]
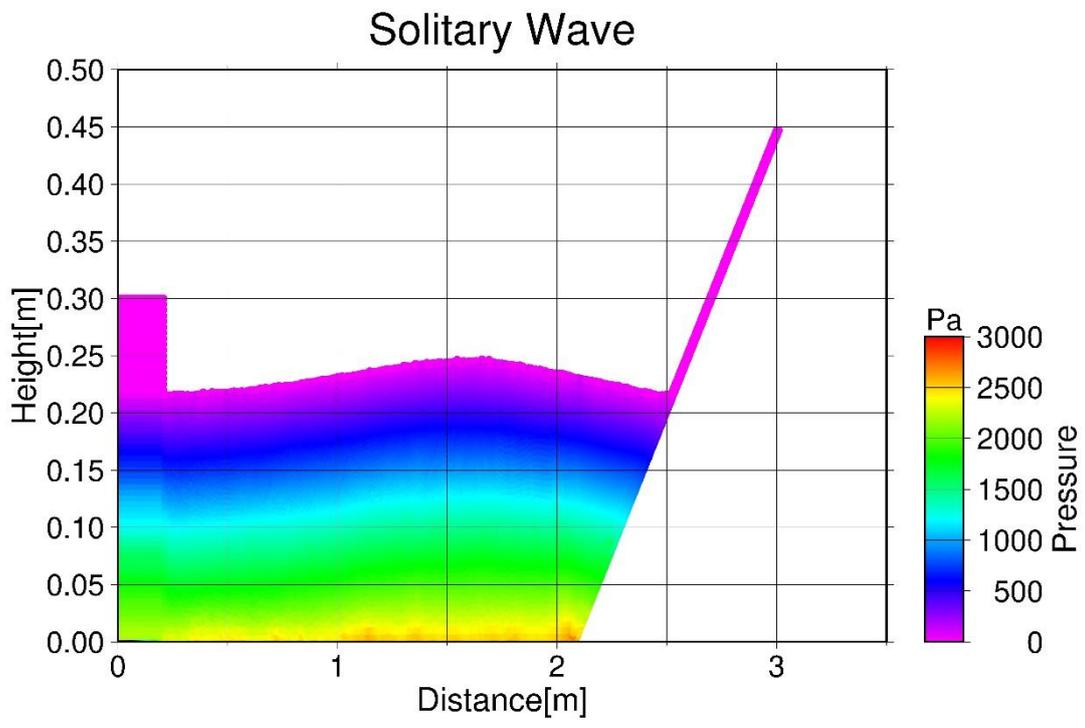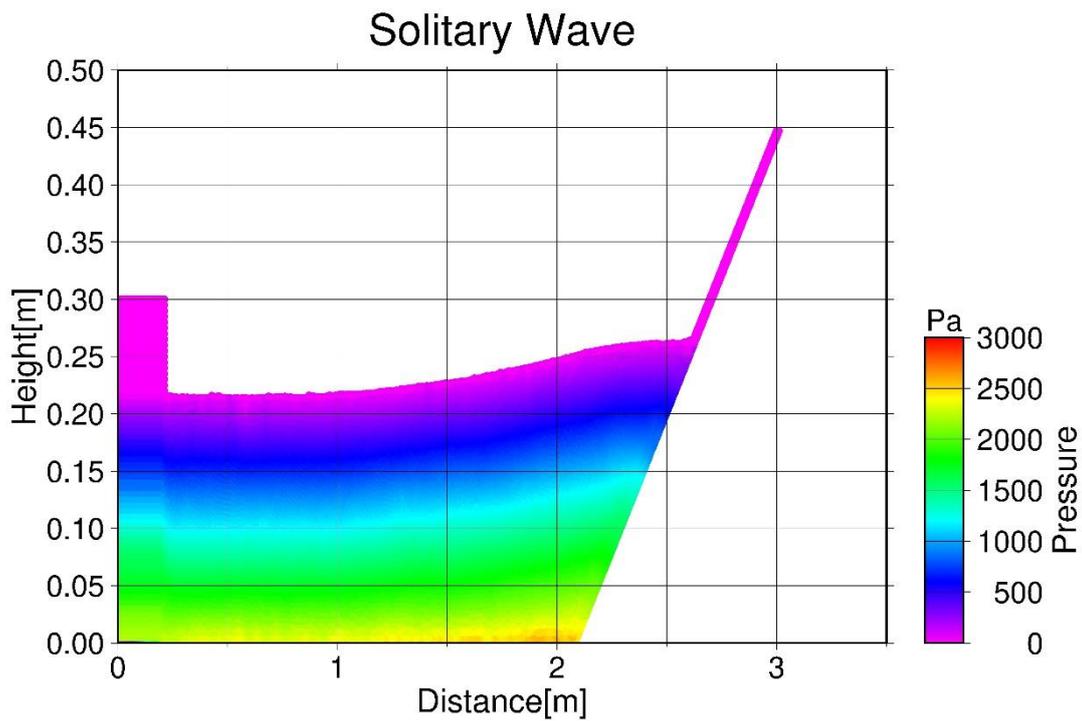
(d) $t = 3.00$ [s]

(e) $t = 3.50$ [s]
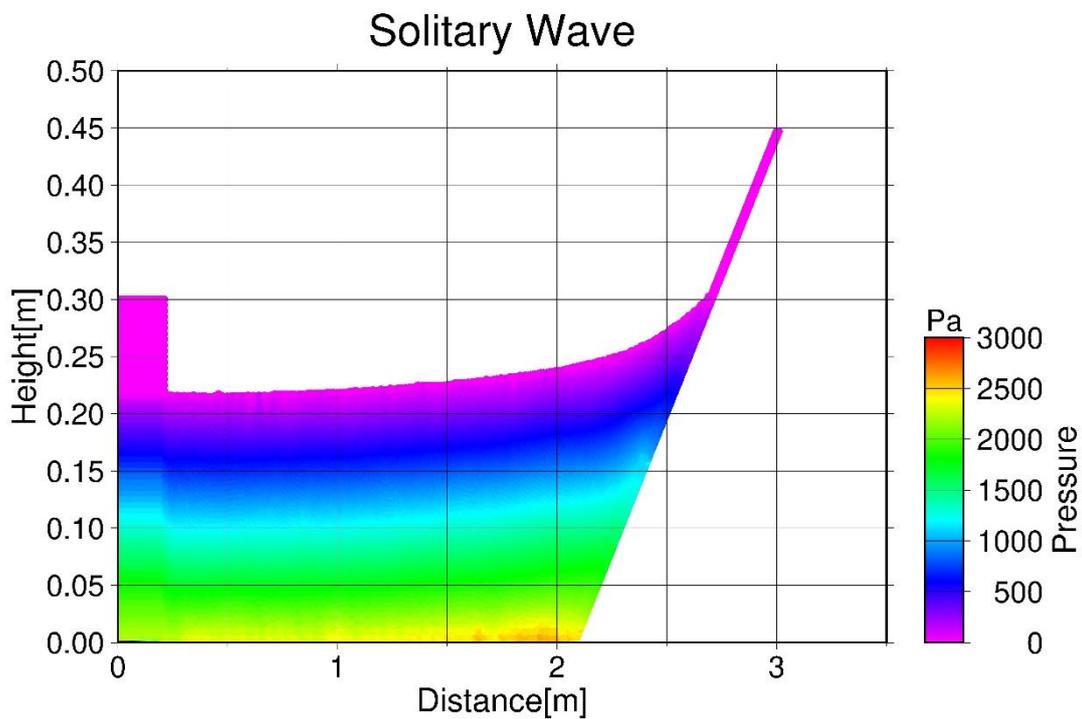
(f) $t = 4.00$ [s]

Figure 4.8 Pressure fields produced by the Wendland kernel and the standard source

term for a 1:2.08 solid slope

(a) $t = 1.50$ [s]

(b) $t = 2.00$ [s]

(c) $t = 2.50$ [s]

(d) $t = 3.00$ [s]

70

Solitary Wave

(e) $t = 3.50$ [s]

Solitary Wave

(f) $t = 4.00$ [s]

Figure 4.9 Pressure fields produced by the Wendland kernel and the hybrid source term

for a 1:2.08 solid slope

4.6.2　　　　　Breaking wave

The setting of the computational domain is illustrated in Figure 4.10. All of the walls and bottoms are solid as well as the non-breaking wave cases. The flat bottom length is 2.00 m and the scale of the slope is 1:20. The total horizontal length of the wave flume is approximately 10.0 m. The mean water depth is 0.21 m. The normalised wave height H/h_0 was 0.28. The wave is expected to break while it runs upon the slope. The combination ratio γ of the hybrid source term was set to be 0.97. The parameters of computing are listed in Table 4.2.
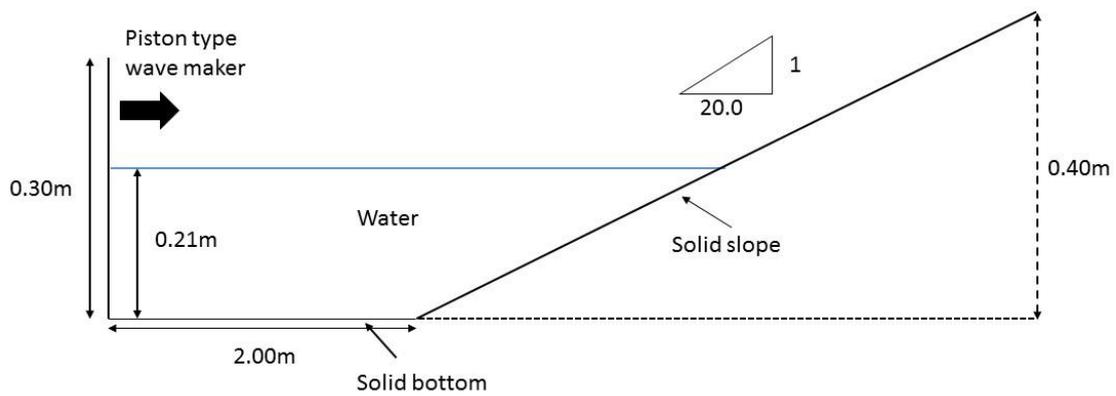
Figure 4.10 Setting of a 1:2.08 slope flume

Table 4.2 Computational parameters for breaking waves on a solid slope

Parameters	Value
Diameter of particles	0.005 m
Initial particle spacing	0.005 m
Smoothing length	0.006 m
Initial time step	0.00025 sec
Smagorinsky coefficient	0.1
Courant number	0.2

Figure 4.11 shows the pressure fields of a breaking wave yielded by the B-spline kernel and the standard source term. During the wave generation process, the pressure fluctuated, particularly under the wave crest. In contrast, the hydrostatic pressure could be observed on the right side of the wave flume until $t = 2.50$ [s]. However, the pressure disturbance can be seen everywhere in the wave flume after the wave started to break on the slope at $t = 4.0$ [s]. If the source term is the hybrid one, the pressure field will be drastically smoothed (Figure 4.12). Although there were some fluctuations after $t = 5.50$ [s], the violent disturbance of the pressure was eliminated, and the overall results were acceptable.

(a) $t = 1.50$ [s]

(b) $t = 2.50$ [s]

(c) $t = 4.00$ [s]

(d) $t = 5.50$ [s]

(e) $t = 7.00$ [s]

(f) $t = 8.25$ [s]

Figure 4.11 Pressure fields produced by the B-spline kernel and the standard source

term for a 1:20 scale slope
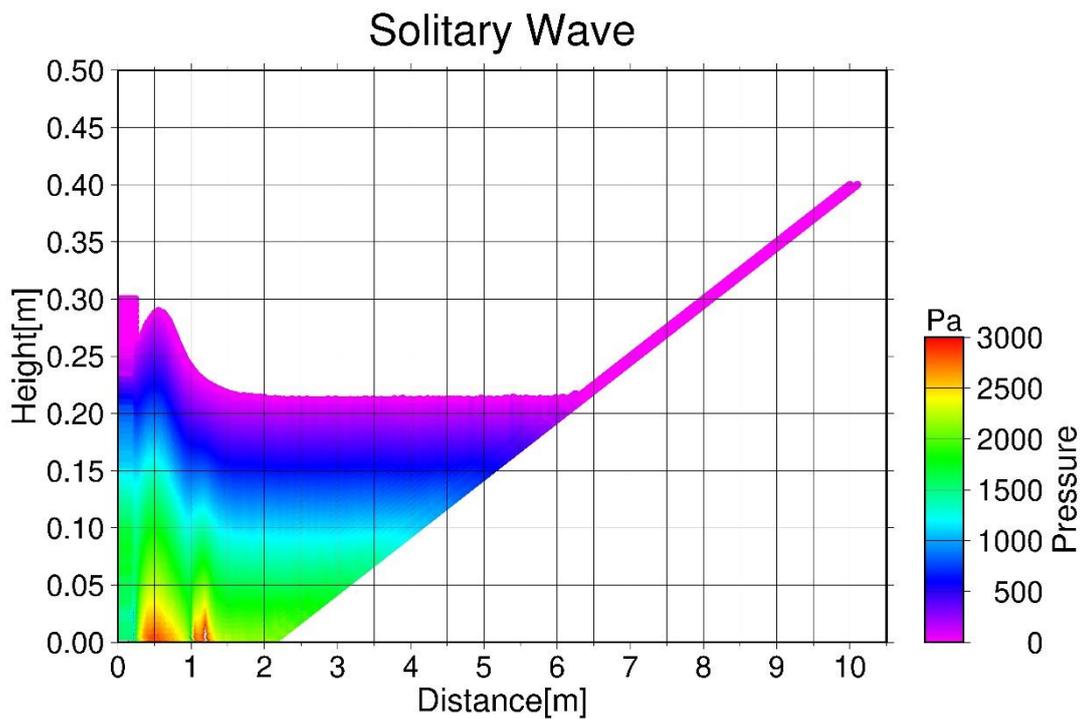
(a) $t = 1.50$ [s]
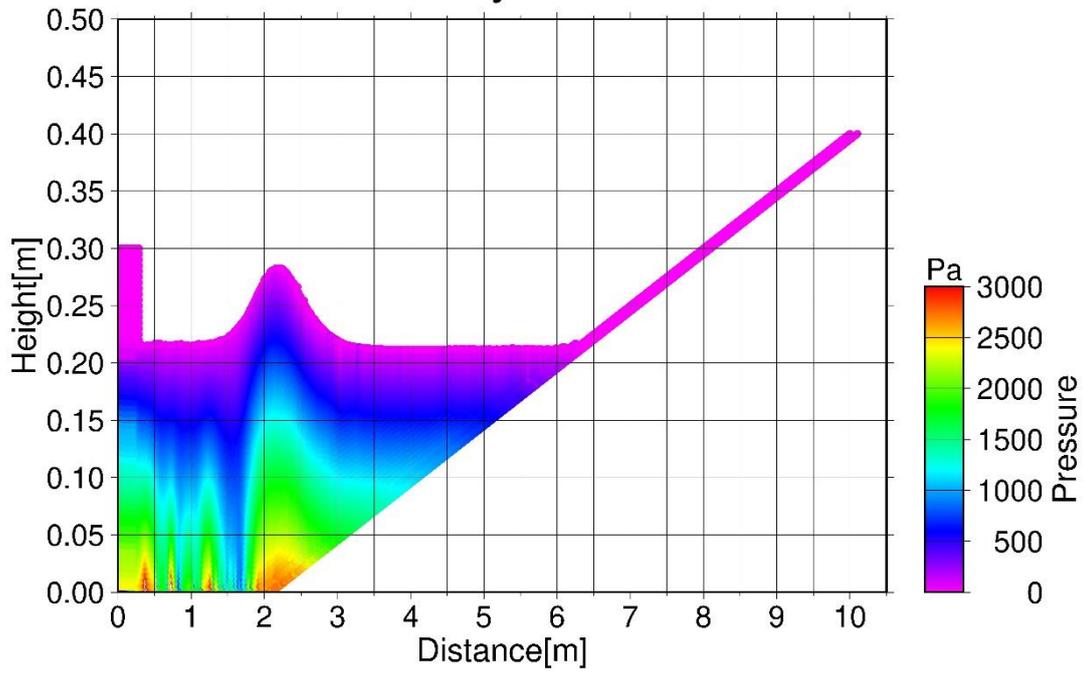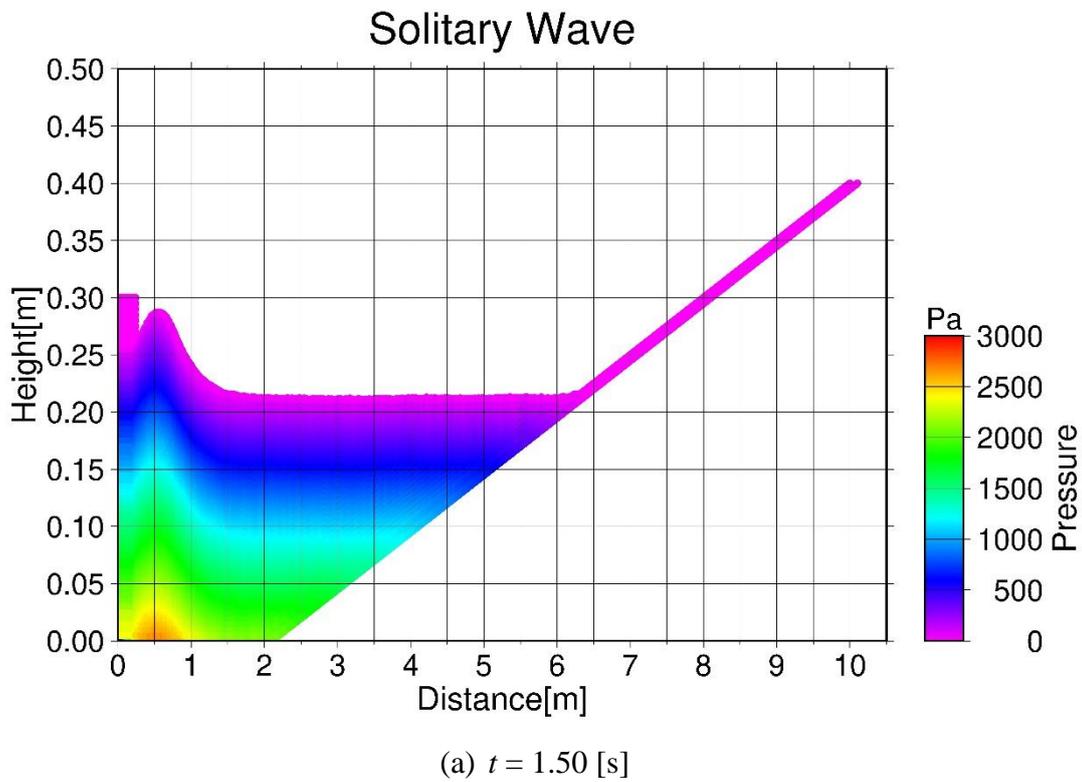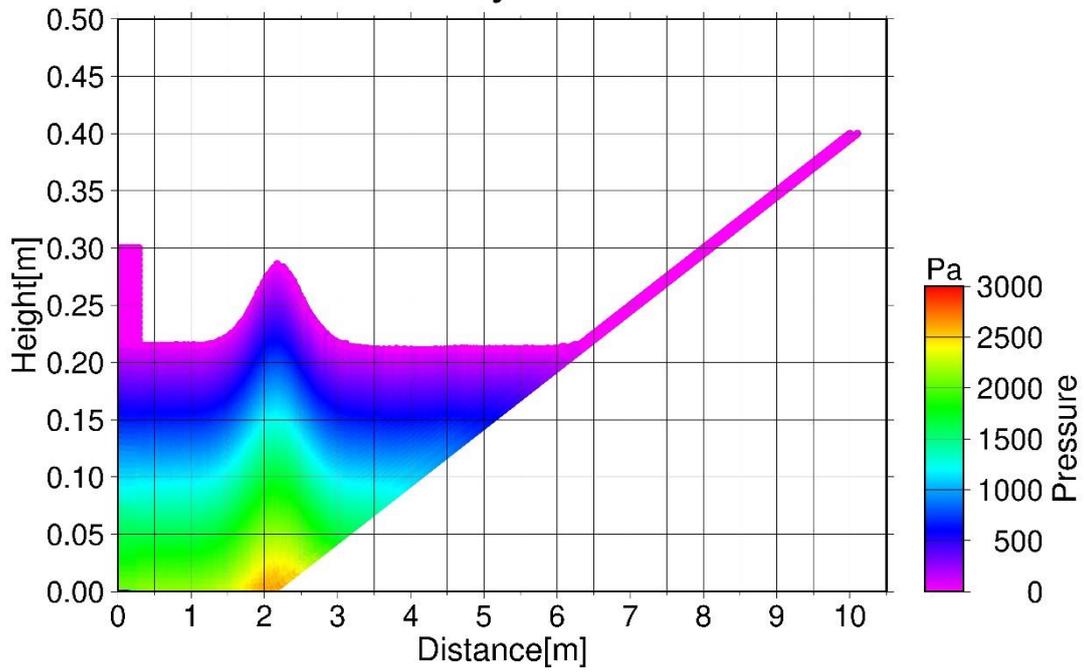
Solitary Wave

(b) $t = 2.50$ [s]

Solitary Wave
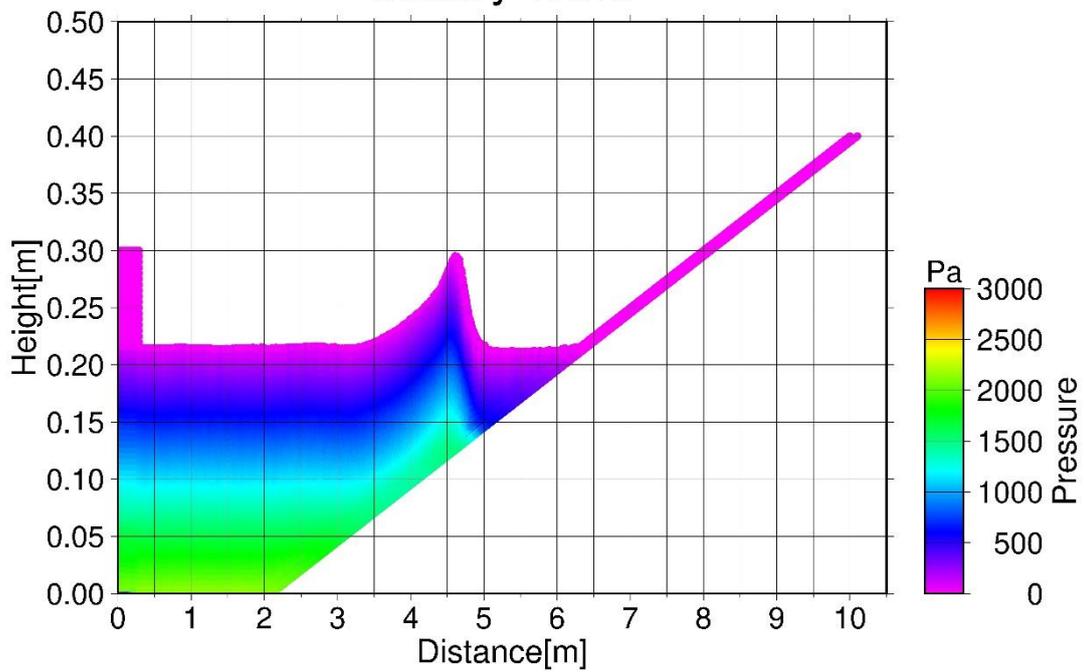
(c) $t = 4.00$ [s]
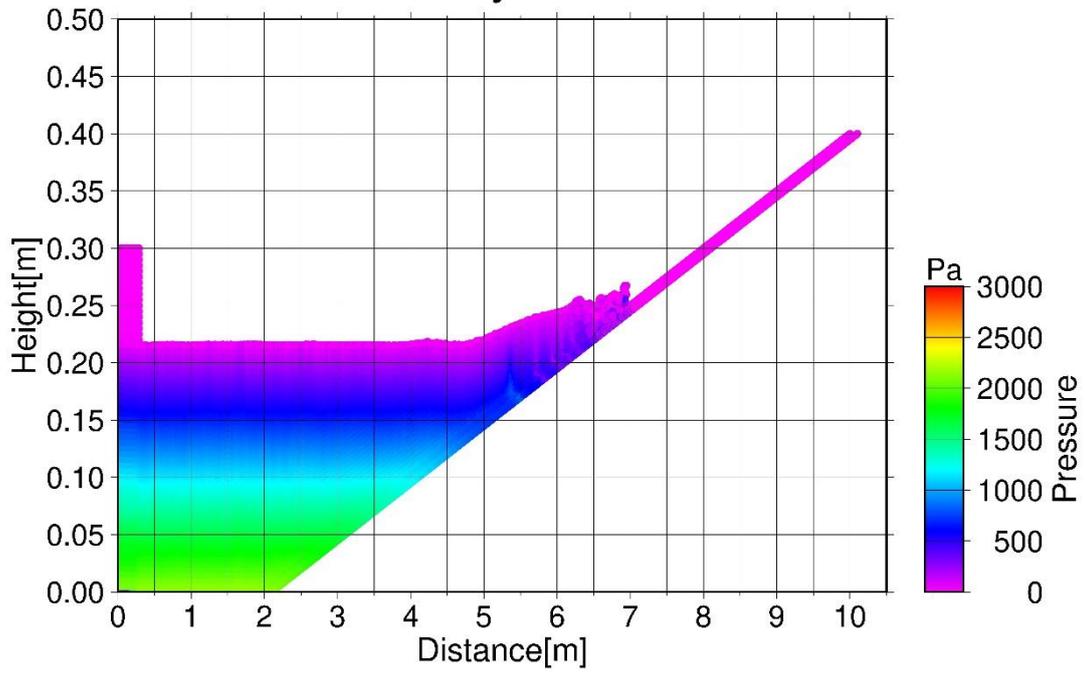
Solitary Wave

(d) $t = 5.50$ [s]

Solitary Wave

(e) $t = 7.00$ [s]

Solitary Wave
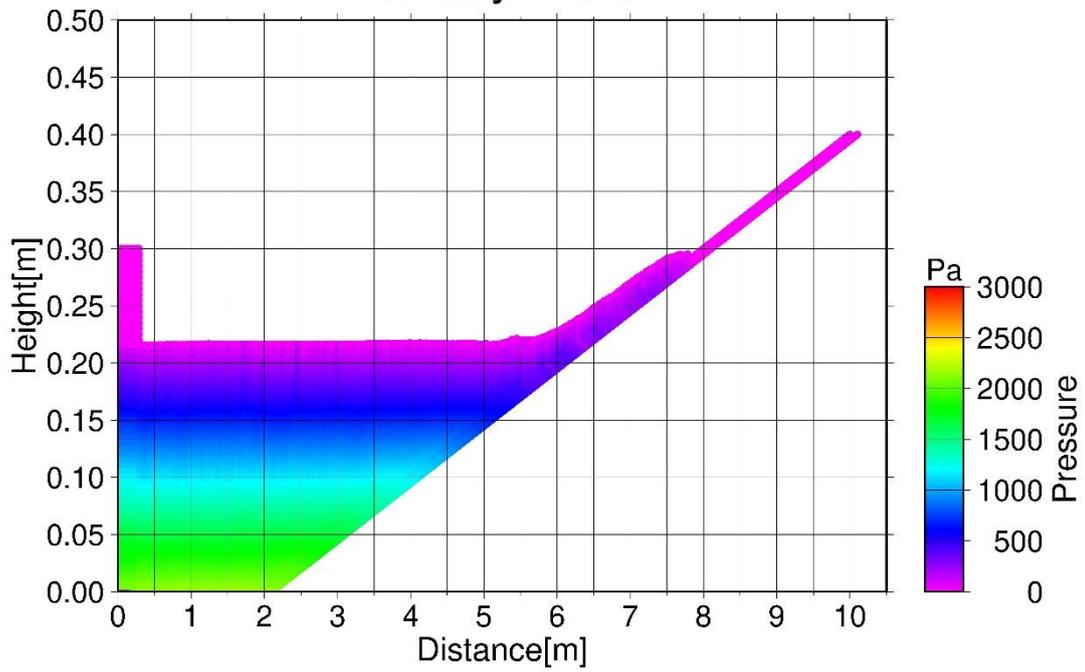
(f) $t = 8.25$ [s]
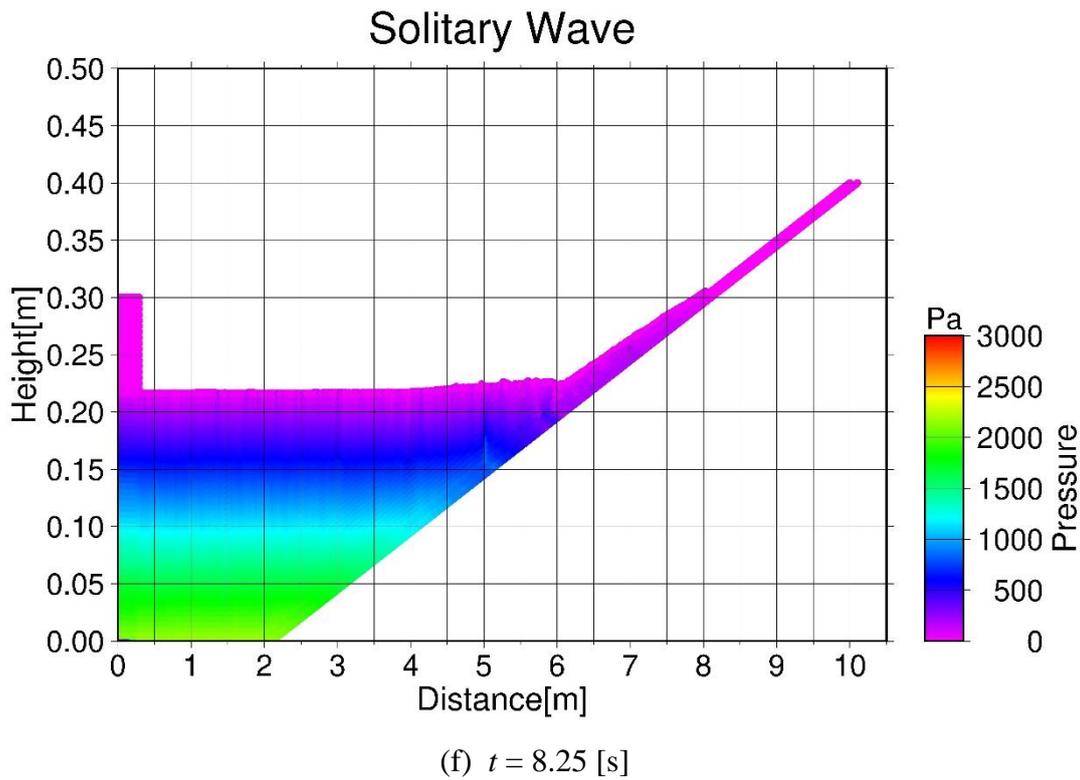
Figure 4.12 Pressure fields produced by the B-spline kernel and the hybrid source term

for a 1:20 scale slope

The results of the Wendland kernel with the standard source term and the hybrid source term are summarized in Figure 4.13 and Figure 4.14, respectively. Compared with the pressure field shown in Figure 4.11, it is noted that the Wendland kernel can give accurate pressure fields even without the HS source term. Adopting the hybrid source term results in the small pressure fluctuations being eliminated. For instance, a comparison of Figure 4.14 (b) with Figure 4.13 (b) shows that the pressure around the wave crest is smoother, and that the maximum pressure at the bottom is slightly smaller.
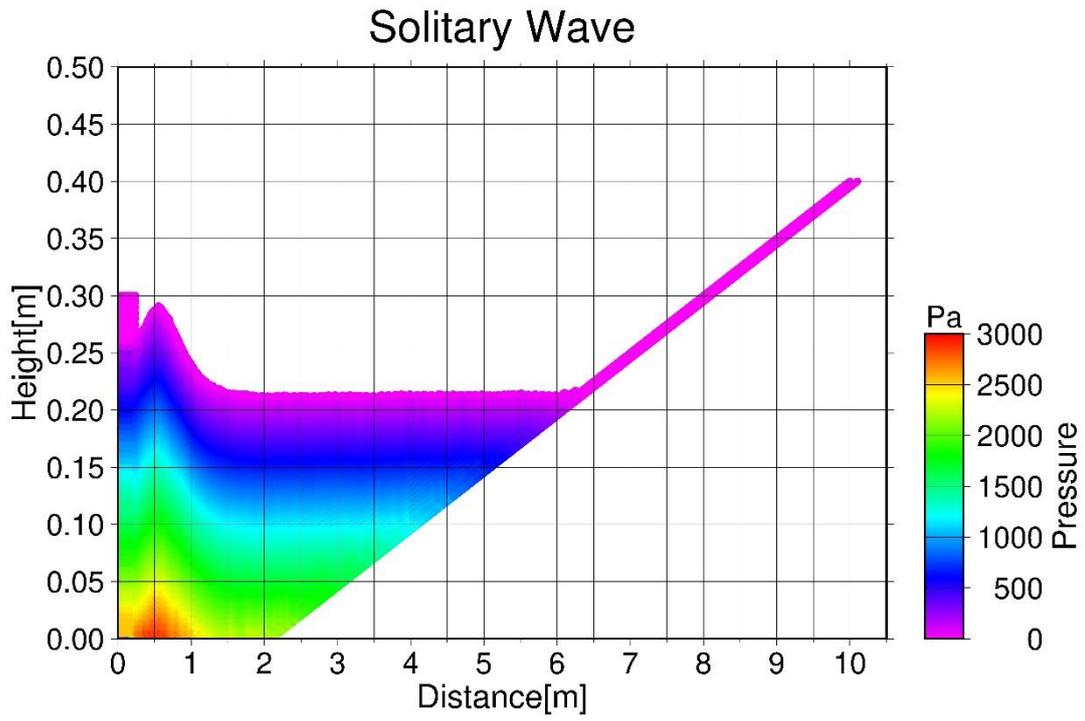
(a) $t = 1.50$ [s]
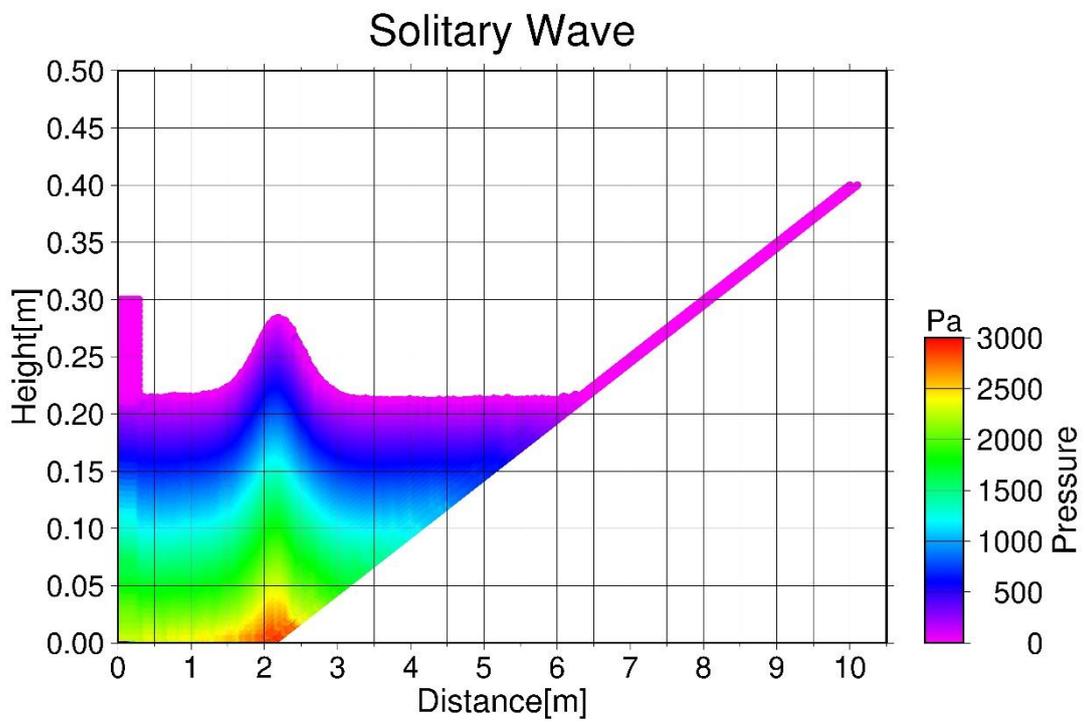
(b) $t = 2.50$ [s]
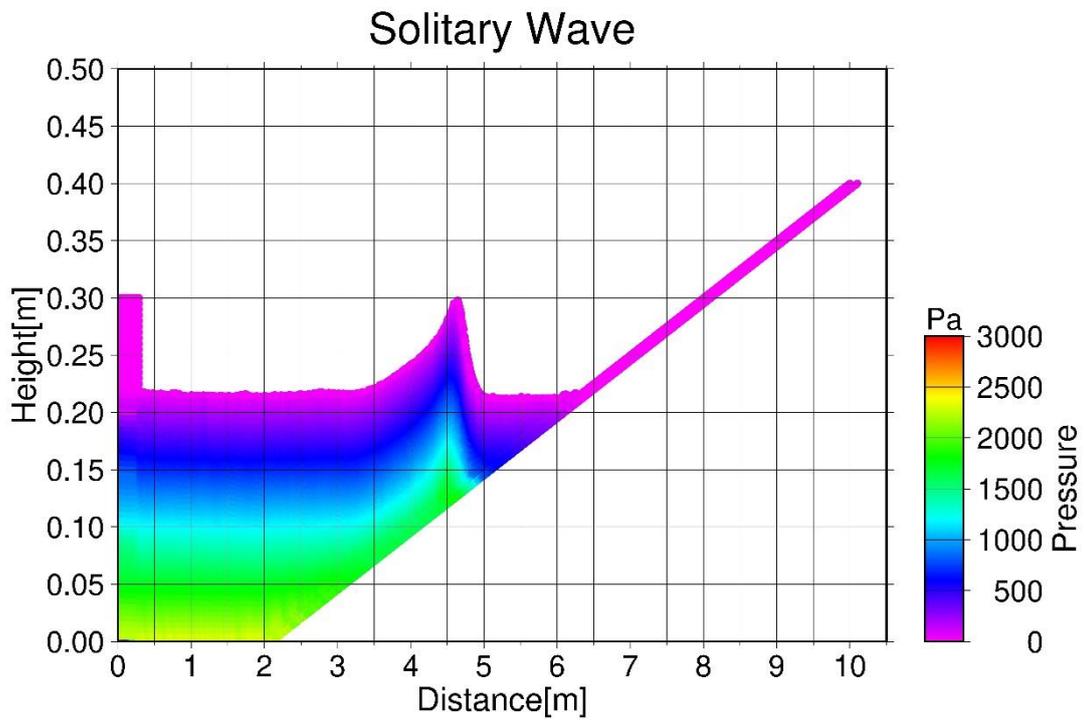
(c) $t = 4.00$ [s]
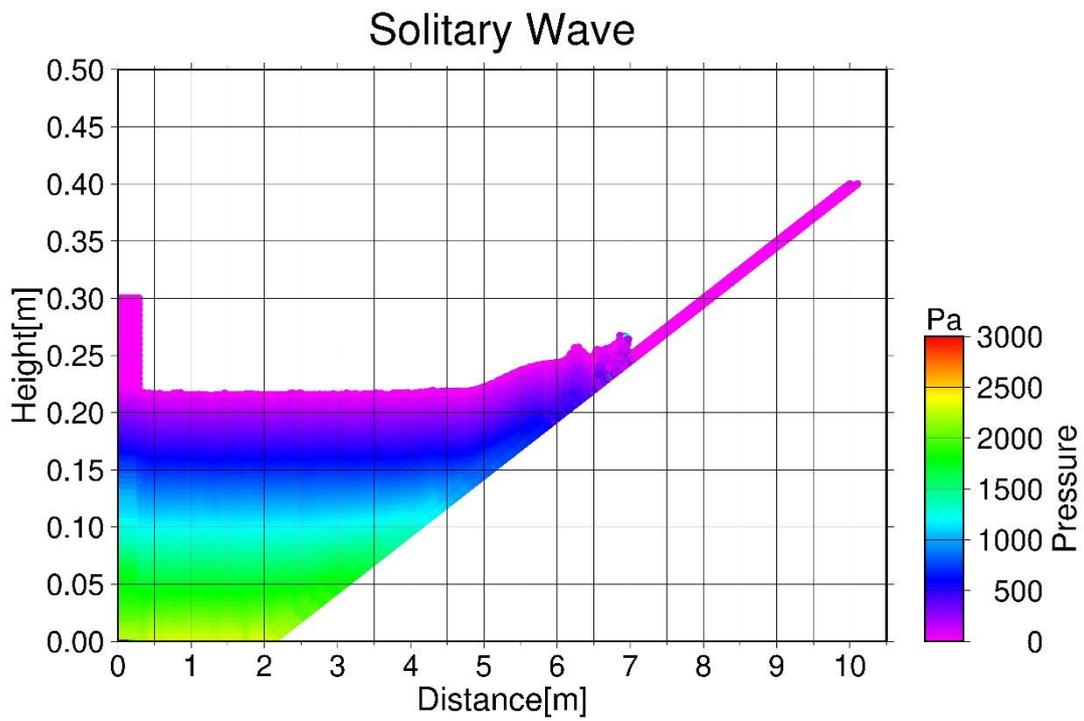
(d) $t = 5.50$ [s]
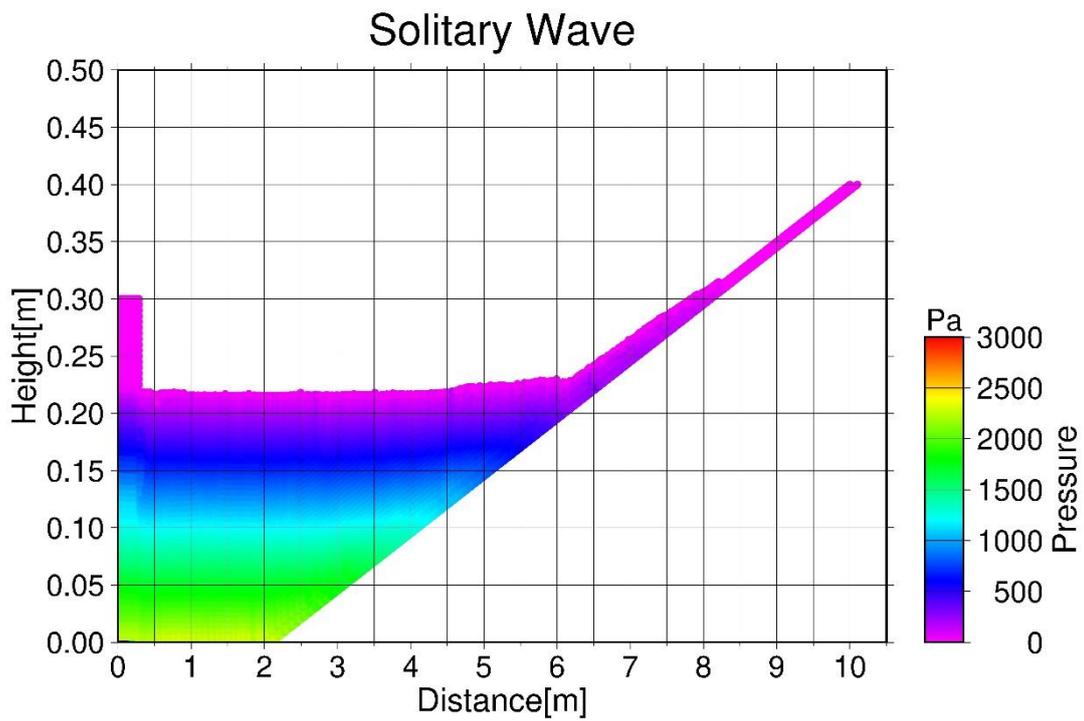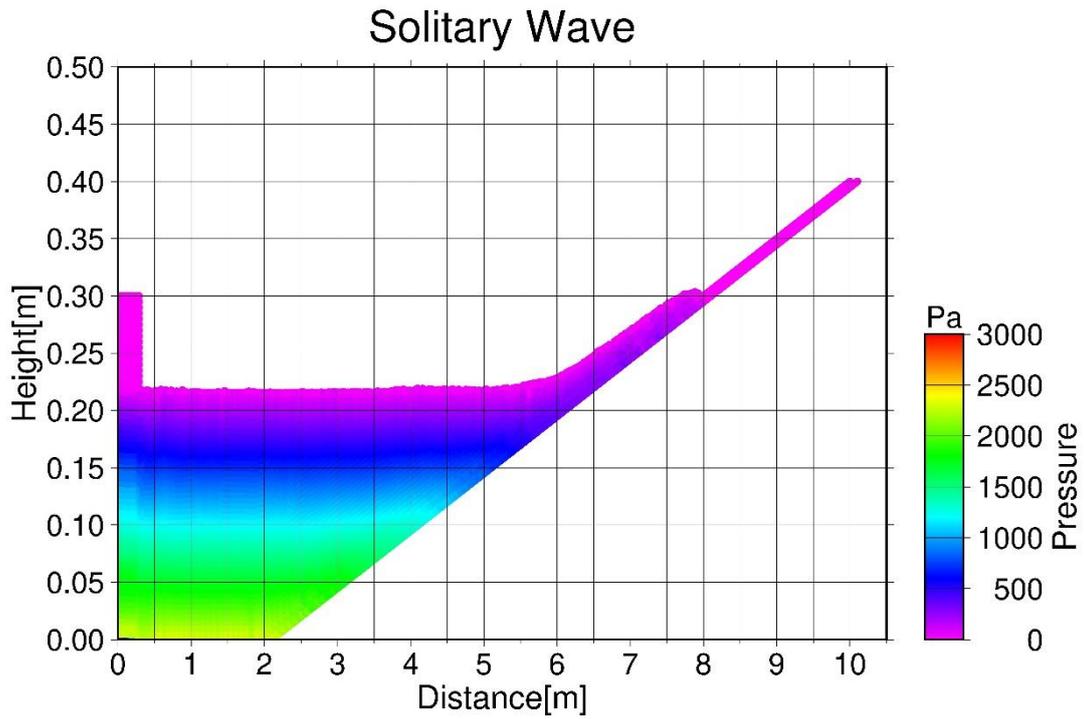
(e) $t = 7.00$ [s]

(f) $t = 8.25$ [s]

Figure 4.13 Pressure fields produced by the Wendland kernel and the standard source

term for a 1:20 scale slope

(a) $t = 1.50$ [s]

(b) $t = 2.50$ [s]

Solitary Wave

(c) $t = 4.00$ [s]

Solitary Wave

(d) $t = 5.50$ [s]

84
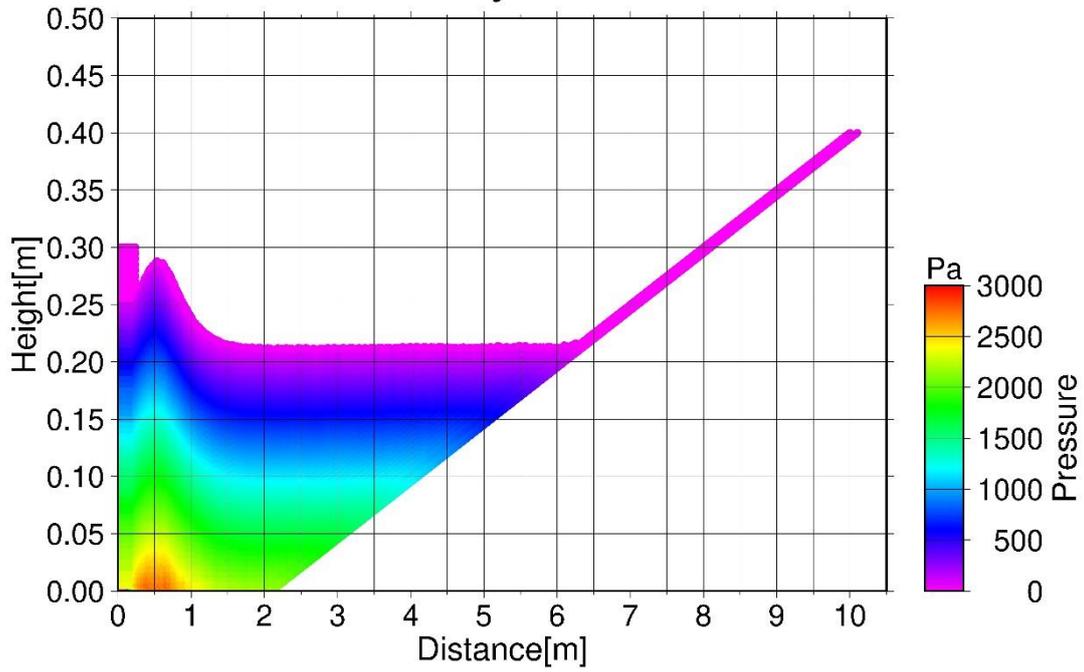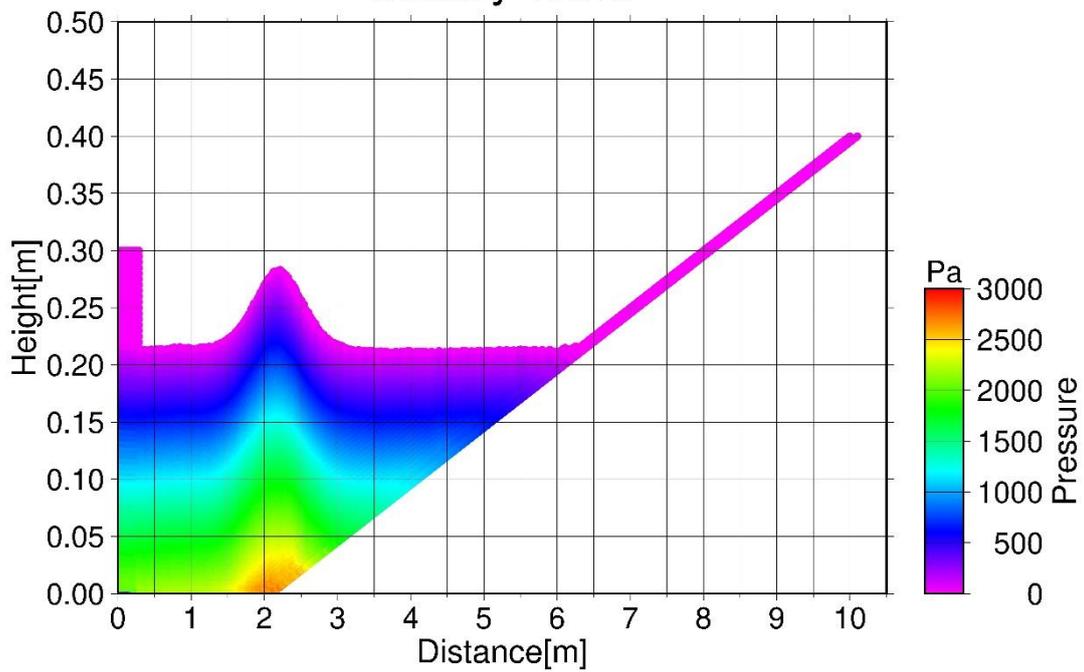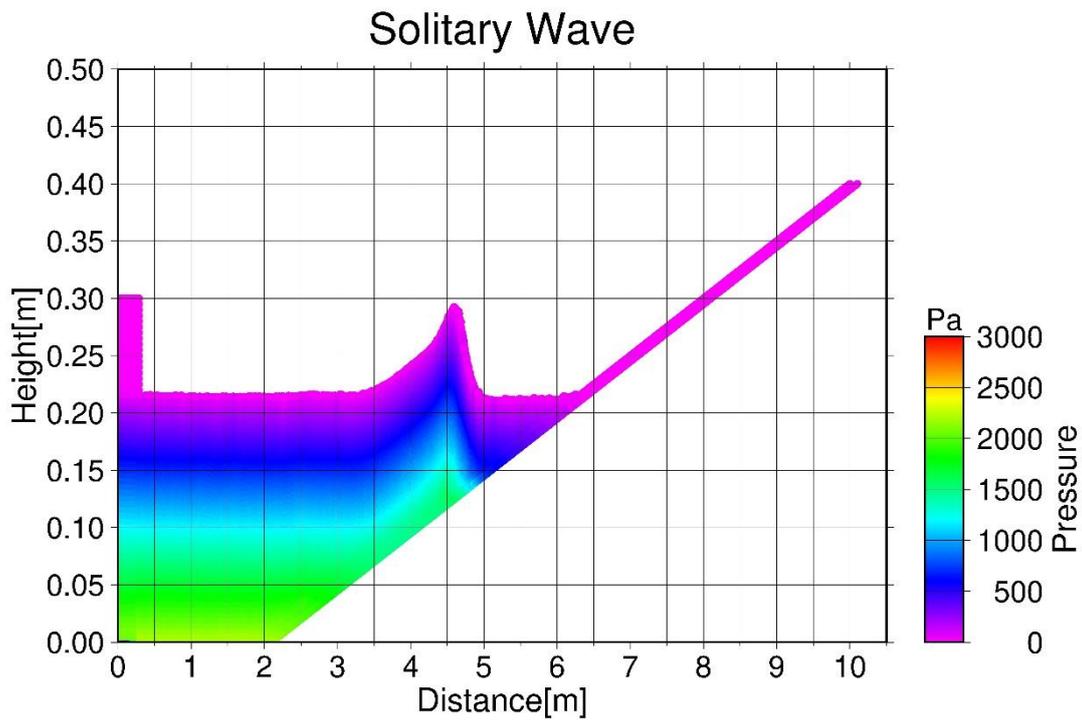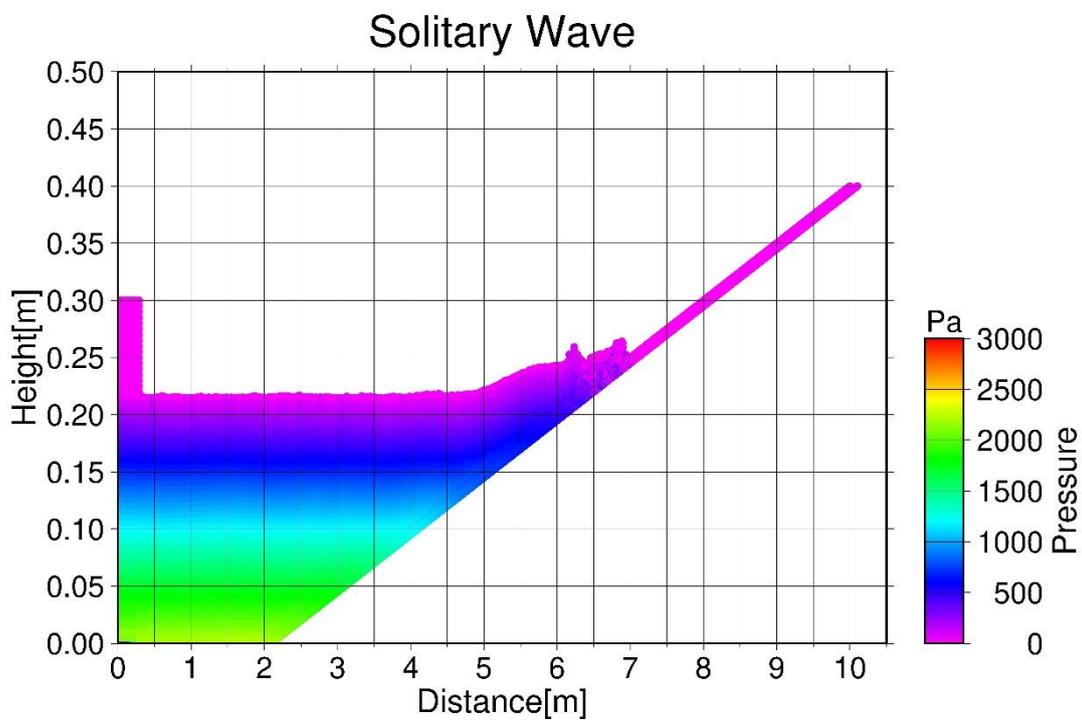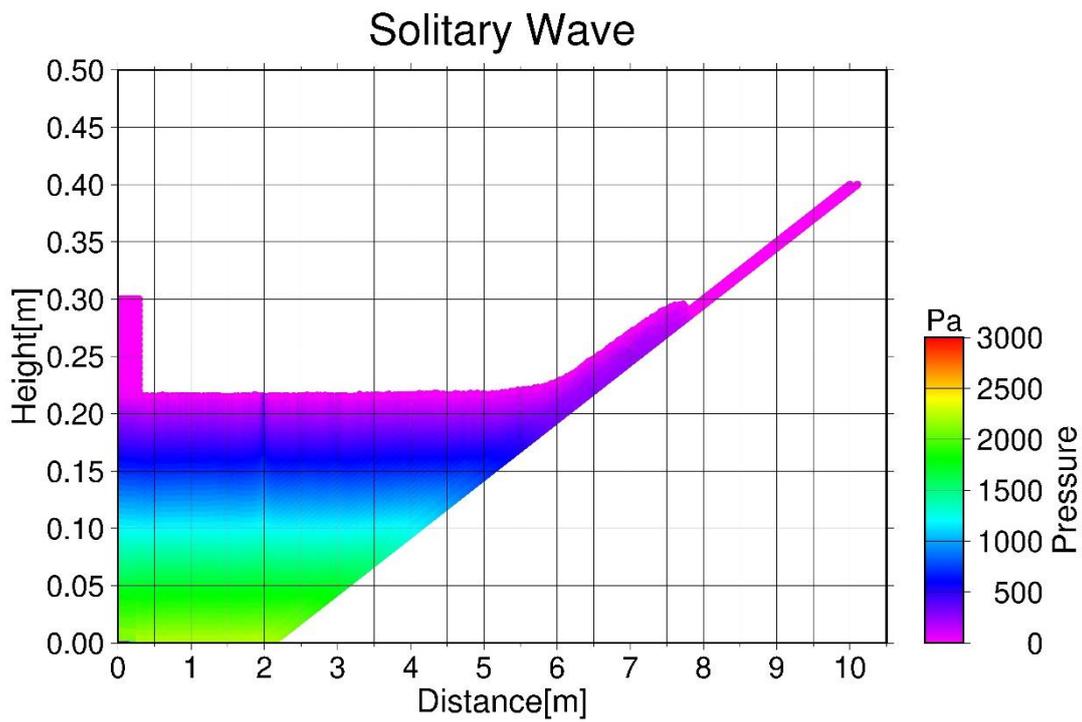
(e) $t = 7.00$ [s]
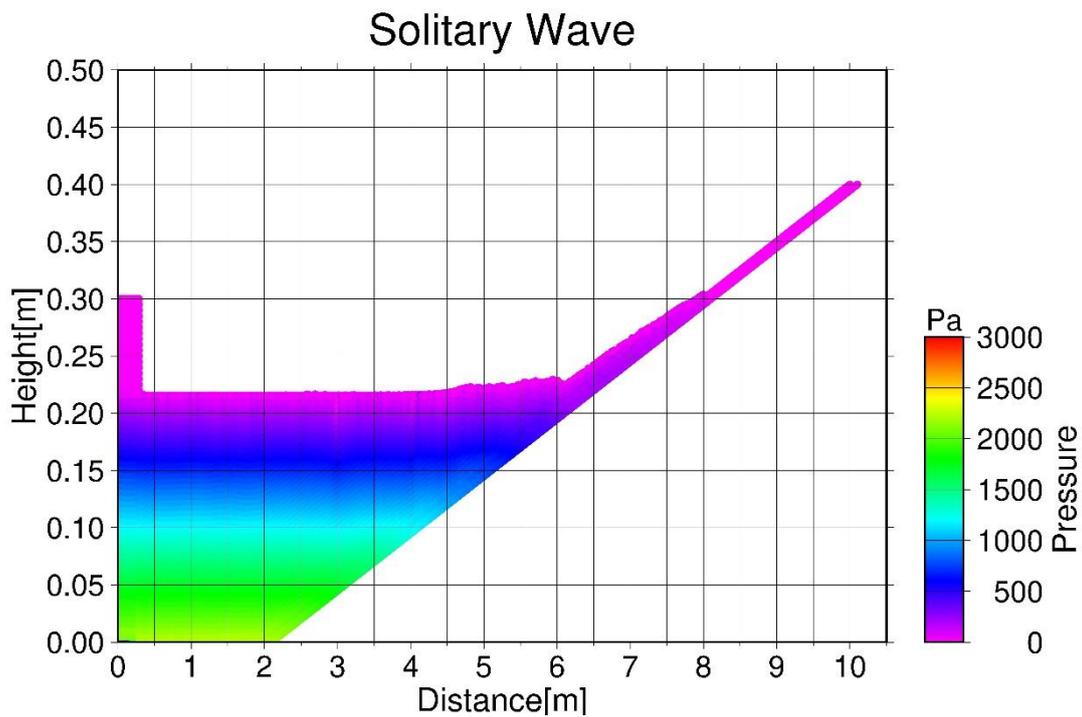
(f) $t = 8.25$ [s]

Figure 4.14 Pressure fields produced by the Wendland kernel and the hybrid source term

for a 1:20 scale slope

85

4.6.3　　　Choice of kernel and source term

The Wendland kernel gives more accurate integral approximation than the B-spline kernel regardless of the choice of the source term. This is more dominantly presented for breaking-waves; more violent free-surface flows. The HS source term works more effectively to smooth pressure fields for the B-spline kernel than for the Wendland kernel and more effectively for breaking waves than for non-breaking waves. In the following simulations, the Wendland kernel was used and the combination ratio γ was set to be 0.97.

4.7　　　Dam-breaking simulation

In order to validate the present ISPH model for porous flows, the numerical results obtained from the flow passing through a porous dam were compared with the experimental data obtained by Liu et al. (1999). The experiment is a dam-breaking flow through a porous block. The water tank used in the experiment was 89.2 cm long, 44 cm wide, and 58 cm high (Figure 4.15). A 29-cm-long porous dam was placed in the section between $x = 0.30 - 0.59$ [m], and it was 37 cm high. A gate was built 2 cm away from the left side of the porous dam to create a water reservoir with a water depth of 25 cm. The porous dam was confined in the initial region to ensure that the porous medium was not allowed to move. The porous dam is made of crushed rocks. The mean grain diameter is 1.59 cm and the porosity is 0.49. The parameters of computing are listed in Table 4.3.
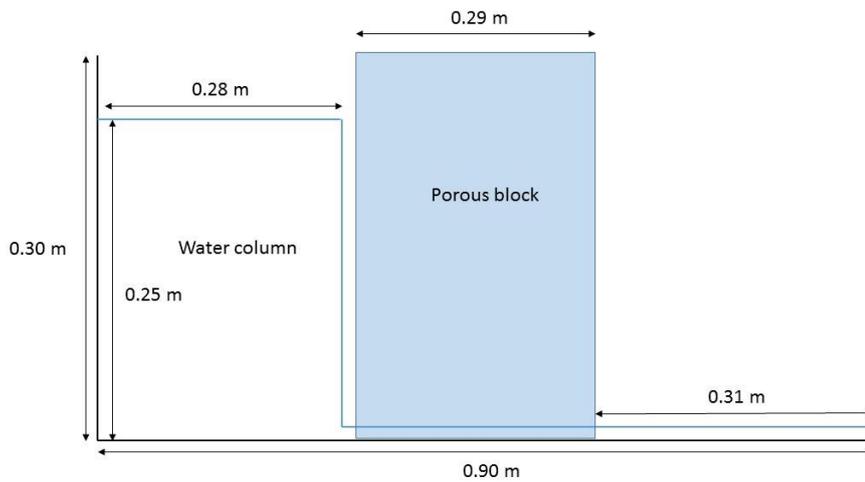
Figure 4.15 Schematic diagram of dam breaking with a porous block

Table 4.3 Computational parameters for dam breaking with a porous bock

Parameters	Value
Diameter of particles	0.005 m
Initial particle spacing	0.005 m
Smoothing length	0.0085 m
Initial time step	0.0005 sec
Smagorinsky coefficient	0.1
Courant number	0.2
Combination ratio of the source term	0.97

Figure 4.16 shows the comparison between the numerical results and experimental data for free surface profiles during the period when the flow passed through the porous dam. Note that the black dots are the experimental free surface. At $t = 0.00$ [s], the non-zero pressure was obtained only around the lower-left corner of the water column. It is natural that the pressure due to the gravitational force cannot be correctly loaded at the very

beginning of computing. After $t = 0.4$ [s], the PPE is successfully solved by the SOR method and the accurate pressure fields were obtained.

Immediately after the water column started to collapse, the front of the dam breaking flow rushed towards the right side and collided the porous block. Consequently, the top of the wavefront became higher than the collapsing water column (Figure 4.16 (b)). This phenomenon was reproduced by the present ISPH model. However, the height of the water column was slightly overestimated while the free surface at $x = 0.45 - 0.60$ [m] was underestimated. The solid lines describe the pressure at every 500 Pa. They show the continuous pressure field at the water-porous interface. These lines look to break at the right end of the porous block. This is because the water depth on the right is shallow and thus the pressure is low.

Figures 4.16 (c) to (f) describe the process of the dam breaking flow propagating through the porous block. During these phases, the computed free surface was in strong agreement with the experimental data. Fewer fluid particles were contained inside the porous block compared with the number of particles outside the block. This is evidence that the apparent density successfully works to sustain the solid skeleton of porous media. The pressure field was accurately calculated and smoothed. In the water-porous interface around $x = 0.3$ [m] and $x = 0.6$ [m], the pressure fields looked continuous. The new free surface condition prevented fluid particles from being zero-pressure inside porous media.

It should be noted that although the apparent density concept has already been proposed by Akbari (2014), Ren et al. (2016) and others, those studies did not show the pressure

fields of their simulation results, presenting only the free-surface comparisons with the experiments. It is doubtful whether past researchers could obtain satisfactory pressure fields with their SPH scheme. The overall results of the present ISPH model show good agreement with the experiment of Liu et al. (1999). It can be concluded that the present ISPH model is capable of simulating violent flows through porous media and of yielding accurate pressure fields.
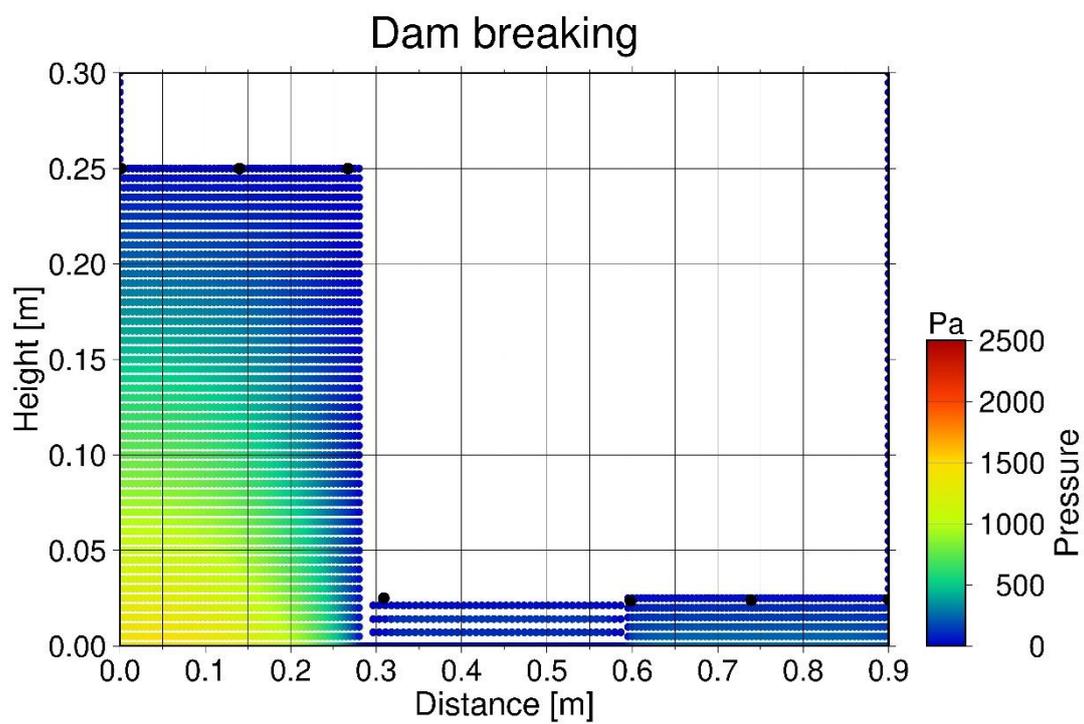
(a) $t = 0.00$ [s]

Dam breaking
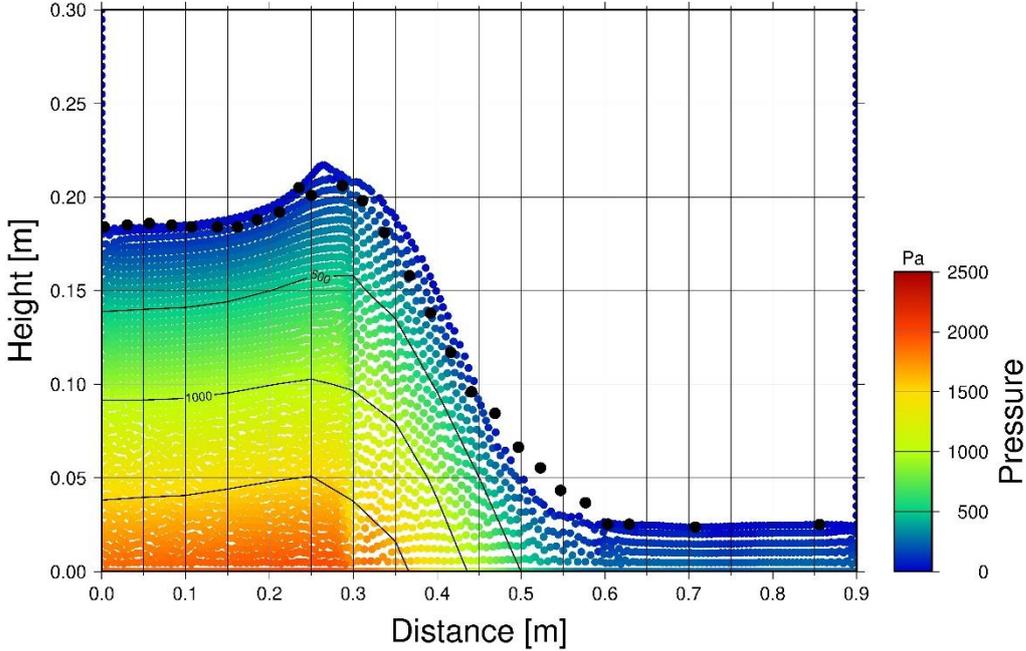
(b) $t = 0.400$ [s]

Dam breaking
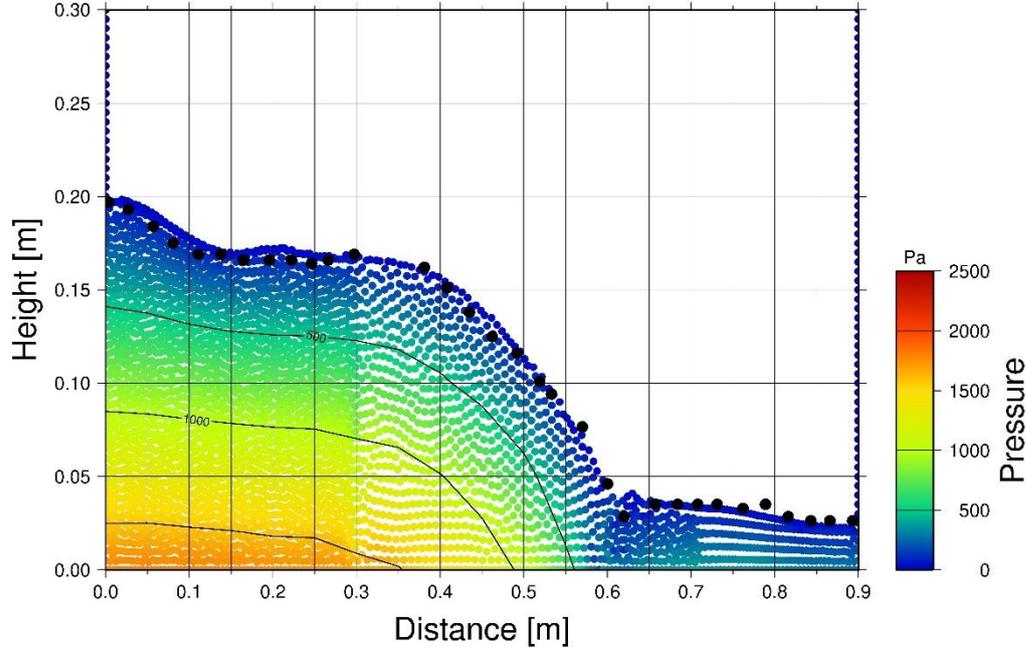
(c) $t = 0.800$ [s]

Dam breaking
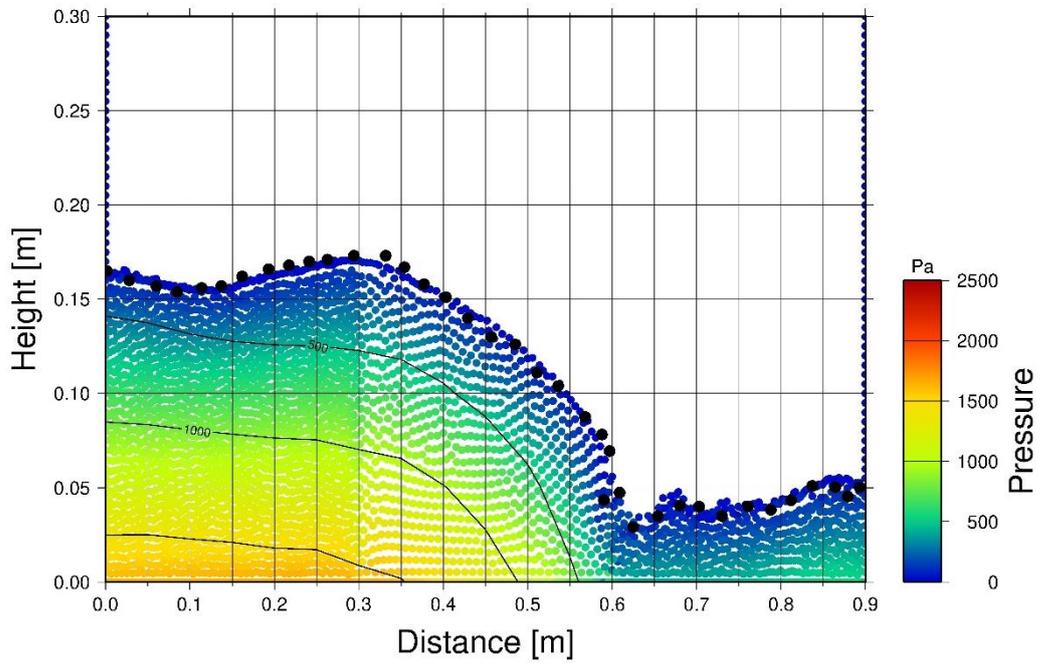
(d) $t = 1.20$ [s]

Dam breaking
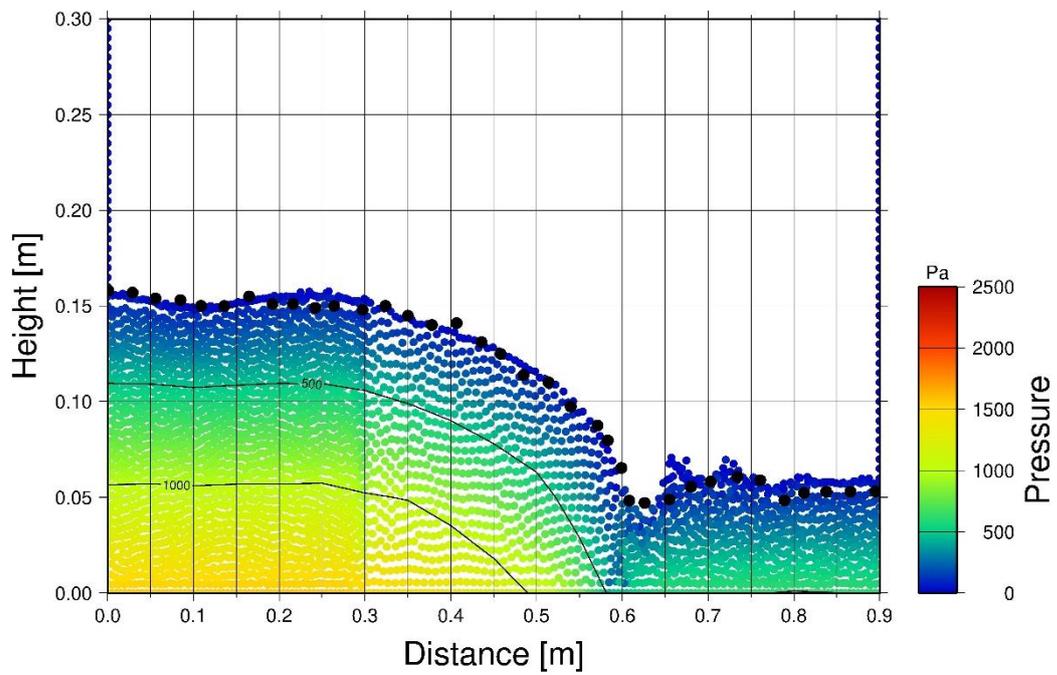
(e) $t = 1.60$ [s]
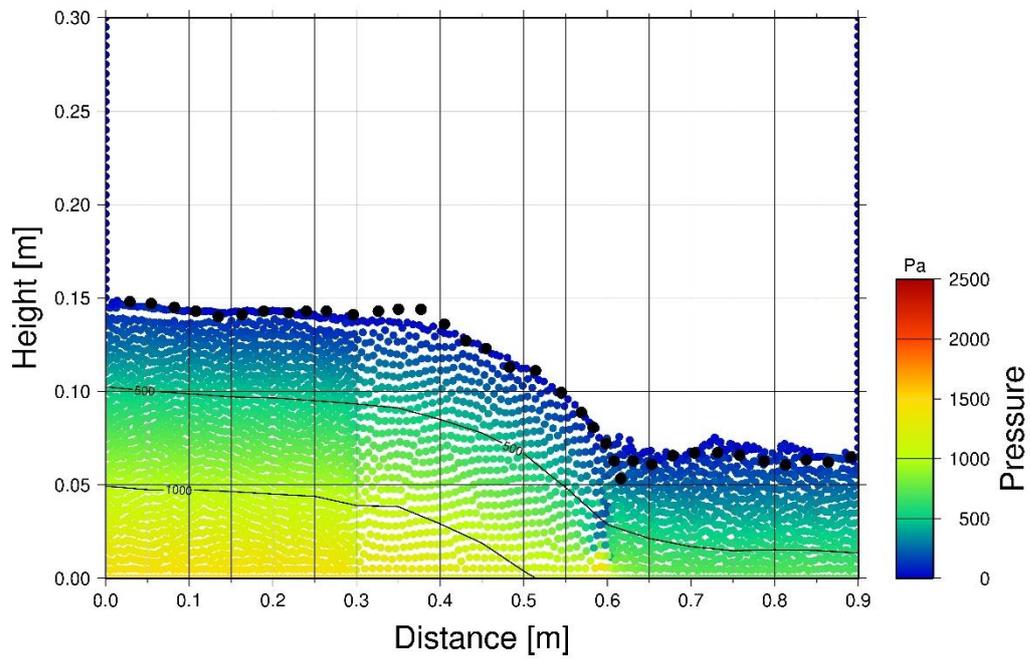
(f) $t = 2.00$ [s]

Figure 4.16 Comparison of the dam breaking simulation results with the experimental

free surface data

Chapter 5   Wave runup on a steep slope

5.1   Overview

Wave runup is an essential factor for some coastal structures such as revetments, breakwaters and seawalls. These structures are often constructed to mitigate wave attacks, particularly tsunamis. Traditionally, tsunami waves have been modelled as solitary waves due to their hydraulic similarities (Lin et al., 1999, Borthwick et al., 2006, Chang et al., 2009). The accurate estimation of the maximum runup height will help engineers to design more effective and economical coastal protections.

Due to its capability for violent free-surface simulations, SPH has been applied to solitary wave runup problems. Monaghan and Kos (1999), for instance, assumed the Cretan beach in SPH-based wave flume and estimated runup heights. Meanwhile, Kim and Ko (2008) and Rasoul and Kourosh (2012) investigated solitary wave runup on a relatively steep slope with ISPH. Most studies, however, assume a smooth impermeable slope to be a beach. Actual beaches, in reality, generally consist of soil, small rocks, gravel, and sand. For the accurate estimation of solitary wave runup in numerical simulations, soil beaches need to be set up instead of solid ones. In this chapter, the present ISPH model is applied to the simulations of solitary wave runup on a relatively steep slope. Firstly, wave runup on a solid slope is briefly reviewed. Secondly, permeable slope cases are investigated and the relationship between runup height and porous media is discussed.

5.2   Prediction of runup height

Many studies have tried to find a consistent law to predict wave runup height on a solid slope. Carrier and Greenspan (1953) obtained solutions of the non-linear shallow-water

equations to investigate the behaviour of wave propagating over a slope. They presented some waves that can clime a slope without breaking. Synolakis (1986) investigated solitary wave runup height extensively through experiments and analytical work in his PhD thesis and summarised all findings in Synolakis (1987). He proposed the following law for nonbreaking waves:

$$\frac{R}{h_0} = 2.831(cot\varphi)^{\frac{1}{2}}\left(\frac{H}{h_0}\right)^{\frac{5}{4}} \tag{5.2.1}$$

In Equation (5.2.1), R is the maximum wave runup height and, φ is a slope angle. He also presented the transition wave height between nonbreaking and breaking waves as follows:

$$\frac{H}{h_0} = 0.8183(cot\varphi)^{-\frac{10}{9}} \tag{5.2.2}$$

Li and Raichlen (2001) modified Synolakis's (1986) runup height law for nonbreaking waves as follows:

$$\frac{R}{h_0} = 2.831(cot\varphi)^{\frac{1}{2}}\left(\frac{H}{h_0}\right)^{\frac{5}{4}} + 0.293(cot\varphi)^{\frac{3}{2}}\left(\frac{H}{h_0}\right)^{\frac{9}{4}} \tag{5.2.3}$$

Equation (5.2.3) provides more accurate estimation of runup height and strong agreements with experimental data in both relatively steep (1:2.08) slope and mild (1:20) slope.

Hughes (2004) focused on the nondimensional wave momentum flux M_F using the first-order solitary wave theory, where

$$\begin{aligned}\left(\frac{M_F}{\rho g h_0^2}\right)_{max} = &\frac{1}{2}\left[\left(\frac{H}{h_0}\right)^2 + 2\left(\frac{H}{h_0}\right)\right] \\ &+ \frac{N^2}{2M}\left(\frac{H}{h_0} + 1\right)\left\{tan\left[\frac{M}{2}\left(\frac{H}{h_0} + 1\right)\right]\right. \\ &\left. + \frac{1}{3}tan^3\left[\frac{M}{2}\left(\frac{H}{h_0} + 1\right)\right]\right\}\end{aligned} \tag{5.2.4}$$

The coefficients M and N in Equation (5.2.4) can be approximated empirically by the following functions:

$$M = 0.98 \left\{ tanh \left[2.24 \left(\frac{H}{h_0} \right) \right] \right\}^{0.44}$$
$$N = 0.69 tanh \left[2.38 \left(\frac{H}{h_0} \right) \right]$$

(5.2.5)

Hughes (2004) derived the following runup law for nonbreaking solitary waves from the momentum flux:

$$\frac{R}{h_0} = 1.82(cot\varphi)^{\frac{1}{5}} \left(\frac{M_F}{\rho g h_0^2} \right)$$

(5.2.6)

5.3   Wave runup on a solid slope

5.3.1   Numerical setup

The same numerical flume is used in Section 4.6.1. The slope is located at $x = 2.07$ [m] and the slope scale is 1:2.08. All of the flume walls are smooth and impermeable. The mean water depth h_0 is 0.21m. A solitary wave was generated by a piston-type wavemaker at the left end with the relative wave height H/h_0=0.100, 0.163, 0.200, 0.250, and 0.300. From Equation (5.2.2), the transition relative wave height is more than 1.8, which means that the generated wave is expected to be a nonbreaking wave during the running up process. The essential parameters are listed in Table 5.1.

Table 5.1 Computational parameters for wave runup on a 1:2.08 solid slope

Parameters	Value
Diameter of particles	0.005 m
Initial particle spacing	0.005 m
Smoothing length	0.006 m
Initial time step	0.00025 sec
Courant number	0.2
Smagorinsky constant	0.1
Combination ratio of the source term	0.97

5.3.2   Results

Figure 5.1 shows the computed particle distribution of the experimental wave profile of H/h_0=0.163. The blue dots represent Li and Raichlen's (2001) experiment data. Both x and y axis are normalised by the initial depth h_0. The mean water level is set to be zero and $x/h_0 = 0$ refers to the location of the original shoreline. Time t^* is a nondimensional time in which t is divided by $\sqrt{\dfrac{h_0}{g}}$.

At the initial phase of the runup process, the present ISPH agreed well with the experiment (see Figure 5.1 (a)). As the runup proceeds until $t^* = 10.2$, there was nearly no difference of the wave profile between the ISPH result and the experiment data. When the wave began to run down in Figure 5.1 (c), the front of the simulated flow looks thinner than the experiment flow. Nevertheless, the wave profile in the ISPH simulation agreed well with the experiment data. At the end of the rundown process in Figure 5.1 (d), the curve of the computed wave profile was looser, and the height at the wavefront was larger than in the experiment. In the simulation, the slope is assumed to be absolutely smooth; no friction force is considered between the slope and fluid particles. Moreover, movable particles model only fluids and air is not considered in the simulation. These assumptions can lead to differences in the results of the rundown process. Nonetheless, the overall simulated wave profiles reasonably agree with the experiment data.

(a) $t^* = 8.2$

(b) $t^* = 10.2$

(c) $t^* = 12.2$
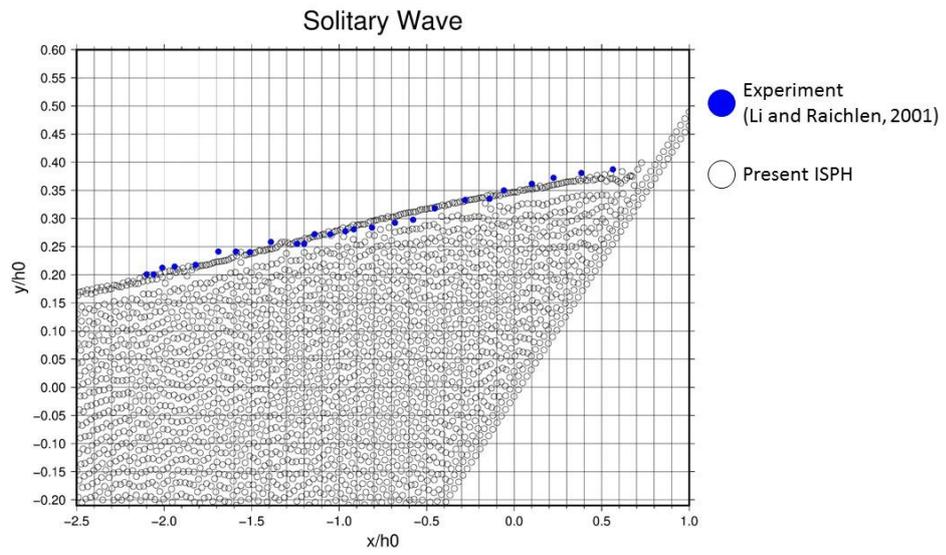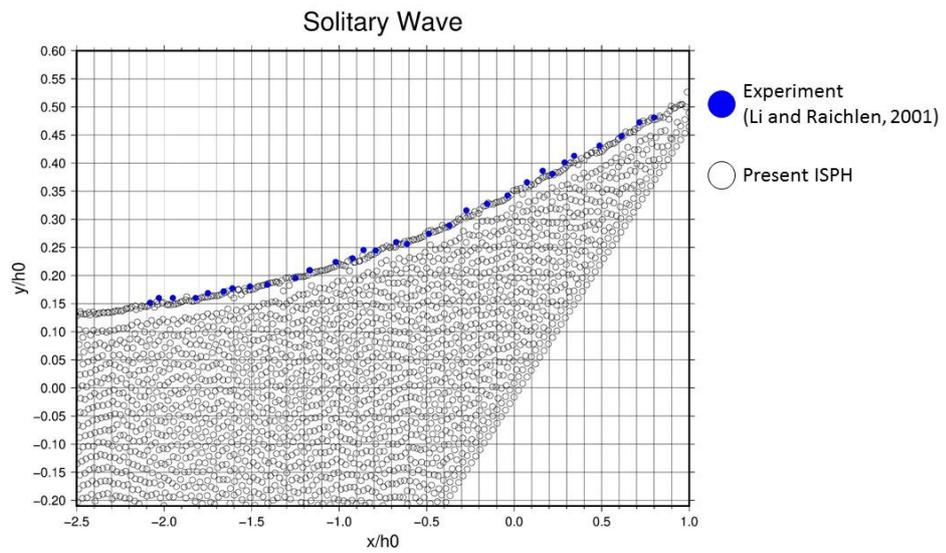
(d) $t^* = 14.2$
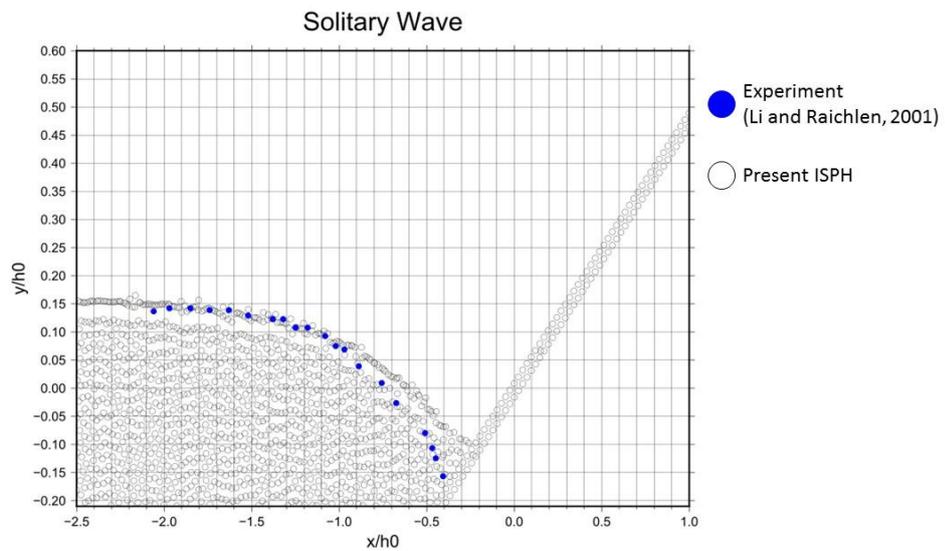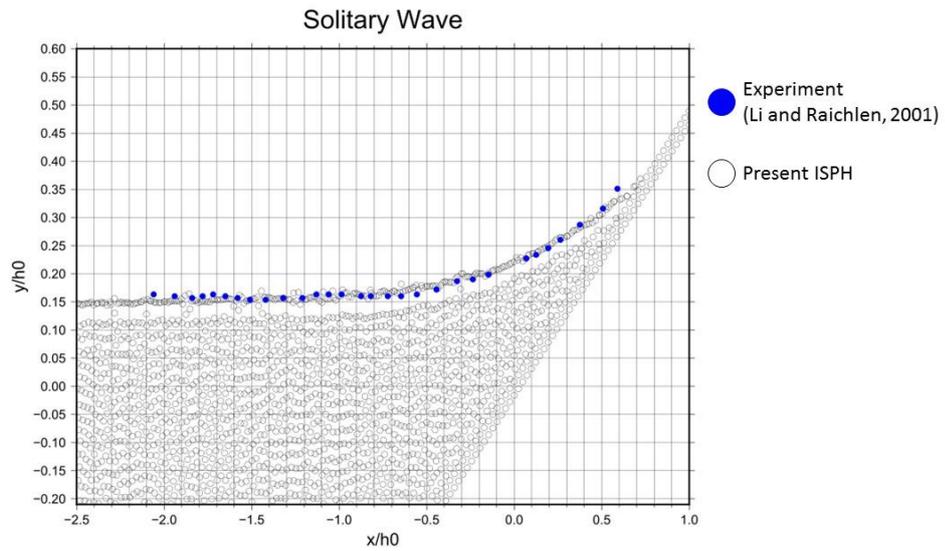
Figure 5.1 Particle distribution of wave runup and rundown on a 1:2.08 solid slope

Figure 5.2 compares the runup height with the present ISPH simulation results, the experiment data, and the theoretical solutions. Notably, only the nonbreaking wave runup laws are presented since the generated wave never broke during the simulation.
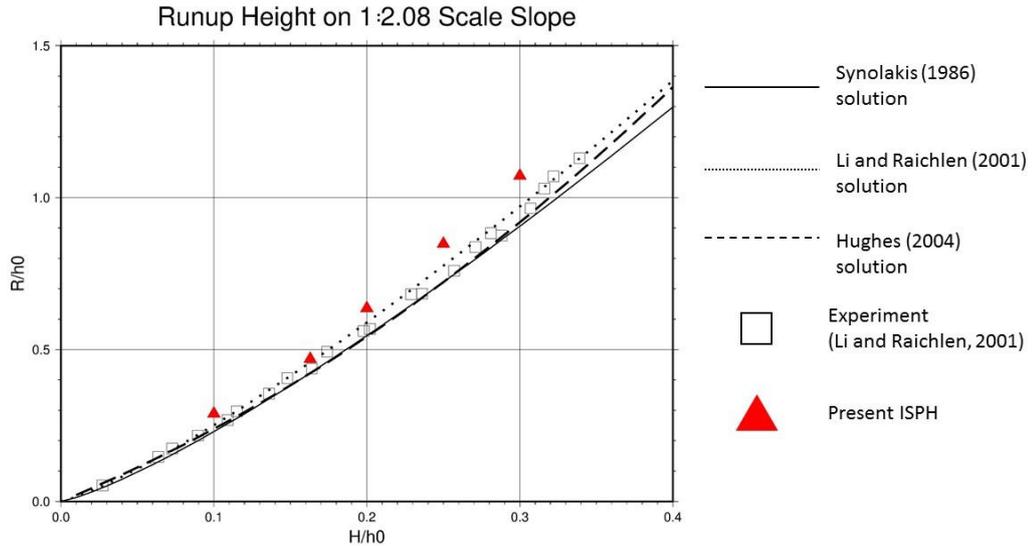
Figure 5.2 Runup height on a 1:2.08 solid slope

The computed relative runup height R/h_0 was 0.469 with the wave $H/h_0 = 0.163$ and 0.848 with the wave $H/h_0 = 0.25$. The three runup height theories show the different solutions as H/h_0 becomes larger. The Li and Raichlen's (2001) law provides the most accurate estimation against the experimental results, whereas the Synolakis (1986) and Hughes (2004) laws underestimate a runup height. The results of the present ISPH show a good agreement with the three theories and the experimental results when $H/h_0 = 0.10$ and 0.163. The present model tends to slightly overestimate a runup height, as the initial wave height becomes larger. However, it can be concluded that the results of the present ISPH model reasonably satisfy the Li and Raichlen's (2001) solution and the experiment.

5.3.3   Discussion

In Section 4.6.3, the choice of the kernel function and the source terms were determined according to pressure fields. The Wendland kernel generated more accurate pressure than the B-spline kernel, and the hybrid source term yielded more smooth pressure field than the standard source term. The combination of the Wendland kernel and the hybrid source

term worked successfully for the dam breaking simulation with a porous block in Section 4.6.4. In this section, the choice of the source term is investigated in terms of wave runup. The numerical settings are the same in Section 4.6.4, except for the combination ratio γ of the source term, which is set to be zero so that only the standard source term is used.

Figure 5.3 compares the simulated particle distribution with the experiment wave profile. At the initial stage of the runup process in Figure 5.3. (a), the computed wave profile was almost the same as the experiment and the result with the hybrid source term. However, at $t^* = 10.2$ during running up, the wave elevation was slightly lower at the front while it was larger around $x/h_0 = -2.0$ to -1.0. The difference became more significant and could not be neglected during the rundown process. A few particles seemed to stick to the slope at $t^* = 14.2$

(a) $t^* = 8.2$

(b) $t^* = 10.2$
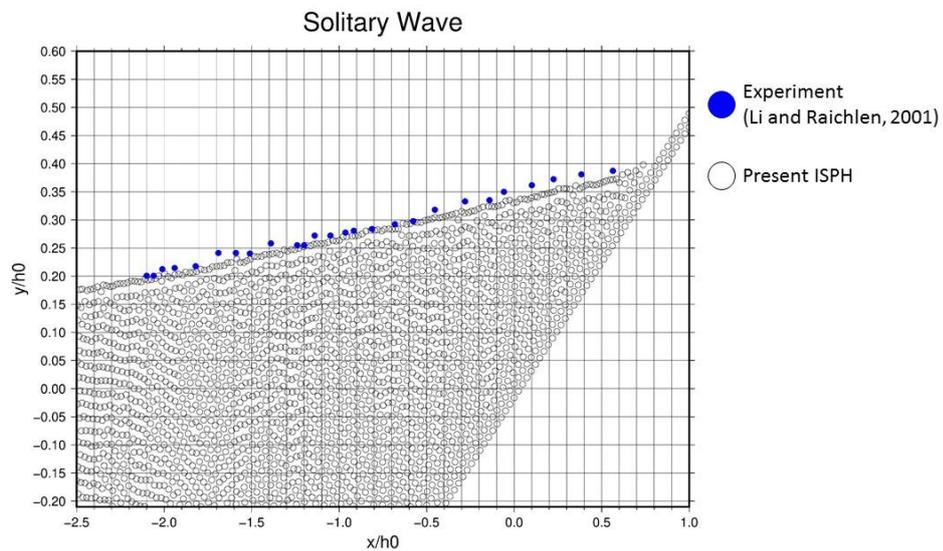
(c) $t^* = 12.2$
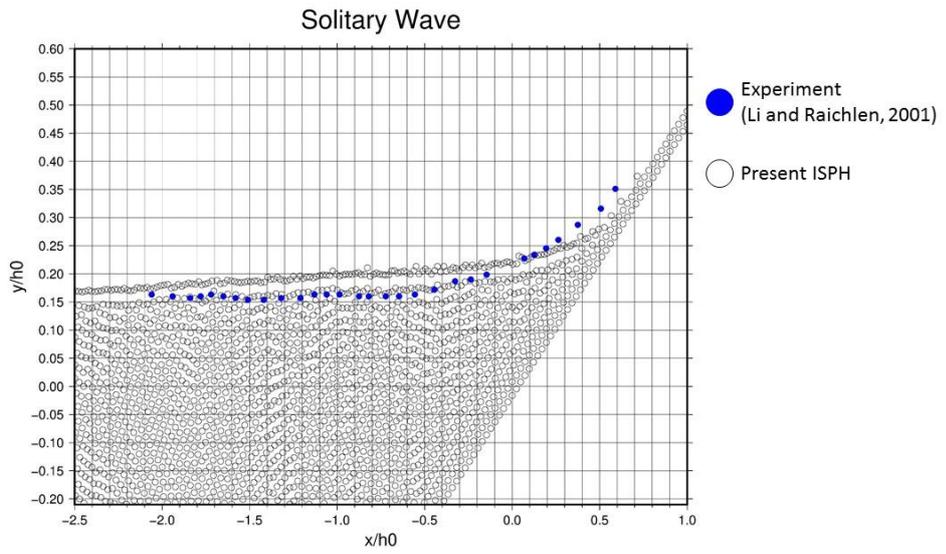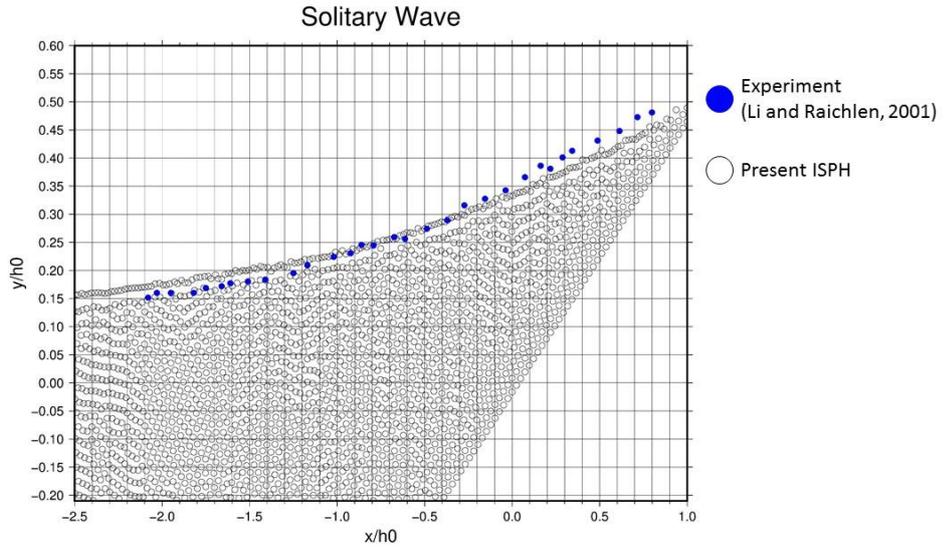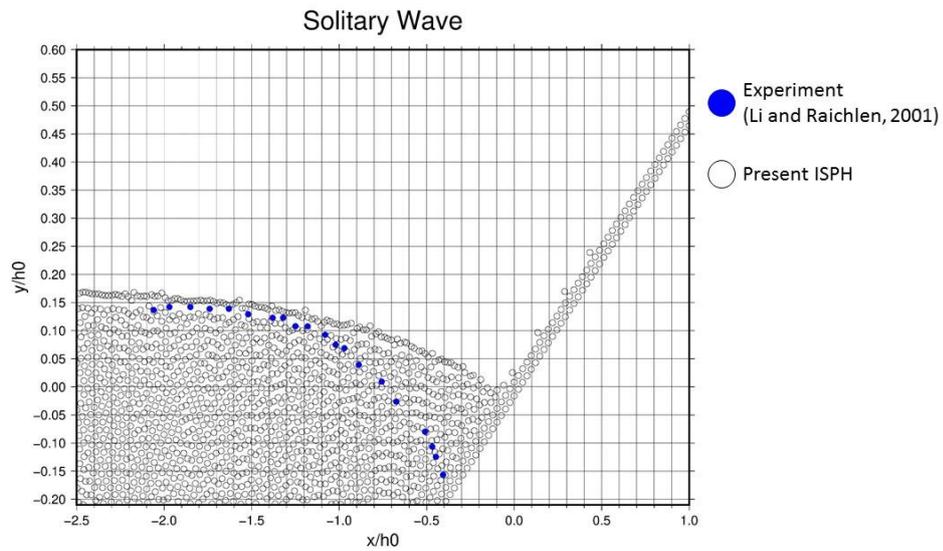
(d) $t^* = 14.2$

Figure 5.3 Particle distribution of wave runup and rundown on a 1:2.08 solid slope

obtained by the standard source term

Figure 5.4 compares the deviation of the vertical wave profile produced by the hybrid

source term and the standard source term. Li and Raichlen's (2001) experimental data is

regarded as the average, and the standard deviation is calculated. The horizontal axis

represents the normalised time t^*, which is the same time scale as shown in Figures 5.2

and 5.3. In Figure 5.4, the deviation became significantly larger during the runup process

in the standard source term case than that in the hybrid source term, which means that the

hybrid source term yields more accurate results than the standard source term.
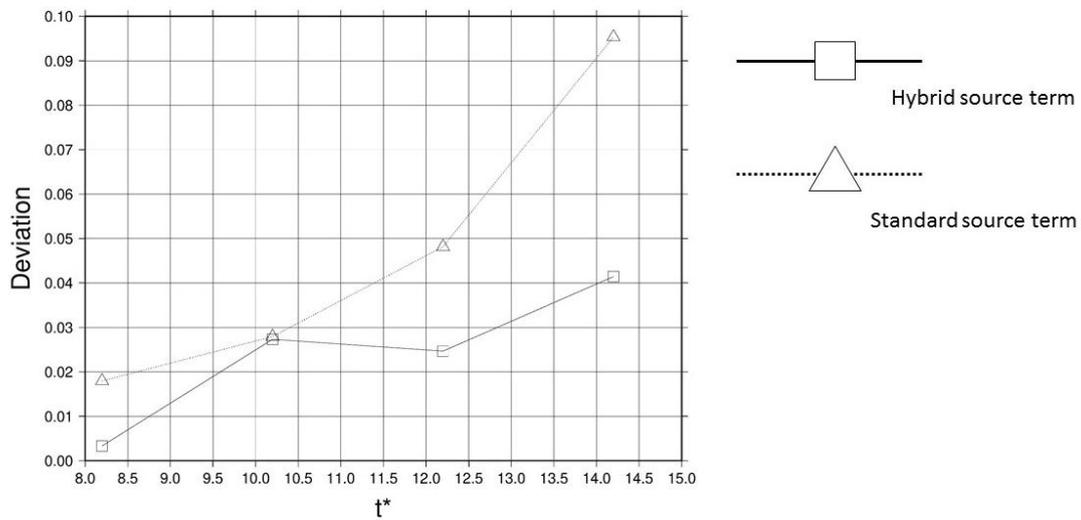
Figure 5.4 Standard Deviation of surface profile on a 1/2.08 slope

Figure 5.5 compares the runup height with the theories, the experiment, and the ISPH simulation results. The results produced by the standard source term only agree better with the theories than the results of the hybrid source term if H/h_0 is 0.10 and 0.163. When the generated wave height is larger than $H/h_0 = 0.20$, the results of runup height become inconsistent. At $H/h_0 = 0.25$, the obtained runup height is lower than the theoretical solutions. In contrast, the runup height at $H/h_0 = 0.20$ and 0.30 is larger than the theoretical values and nearly the same as the results obtained by the hybrid source term. In conclusion, the verification of the results is limited to the small relative wave height cases when only the standard source term is used. Consistent results of runup height for nonbreaking waves can be obtained through the hybrid source term.
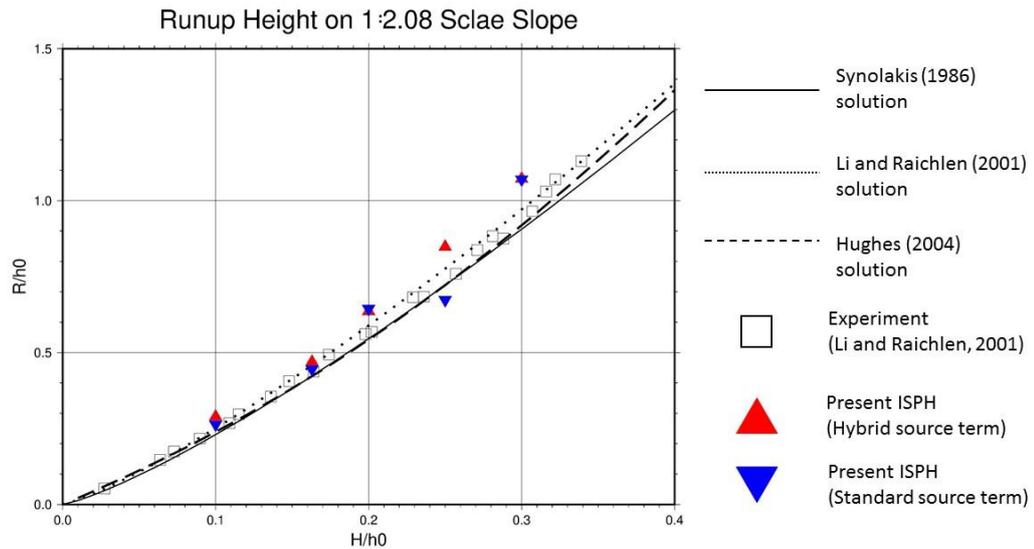
Figure 5.5 Runup height on a 1:2.08 solid slope obtained by the standard source term

5.4 Wave runup on permeable beach
5.4.1 Numerical setup

In this section, the wave runup on a permeable beach is investigated. The wave flume is 3.0 m long. A triangle-shaped porous media is located at $x = 2.07 - 3.00$. The slope scale is 1:2.08 ($\varphi \approx 25.68°$). The schematic diagram of which is shown in Figure 5.6. Whereas the porosity of the porous media was fixed at 0.49, the mean grain diameter varied from 0.20 mm to 200.0 mm. The computational parameters are listed in Table 5.2. The mean water depth was 0.21 m and the two different wave heights were tested: 0.03423 m ($H/h_0 = 0.163$) and 0.0525 m ($H/h_0 = 0.25$). In these simulations, the runup height is defined as the highest point of the wave at the water-porous boundary.
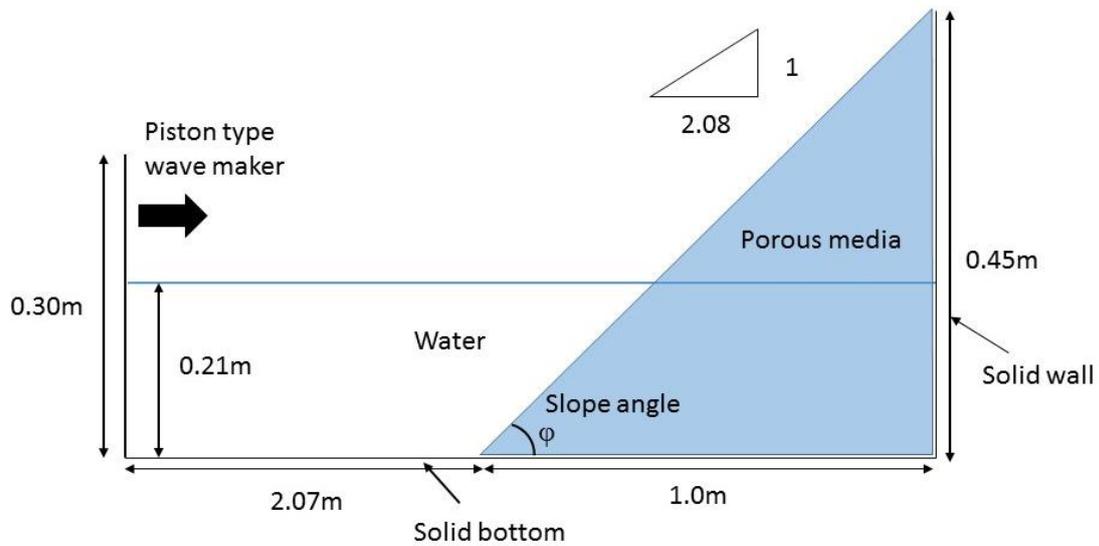
Figure 5.6 Setting of a 1:2.08 permeable beach flume

Table 5.2 Computational parameters for wave runup on a 1:2.08 porous beach

Parameters	Value
Diameter of particles	0.005 m
Initial particle spacing	0.005 m
Smoothing length	0.0085 m
Initial time step	0.00025 sec
Courant number	0.2
Smagorinsky constant	0.1
Combination ratio of the source term	0.97
Mean grain diameter of porous media	0.20 mm, 0.25 mm, 0.50 mm, 1.0 mm, 2.0 mm, 10.0 mm, 20.0 mm, 50.0 mm, 100.0 mm, 200.0 mm

5.4.2 Results and analysis

Figures 5.7 and 5.8 describe the snapshots of solitary wave runup on a permeable beach, with the mean grain size Dc = 1.0 [mm] and 0.25 [mm], respectively. The initial wave height is 0.03423 m (H/h_0 = 0.163).

105

(a) $t = 3.50$ [s]

(b) $t = 4.05$ [s]
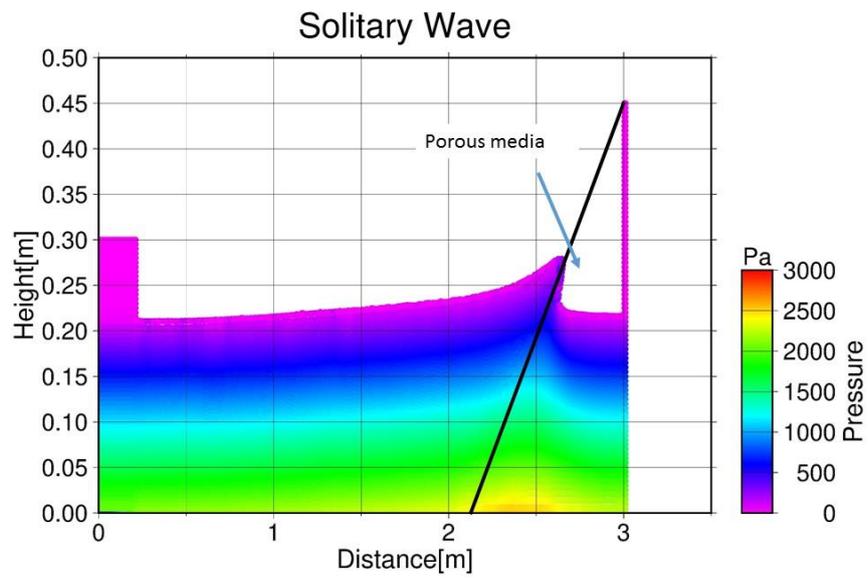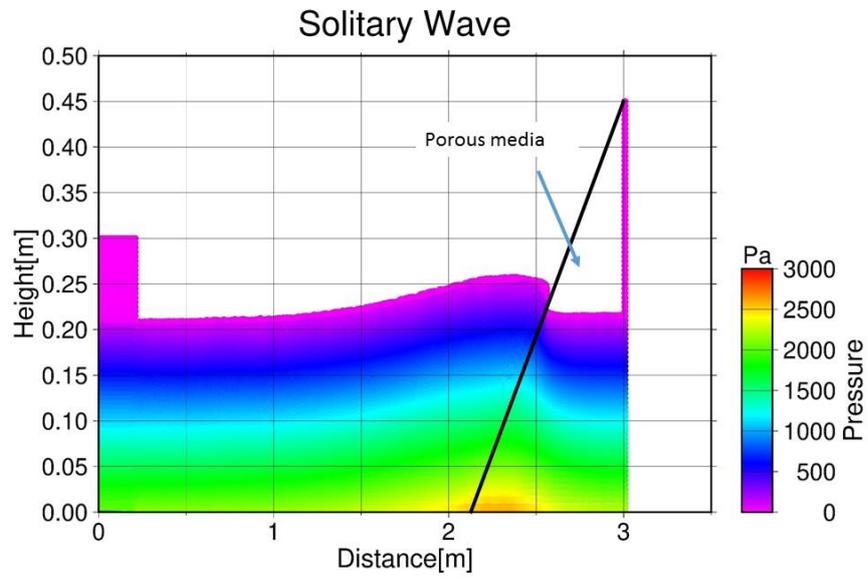
Figure 5.7 Wave runup on a 1:2.08 permeable beach with Dc = 1.0 [mm]
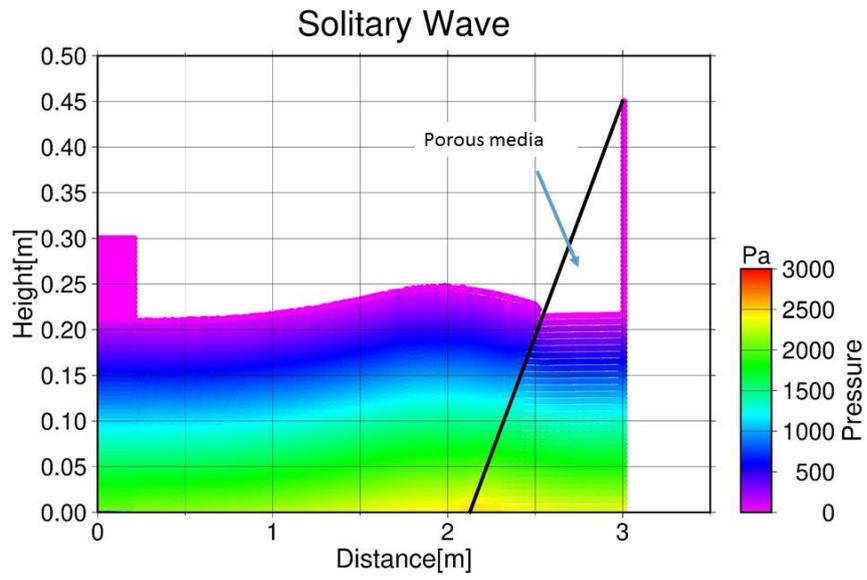
(a) $t = 3.25$ [s]
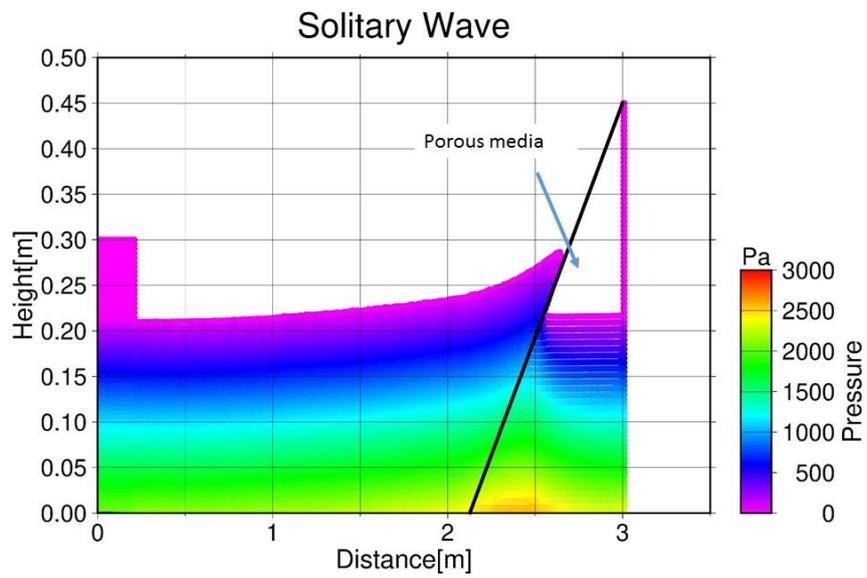
(b) $t = 3.95$ [s]

Figure 5.8 Wave runup on a 1:2.08 permeable beach with Dc = 0.25 [mm]

When the mean grain size is 1.0 mm, the wavefront reached the permeable slope at $t =$ 3.50 [s]. The wave was partly blocked by the permeable beach and distorted due to friction force. At $t = 4.05$ [s], the flow reached the highest point on the permeable slope. Some fluid particles could be observed in the porous media connecting the mean water level and the wave crest. These fluid particles propagated through the permeable beach from the pure fluid region. In Figure 5.8, the wavefront appeared to be chopped and discontinuous around the water-porous boundary due to large friction force. During running up, the water level kept the initial level at 0.21 m. Fluid particles slid on the permeable beach, and no particles newly penetrated the water-porous boundary. In both Figure 5.7 and Figure 5.8, the smooth and continuous pressure field is obtained through the Wendland kernel and the hybrid source term.

Meanwhile, Figure 5.9 compares the runup height of the two different wave heights with various mean grain sizes. Notably, the horizontal axis is logarithmic. The runup height decreases nearly linearly as the mean grain size of porous media becomes logarithmically larger. The computed height will converge to a certain value, but it is unlikely to reach the runup height on a solid slope even if the grain size is absolutely small.
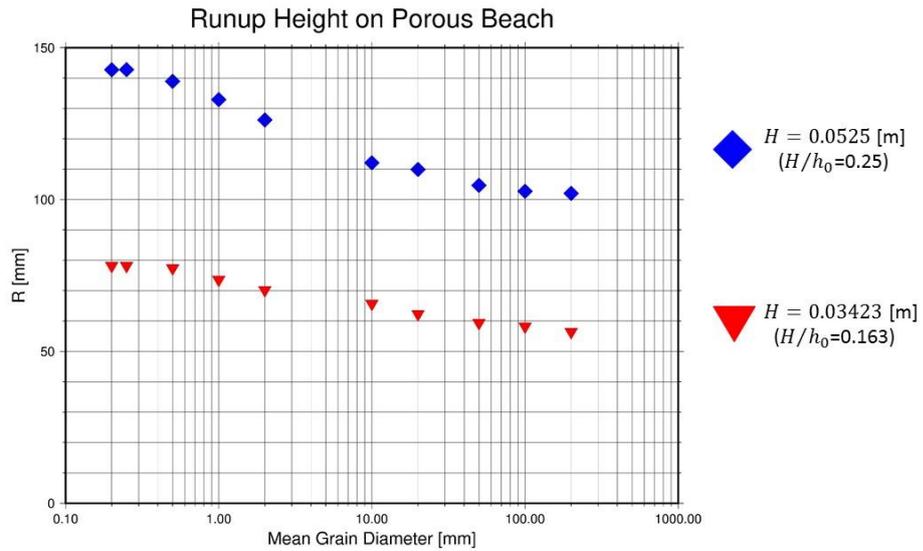
Figure 5.9 Runup hight on a 1:2.08 permeable beach

Figure 5.10 plots the velocity fields of the wave H = 0.03423 [m] (H/h_0 = 0.163) with the mean grain diameter of 0.25 mm. Note that the velocity fields were averaged at the grid size of 0.025 m and the position of the particles are described by the dots. The fluid particles inside the porous media had zero or nearly zero velocity, which means that these particles could not move and the permeable beach worked as if it had been a solid slope. In Figure 5.10 (b), few particles penetrated the beach from the pure fluid region. If the grain size is quite small, porous media can be regarded as an impermeable material. The difference between fine porous media and truly solid structure is that there are friction forces at a water-structure boundary. These friction forces contributed to lower runup height compared to wave runup on solid slope cases.

Velocity Field
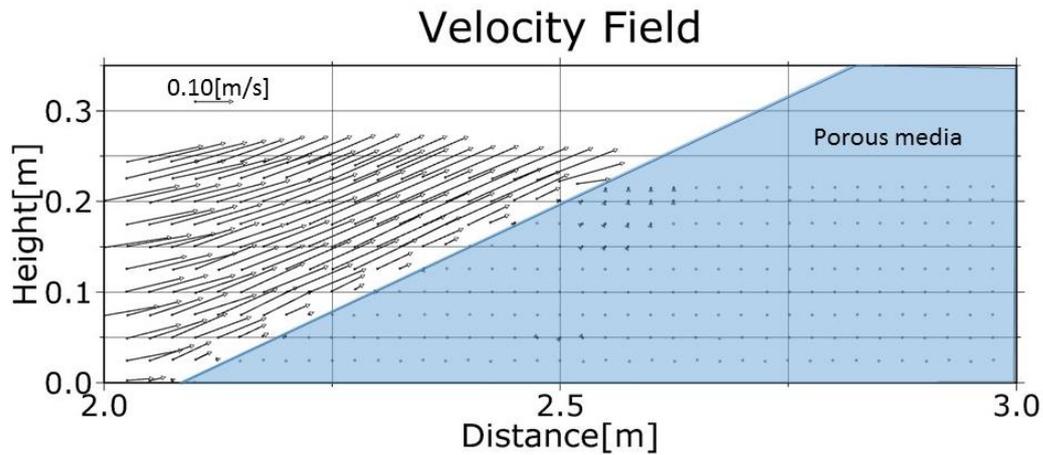
(a) $t = 3.25$ [s]
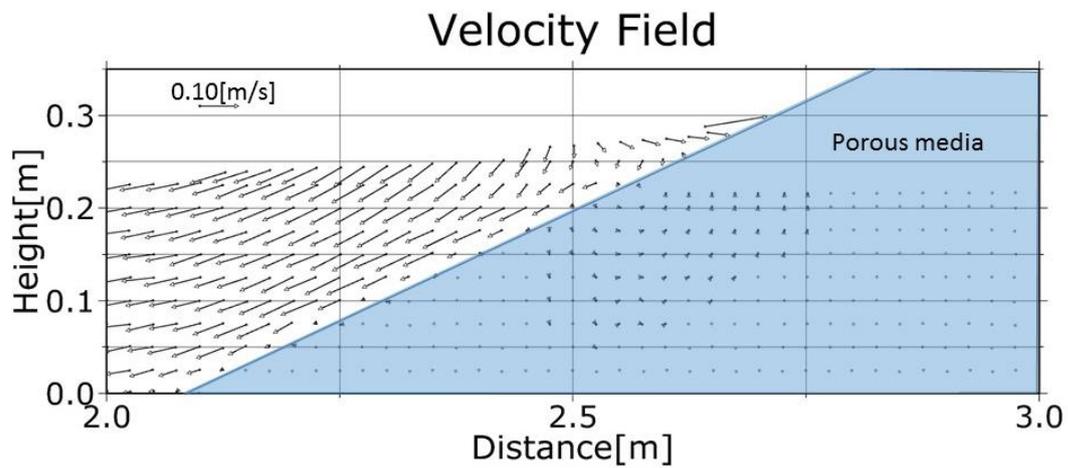
Velocity Field

(b) $t = 3.95$ [s]

Figure 5.10 Velocity fields of the wave H = 0.03423 [m] with Dc = 0.25 [mm]

If the mean grain size is relatively large, fluid particles can move into the porous area. Figure 5.11 presents the velocity fields of the wave H = 0.03423 [m] ($H/h_0 = 0.163$) with the mean grain diameter of 1.0 mm. When the wavefront reached the permeable beach, fluid particles did not lose the horizontal velocity and moved into the porous area. The velocity of fluid particles pointed lower rightward inside the porous media. The runup height consequently became smaller as mean grain size became larger.

110

Velocity Field
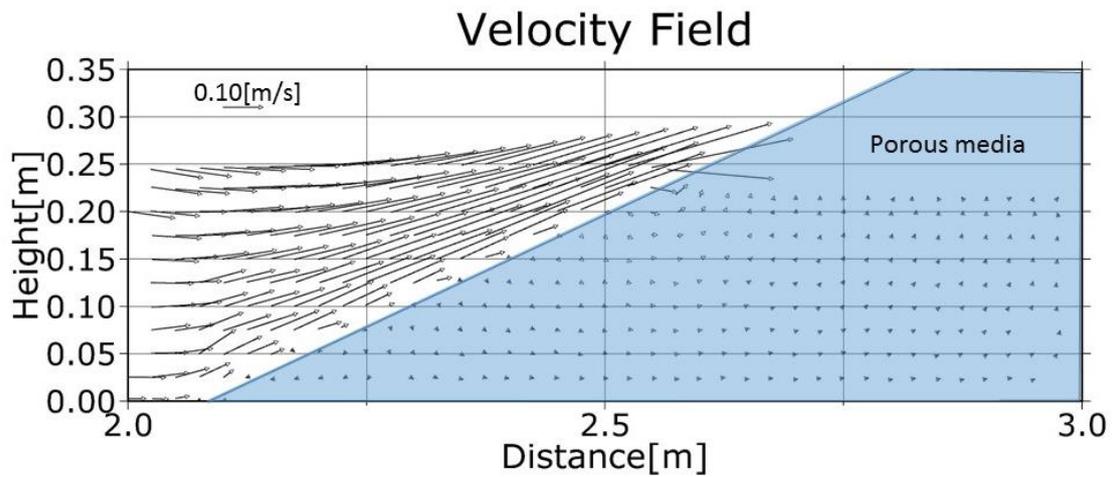
(a) $t = 3.50$ [s]
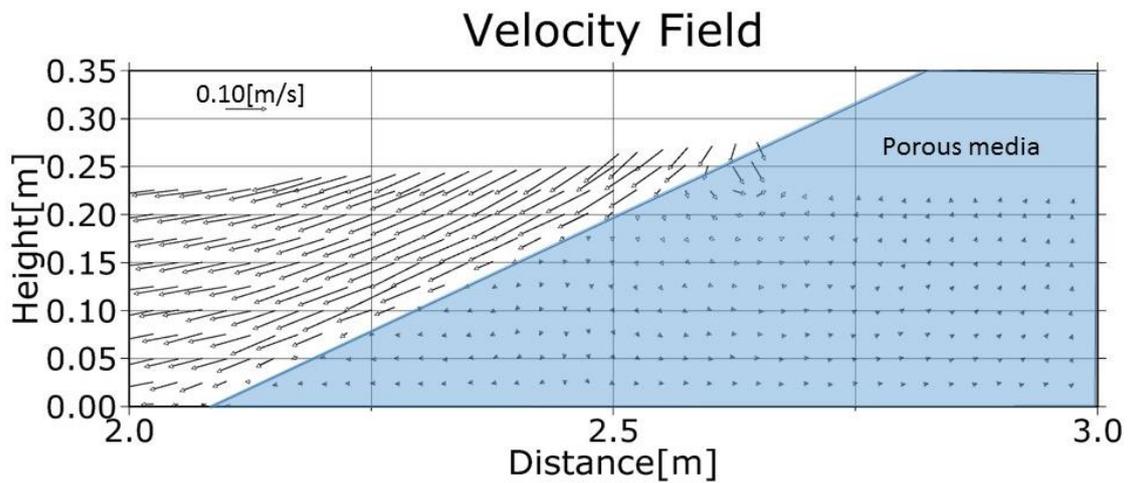
Velocity Field

(b) $t = 4.05$ [s]

Figure 5.11 Velocity fields of the wave H = 0.03423 [m] with Dc = 1.0 [mm]

In Figure 5.12, the power trendline for the wave H = 0.03423 [m] ($H/h_0 = 0.163$) can be estimated as:

$$y = 73.157x^{-0.050} \tag{5.4.1}$$

and, as:

$$y = 131.46x^{-0.054} \tag{5.4.2}$$

for the wave H = 0.0525 [m] ($H/h_0 = 0.25$).
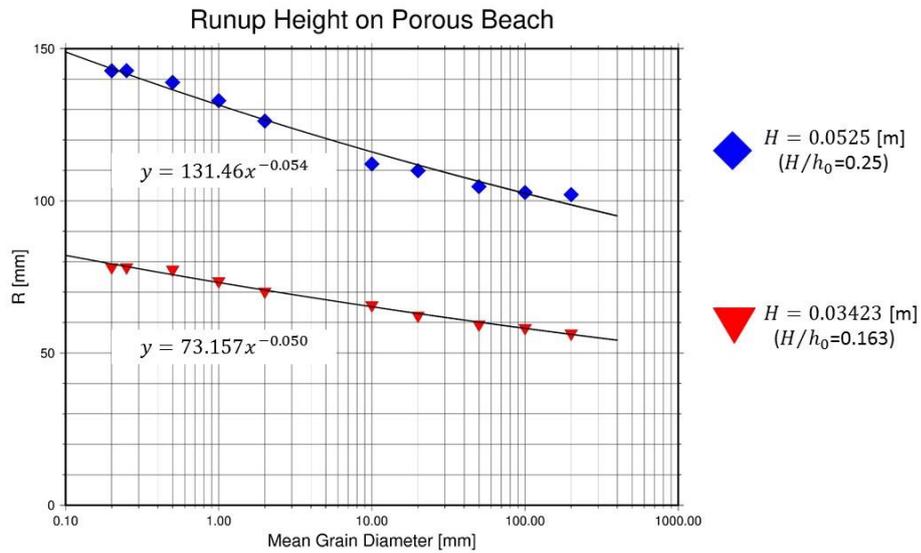
Figure 5.12 Trendlines for runup on a 1:2.08 porous beach

Following the runup height laws for solid slopes, the runup height on permeable beaches can be expected as

$$R = k_1 \frac{h_0}{H^{k_2}} Dc^{k_2} \tag{5.4.3}$$

where k_1 and k_2 are coefficients. From Equations (5.4.1) and (5.4.2), k_2 can be estimated around -0.052 and k_1 will be

$$
\begin{aligned}
k_1 &\fallingdotseq 0.290 \quad \text{for } H = 0.03423 \text{ [m]} \\
k_1 &\fallingdotseq 0.509 \quad \text{for } H = 0.0525 \text{ [m]}
\end{aligned}
\tag{5.4.4}
$$

Assuming that k_1 can be written as

$$k_1 = k_3 \frac{R_s}{h_0} \tag{5.4.5}$$

where $\frac{R_s}{h_0}$ is the runup height on the same scale solid slope with the same wave height H, k_3 can be estimated around 0.61 for both waves. The runup law for the wave propagating on a 1:2.08 permeable slope can be expected as

112

$$R = 0.61 \frac{R_s}{H^{-0.052}} Dc^{-0.052} \qquad (5.4.6)$$

In Figure 5.13, the dashed lines represent the estimated runup height for two waves obtained through Equation (5.4.6). For the H = 0.03423 [m] wave, the estimated runup height strongly agrees with the simulated runup height in any size of the mean grain diameter. Although Equation (5.4.6) tends to slightly overestimate the height when the grain size is relatively large for the wave H = 0.0525 [m], the overall estimation is satisfactory.
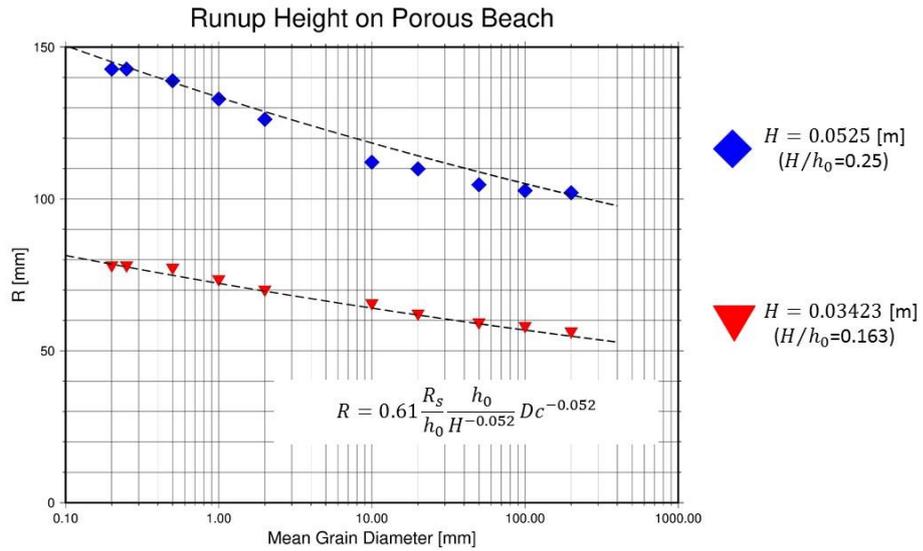
Figure 5.13 Runup law for a 1:2.08 permeable beach

5.5 Wave runup on porous layers

5.5.1 Numerical setup

In this section, another type of porous media is arranged. The schematic diagram of the computational domain is presented in Figure 5.14. The parallelogram porous media was placed at $x = 2.07$ and the slope scale is 1:2.08 ($\varphi \approx 25.68°$). The generated wave height was H = 0.03423 [m] ($H/h_0 = 0.163$) and H = 0.0525 [m] ($H/h_0 = 0.25$). The porosity

of the porous layers was fixed at 0.49, and various grain sizes were tested. The thickness of the porous layers is varied at 13.0 cm, 19.5 cm, and 43.3 cm. The highest point of the flow at the water-porous boundary was defined as the runup hight. The numerical parameters are listed in Table 5.3.
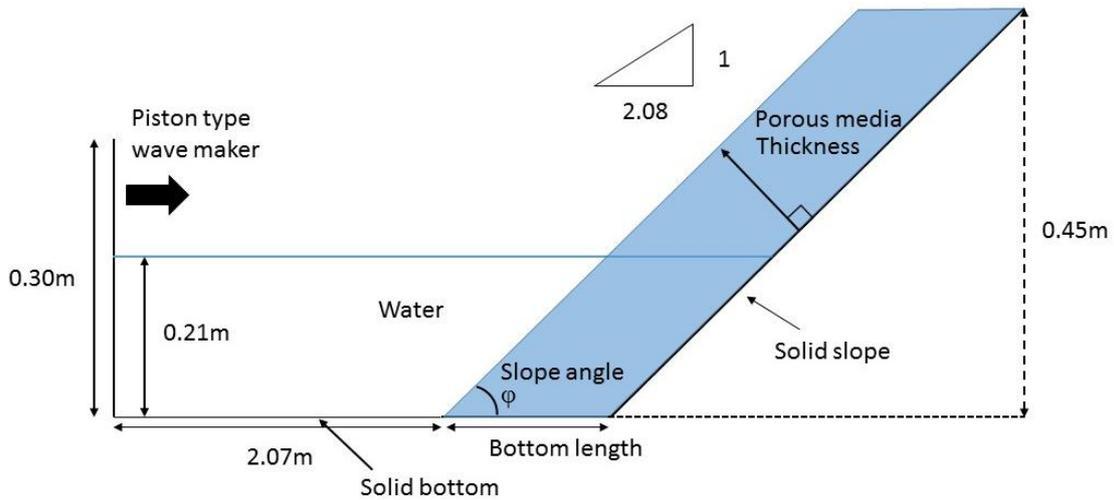
Figure 5.14 Setting of a 1:2.08 porous layers flume

Table 5.3 Computational parameters for wave runup on 1:2.08 porous layers

Parameters	Value
Diameter of particles	0.005 m
Initial particle spacing	0.005 m
Smoothing length	0.0085 m
Initial time step	0.00025 sec
Courant number	0.2
Smagorinsky constant	0.1
Combination ratio of the source term	0.97
Mean grain diameter of porous media	0.20 mm, 0.25 mm, 0.50 mm, 1.0 mmm, 2.0 mm, 10.0 mm, 20.0 mm, 30.0 mm, 40.0 mm, 50.0 mm, 100.0 mm, 200.0 mm
Bottom length of porous layers	30 cm, 45 cm, 100 cm
Thickness of porous layers	13.0 cm, 19.5 cm, 43.3 cm

5.5.2   Results and analysis

Figures 5.15 and 5.16 describe the snapshots of solitary wave runup on 13.0-cm thick porous layers, with the mean grain size Dc = 1.0 [mm] and 0.25 [mm], respectively. The initial wave height is 0.03423 m.
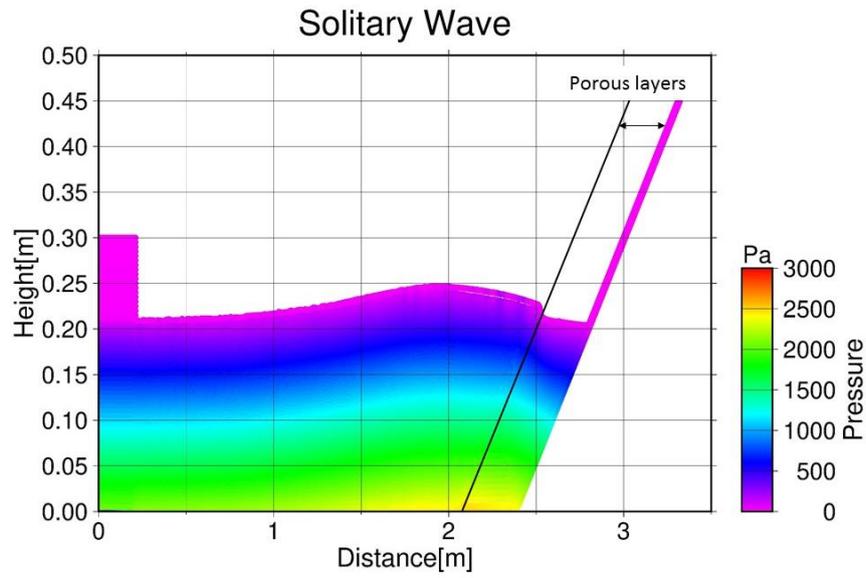
(a) $t = 3.25$ [s]
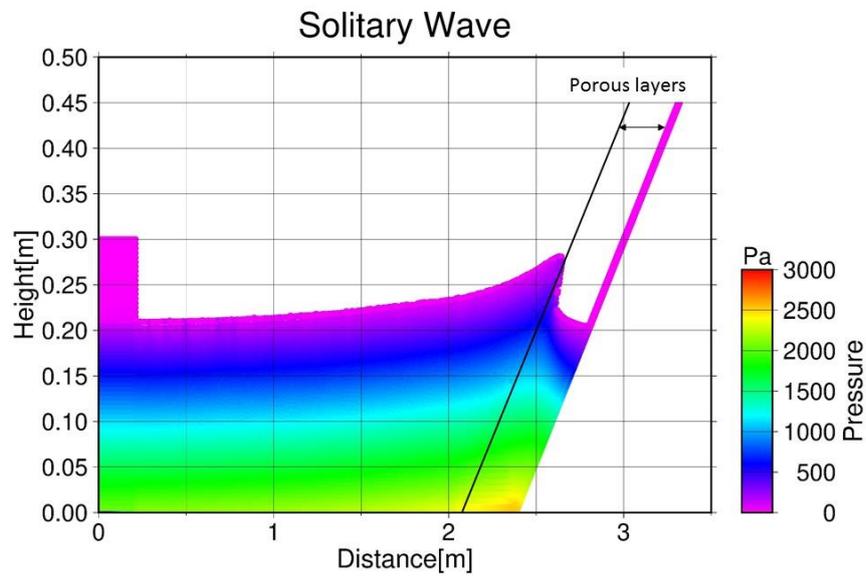
(b) $t = 3.95$ [s]

Figure 5.15 Wave runup on 13.0-cm thick porous layers with Dc = 1.0 [mm] (H = 0.03423 [m])
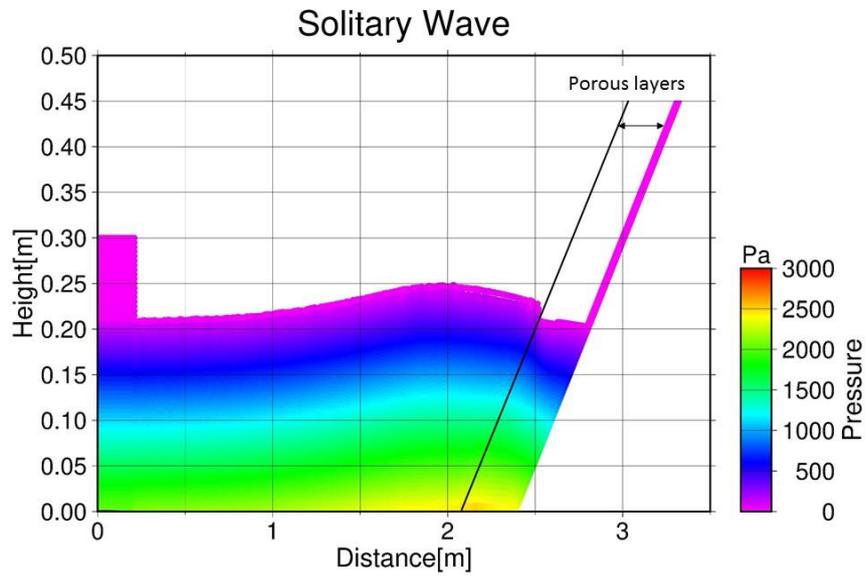
(a) $t = 3.25$ [s]
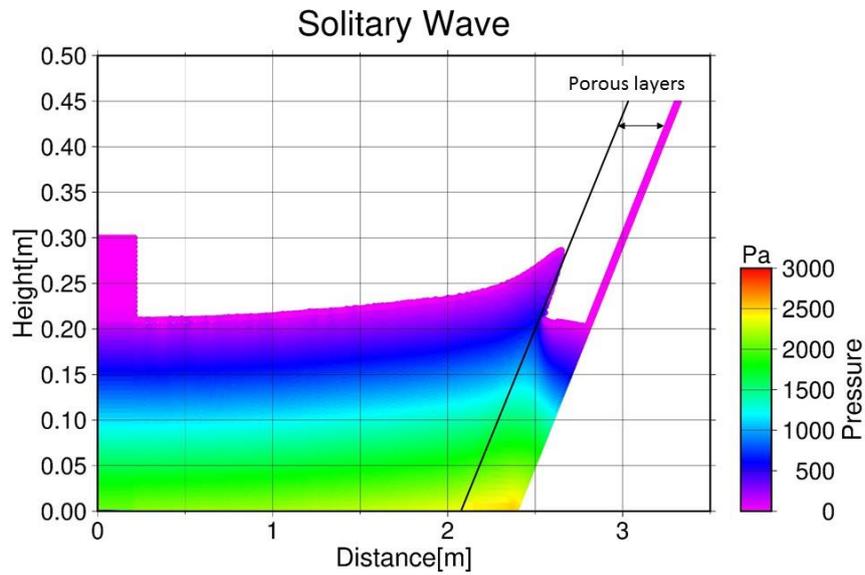
(b) $t = 4.00$ [s]

Figure 5.16 Wave runup on 13.0-cm thick porous layers with Dc = 0.25 [mm] (H =

0.03423 [m])

Both Figures 5.15 and 5.16 describe the accurate pressure fields during the runup process.

In Figures 5.15 (a) and 5.16 (a), the shape of the wave was the same regardless of the

116

grain size when the wave reached the porous region. If the grain size is 1.0 mm, some fluid particles penetrated the water-porous boundary (Figure 5.15 (b)), while fluid particles slid on the porous layers if the grain diameter is 0.25 mm (Figure 5.16 (b)).

Figure 5.17 compares the runup height of the wave $H = 0.03423$ [m] ($H/h_0 = 0.163$) with the three thickness cases (13.0 cm, 19.5 cm, and 43.3 cm) and various diameter sizes of the porous media. Notably, the horizontal axis is logarithmic. Overall, the runup height decreases nearly linearly as the mean grain diameter increases logarithmically. Similar to the permeable beach case, the height converges at around 80 mm, but it is unlikely to reach the runup height on a solid slope. Almost the same height is obtained, regardless of the thickness of the porous media until the grain size becomes 30.0 mm. When the mean grain diameter is larger than 40.0 mm, the runup height of the 43.3 cm thickness case becomes lower than the other two thickness cases. There is no difference in height between the 13.0 cm and 19.5 cm cases even if the grain size is larger than 40.0 mm.
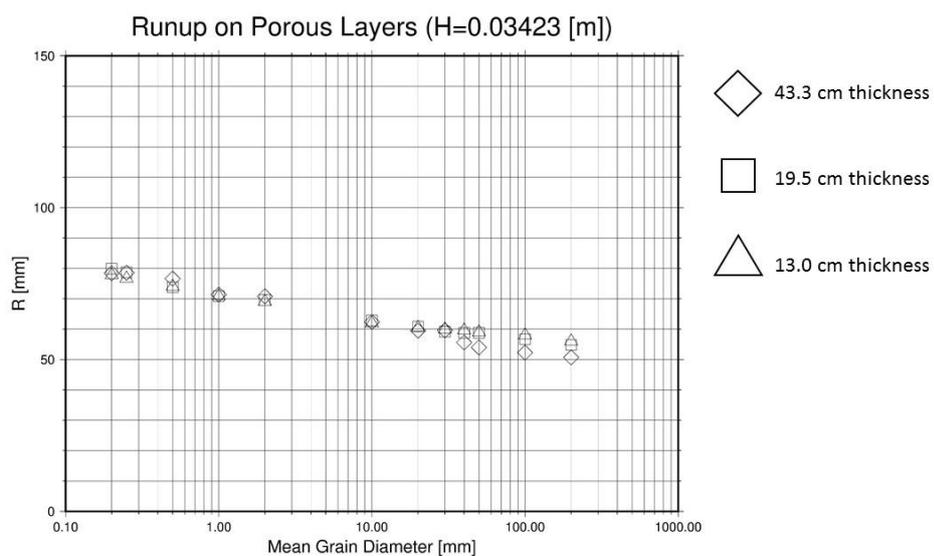
Figure 5.17 Runup height of the wave H = 0.03423 [m] on 1:2.08 porous layers

Figure 5.18 shows the velocity fields of the grain size 2.0 mm when the flow reached the highest point in the 13.0 cm and 43.3 cm thickness cases. Although some fluid particles could penetrate the porous layers and move into the porous region, they lost their velocity inside the porous media. These fluid particles consequently stayed around the water-porous boundary and could not approach the solid slope on the right side. The same runup height was thus obtained in both the 13.0 cm and the 43.3 cm thickness cases.
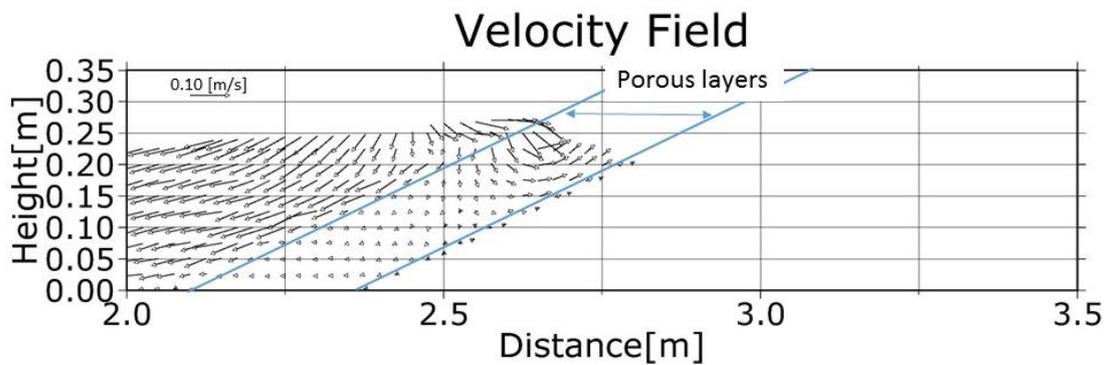
(a) 13.0-cm thick porous media
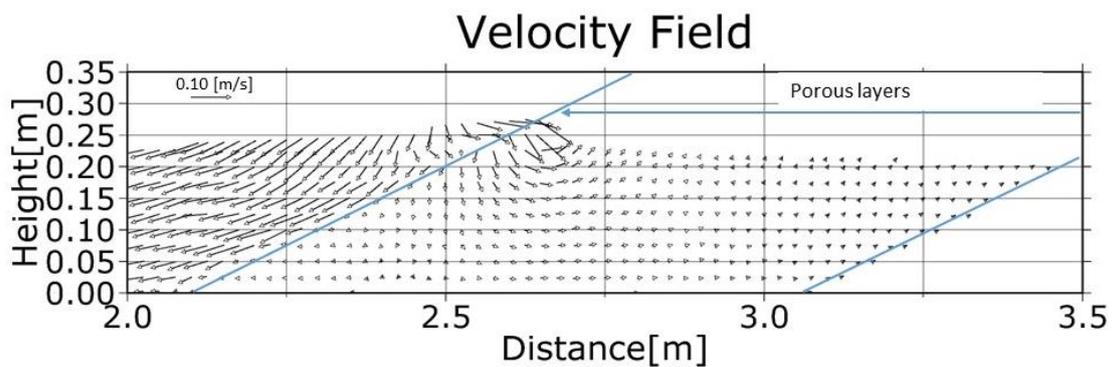
(b) 43.3-cm thick porous media

Figure 5.18 Velocity fields of the H = 0.03423 wave [m] with Dc = 2.0 [mm]

The velocity fields of the grain size 40.0 mm when reaching the highest point are presented in Figure 5.19 (a) for 13.0-cm thickness and (b) for 43.3-cm thickness. In both

cases, some fluid particles could move from the pure water are into the porous layers. After penetrating the water-porous boundary, fluid particles could reach the solid wall at the right end of the 13.0-cm thick porous media. In contrast, if the thickness is 43.3 cm, particles must propagate for a longer distance until they reach the right slope. Fluid particles did not stay around the water-porous boundary, but more partices propagated towards the solid boundary on the right side of the wave flume. The runup height thus became lower than 13.0 cm and 19.5 cm thickness cases. Notably, only the 43.3-cm thick porous layers affect the runup height with the relatively large grain size.
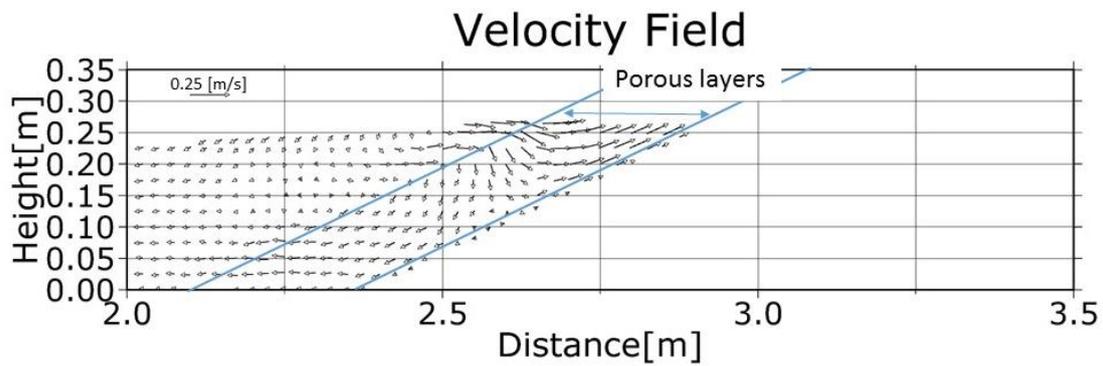
(a) 13.0-cm thick porous media
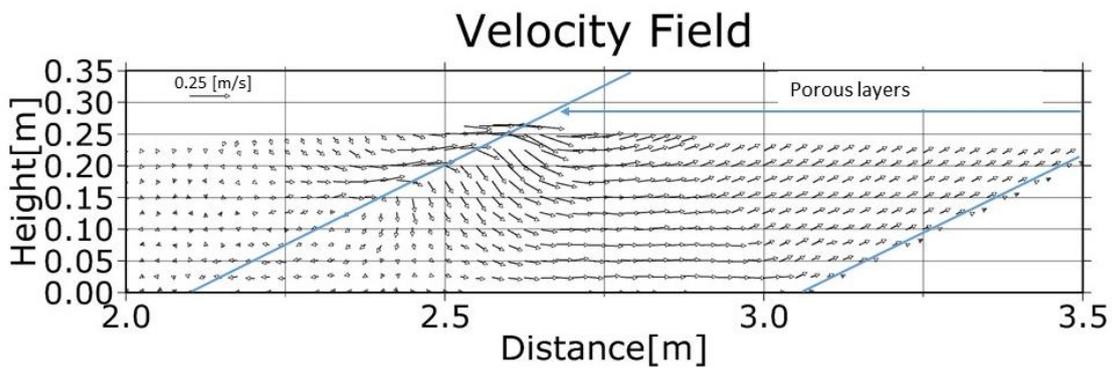
(b) 43.3-cm thick porous media

Figure 5.19 Velocity fields of the H = 0.03423 [m] wave with Dc = 40.0 [mm]

119

For the H = 0.0525 [m] wave, Figures 5.20 and 5.21 describe the snapshots of solitary wave runup on 13.0-cm thick porous layers, with the mean grain size Dc = 1.0 [mm] and 0.25 [mm], respectively. The smooth and continuous pressure fields were obtained in both cases. At $t = 3.00$ [s], the wavefront reached the porous region in Figures 5.20 (a) and 5.21 (a). The shape of the wave corresponded each other. If the mean grain size of the porous layers is 1.0 mm, some fluid particles penetrated the porous region and they were newly contained inside the porous layers. In contrast, if the mean grain size is 0.25 mm, fluid particles could not move into the porous layers. The runup height looked larger in this case compared to the Dc = 1.0 [mm] case.
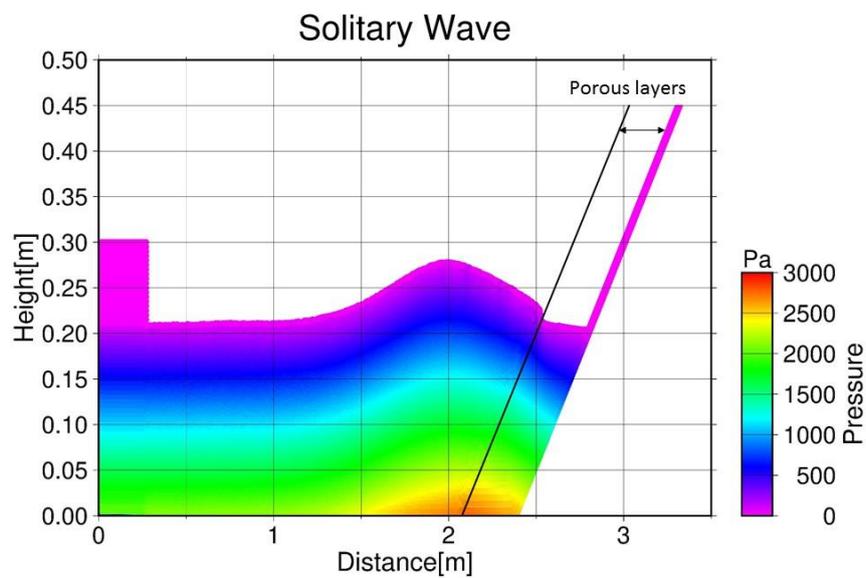
(a) $t = 3.00$ [s]
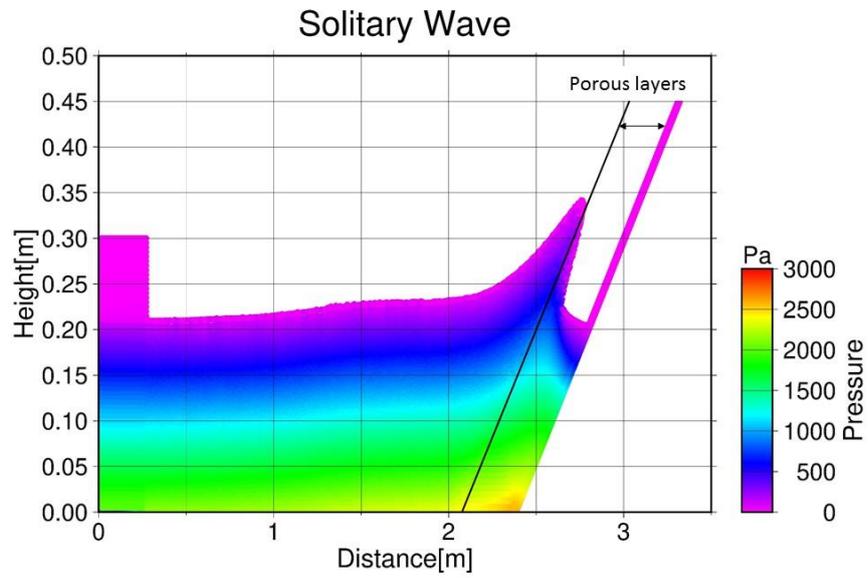
(b) $t = 3.70$ [s]

Figure 5.20 Wave runup on 13.0-cm thick porous layers with Dc = 1.0 [mm] (H =

0.0525 [m])
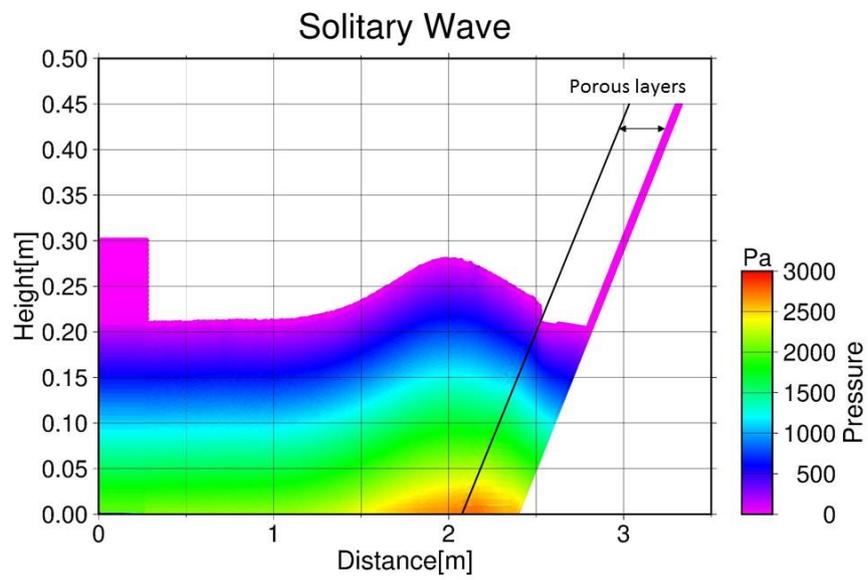
(a) $t = 3.00$ [s]
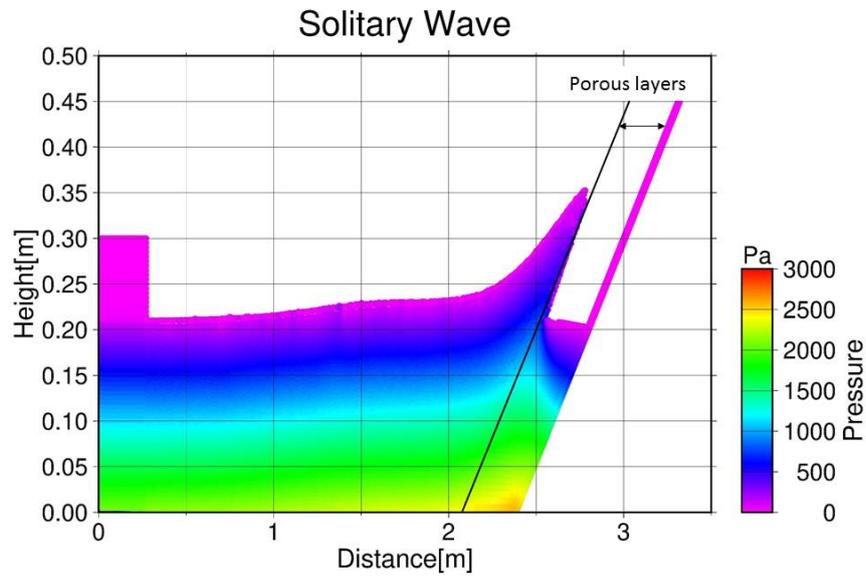
(b) t = 3.70[s]

Figure 5.21 Wave runup on 13.0-cm thick porous layers with Dc = 0.25 [mm] (H = 0.0525 [m])

The runup height of the wave H = 0.0525 [m] (H/h_0 = 0.25) on the porous layers is summarised in Figure 5.22. The runup height decreases nearly linearly and more rapidly than the H= 0.03423 [m] (H/h_0 = 0.163) wave cases as the mean grain of the porous layers increases logarithmically. The thickness of porous media does not affect the runup height until the grain size becomes 10.0 mm. If the mean grain diameter is 20.0 mm or larger, the 43.3-cm thick porous media yields lower runup height than the other two porous media.
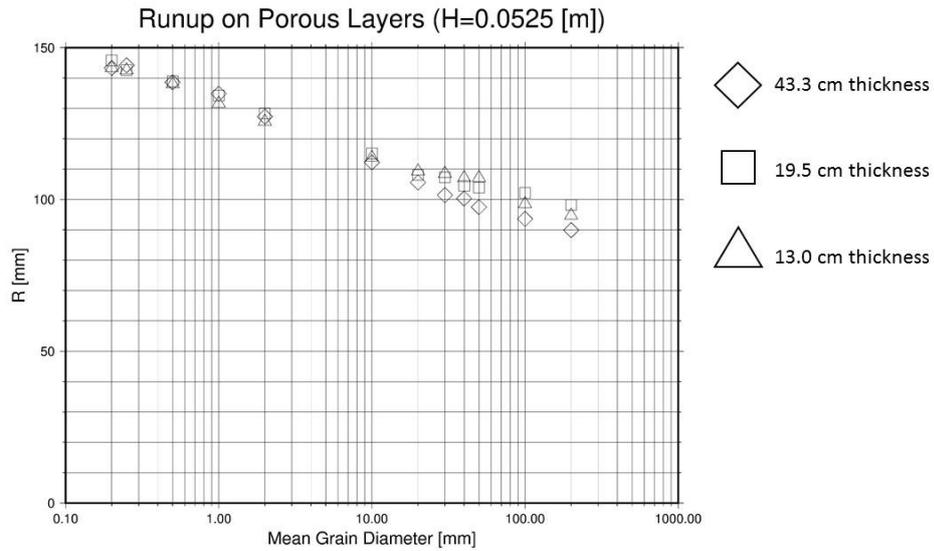
Figure 5.22 Runup hight of the wave H = 0.0525 [m] on 1:2.08 porous layers

Figures 5.23 and 5.24 show the velocity fields of the wave with Dc = 1.0 [mm] and Dc= 20.0 [mm] porous media in the different thickness, respectively. When the mean grain diameter was 1.0 mm, some fluid particles flowed into the porous layers as they connected with the wave crest and the mean water level inside the porous media, regarless of the thickness. However, their velocity was nearly zero, and they could not move freely in the porous region. The particles stayed around the water-porous boundary; thus, the runup height remained the same, regardless of the thickness of the porous layers. In contrast, fluid particles kept their horizontal velocity to some extent if the coarse porous material is placed. While the fluid particles propagated rightward, the runup height became lower in the 43.3-cm thick case.
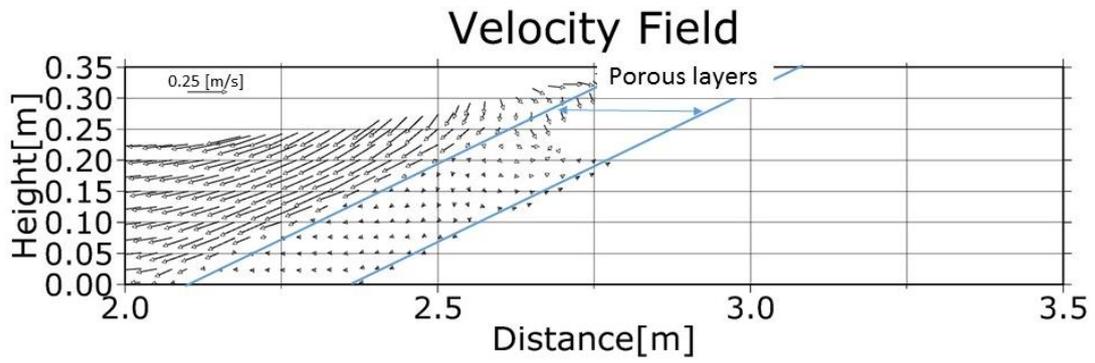
(a) 13.0 cm thick porous media
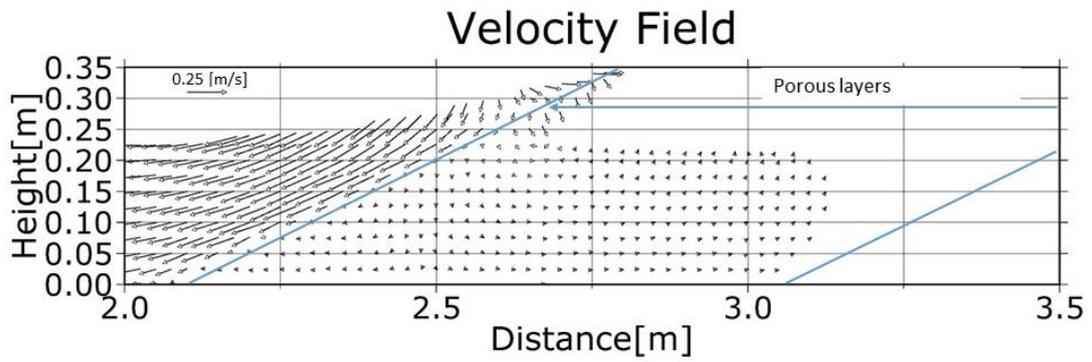
(b) 43.3 cm thick porous media

Figure 5.23 Velocity fields of the H = 0.0525 [m] wave with Dc = 1.0 [mm]
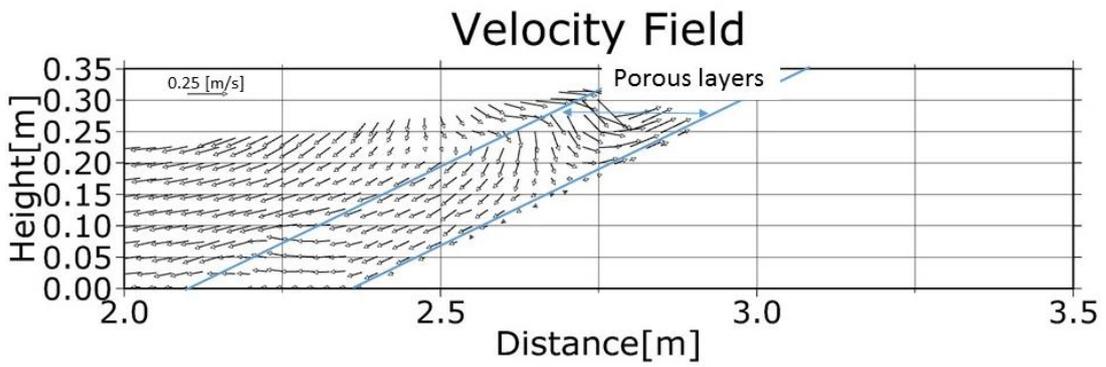
(a) 13.0 cm thick porous media
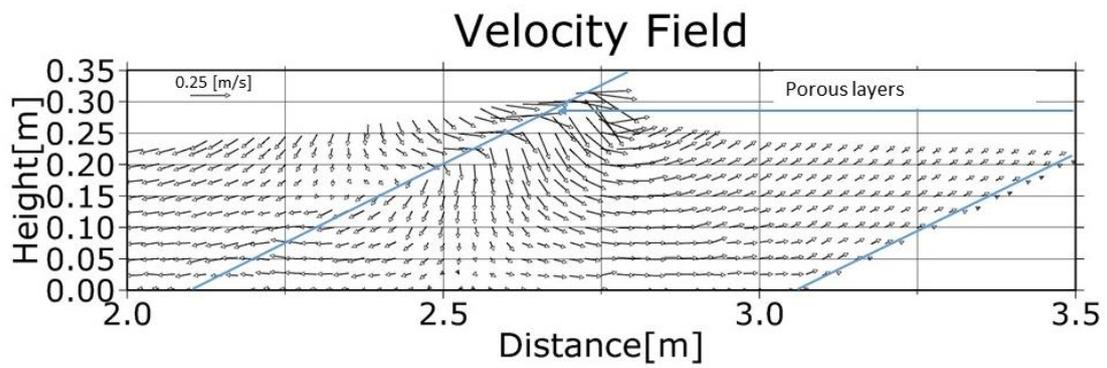
(b) 43.3 cm thick porous media

Figure 5.24 Velocity fields of the H = 0.0525 [m] wave with Dc = 20.0 [mm]

Chapter 6   Wave runup on a mild slope

6.1   Overview

Large-scale experiments of solitary wave runup on an idealised slope have been conducted to investigate the behaviour of tsunami waves in more practicable and natural conditions of beaches. As the wavelength of tsunamis is significantly long reaching a few hundred kilometres, its phase speed is proportional to water depth. In shallow water, while the speed of a tsunami becomes smaller, the height of a tsunami becomes larger. Tsunami waves moving in shallow water can break and cause more severe damage (Lo and Shao, 2002).

Hall and Watts's (1953) experiment is one of the earliest studies of solitary wave runup on a plane slope. Synolakis (1986) later conducted a number of experiments on solitary wave runup on a 1:19.85 scale slope. In his experiments, wave profiles were captured and compared with the analytical solutions. This 1:19.85, or more simply, 1:20 scale slope, has been conventionally utilised for both experimental and numerical modelling studies. Lin et al. (1999) investigated solitary wave runup and rundown on a 1:20 slope using the RANS model. They analysed the pressure fields and velocity fields during the runup and rundown processes. The wave profiles were compared with their experiments, the solutions of Boussinesq equations (Zelt, 1991), and the results of the shallow water equations (Titov and Synolakis, 1995). Xiao (2008) also utilised the RANS model, combined with the k-ε model, to investigate solitary wave runup on a 1:20 slope. Borthwick et al. (2006) used Boussinesq-non-linear shallow water equations model to investigate wave interactions with various large-scale slopes. Wei et al. (2006) presented a well-balanced finite-volume model for large wave runup. Tan and Chu (2010) compared

the simulation results of a Lagrangian Blocks on Eulerian Mesh (LBEM) model with Synolakis's (1986) experiments. In SPH, wave runup on a large-scale slope is simulated by both WCSPH (Dao et al., 2013) and ISPH (Atae-Ashtiani et al., 2008, Shadloo et al., 2015).

For more large-scale slopes, Hsiao et al. (2008), for instance, conducted experiments of wave runup on a 1:60 plane slope. However, as presented above, Synolakis's (1986) 1:19.85 (or 1:20) scale experiments have been widely referred to in various numerical models. Chang et al. (2009) conducted similar experiments following Synolakis (1986) and re-examined the motion of breaking waves with improved measurement equipment. The details of the wave runup process on 1:20 slopes are available.

Notably, all the above-mentioned studies investigated wave runup on an impermeable smooth slope, which has been described as a "beach" in some studies. Wave propagation through large-scale permeable beaches has not been intensively investigated. In this chapter, the present ISPH model is applied to simulations of solitary wave runup over a 1:20 scale porous beach. The following section briefly reviews solitary wave runup on a solid slope and discuss the the permeability of the beaches.

6.2   Prediction of runup height

The detailed theory has been explained in Section 5.2. This section introduces two resulting laws.

Synolakis (1986) proposed the equation

$$\frac{R}{h_0} = 1.109 \left(\frac{H}{h_0}\right)^{0.582} \tag{6.1.1}$$

for breaking waves on a 1:20 scale slope based on the maximum position of the shoreline. Meanhile, Hughes (2004) derived the following runup law for breaking solitary waves from the momentum flux:

$$\frac{R}{h_0} = (1.39 - 0.027 cot\varphi) \left(\frac{M_F}{\rho g h_0^2}\right)^{\frac{1}{2}} \tag{6.1.2}$$

6.3 Wave runup on a solid slope
6.3.1 Numerical setup

The slope is located at $x = 2.0$ [m], and the slope scale is 1:20 ($\varphi \approx 2.86°$). All of the flume walls are smooth and impermeable. The initial water depth h_0 is 0.21 m. The same numerical flume was used in Section 4.6.2. A solitary wave was generated by a piston-type wavemaker at the left end with the relative wave height of H/h_0 = 0.100, 0.188, 0.280, and 0.416. From Equation (5.2.2), the transition relative wave height is estimated around 0.0295, which means that the generated wave is expected to break during the running up process. The parameters for these simulations are listed in Table 6.1.

Table 6.1 Computational parameters for wave runup on a 1:20 solid slope

Parameters	Value
Diameter of particles	0.005 m
Initial particle spacing	0.005 m
Smoothing length	0.006 m
Initial time step	0.00025 sec
Courant number	0.2
Smagorinsky constant	0.1
Combination ratio of the source term	0.97

6.3.2   Results

Figure 6.1 shows the computed particle distribution of the experimental wave profile of $H/h_0 = 0.28$. The blue dots represent Synolakis's (1986) experiment data. Both x and y axis are normalised by the initial depth h_0. The mean water level is set to be zero, and $x/h_0 = 0$ refers to the location of the original shoreline. Time t^* is a nondimensional time in which t is divided by $\sqrt{\dfrac{h_0}{g}}$.

At $t^* = 15$ in Figure 6.1 (a), the wave reached the slope, and the wave height became larger than the initial height due to the shallower water. The wave shape became asymmetric at this phase. The wave in Synolakis's (1986) experiment leant forward slightly more strongly, but the overall shape in the ISPH simulation corresponded with the experimental wave profile. In Figure 6.1 (b), the wave leant further forward while running on the slope and began to break. Although the crest of the simulated wave was sharper, the shape of the breaking wave agreed well with the experimental results. At $t^* = 30$, the wave completely broke and moved upward on the solid slope. The present ISPH model reproduced the flow of Synolakis's (1986) experiment. At $t^* = 45$ in Figure 6.1 (d), the flow reached the highest point on the slope. However, there was a slight gap between the experimental results and the present ISPH simulation. The flow front was significantly thin and fluid particles could not reach the same point as the experiment. The free surface of the simulation results seemed not to be in contact with the main body of fluid, such that the profile differs from the experiment. Nevertheless, the overall wave profiles during running up were in agreement with the experiment, and the ISPH simulation results were acceptable.

(a) $t^* = 15$

(b) $t^* = 20$

(c) $t^* = 30$

(d) $t^* = 45$
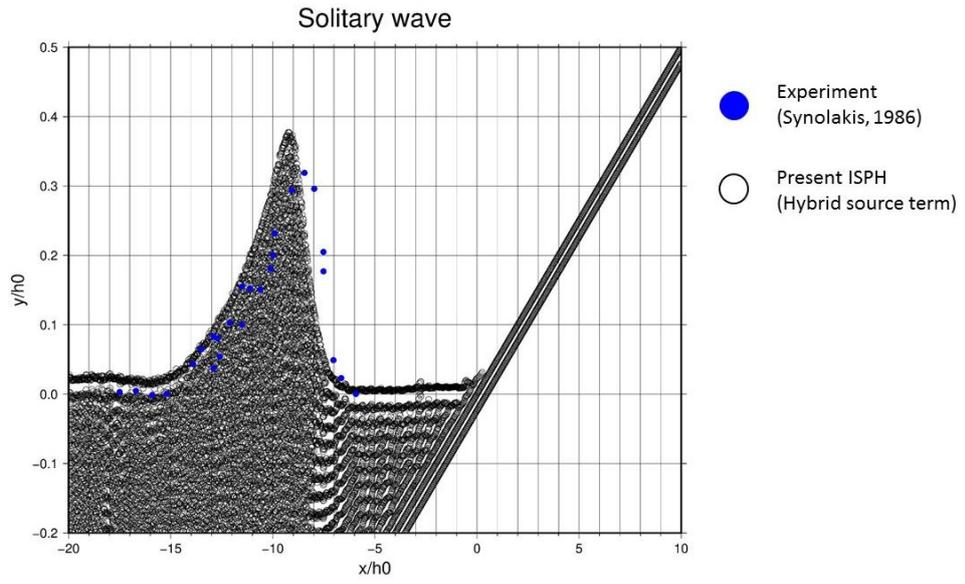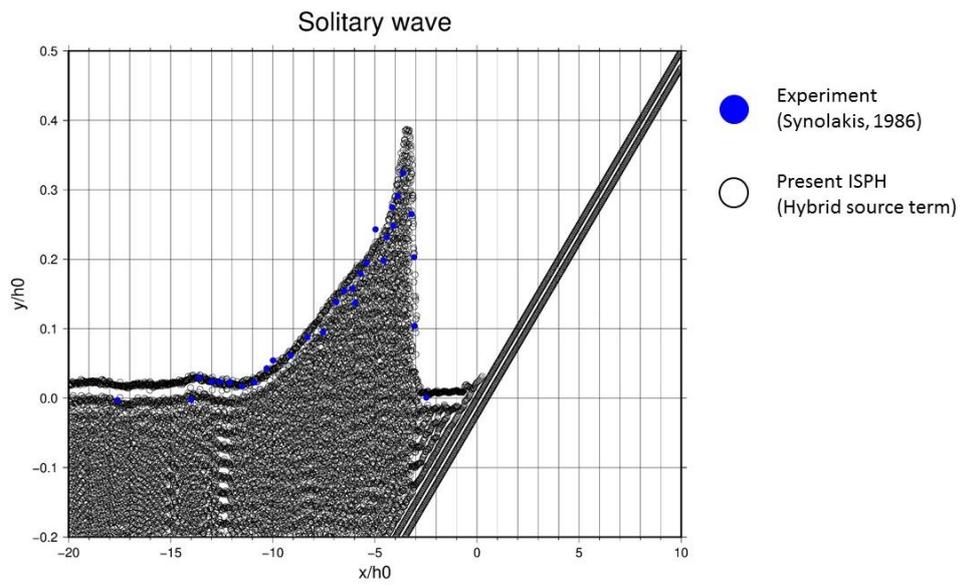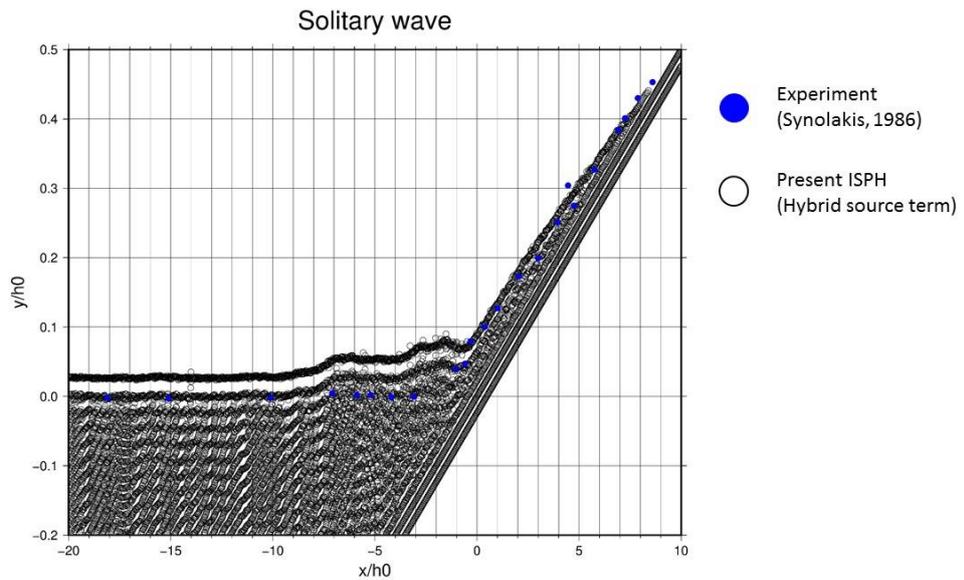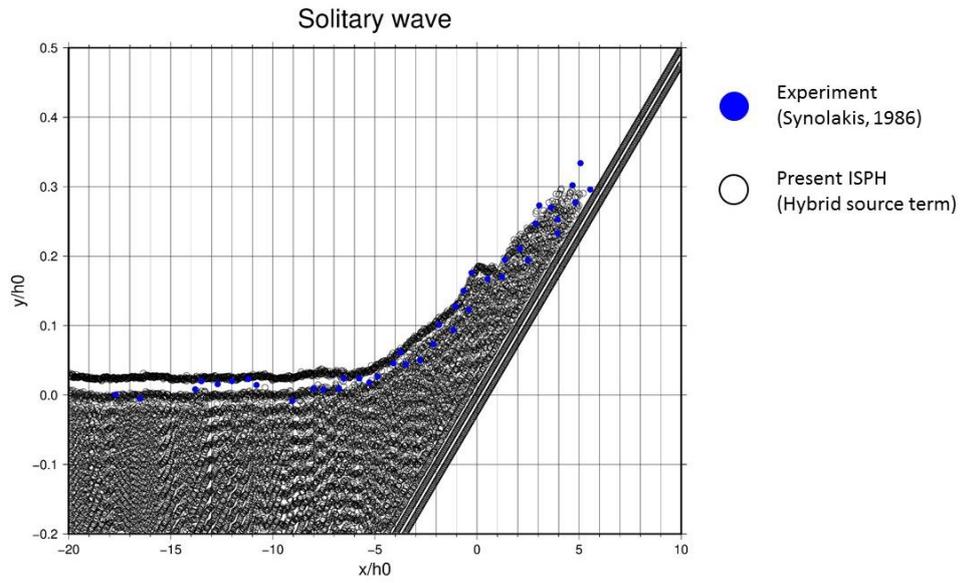
Figure 6.1 Particle distribution of wave runup and rundown on a 1:20 solid slope

Figure 6.2 compares the runup height with the present ISPH simulation results, the experiment data, and the theoretical solutions. Notably, both the nonbreaking and breaking wave runup laws are presented since some experimental results of a nonbreaking

wave have been included. The computed relative runup height was 0.445 with the wave $H/h_0 = 0.28$. The runup height simulated by the present ISPH tends to be slightly lower than that of the experiments'. However, the trend follows the analytical solutions, and Synolakis's (1986) runup height law is close to the ISPH results.
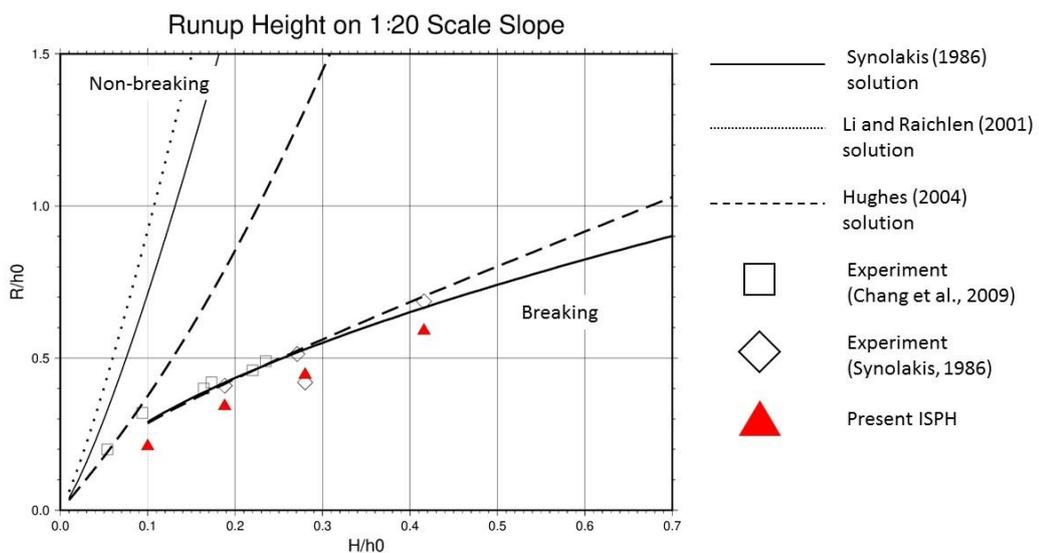
Figure 6.2 Runup height on a 1:20 solid slope

6.3.3 Discussion

In Section 5.3.3, the choice of the source term in the PPE was investigated in terms of runup height. This investigation led to the conclusion that the standard source term is limited to small waves, and that the hybrid source term can yield more accurate results regardless of the initial wave height. This section examines the possibility of using the standard source term to obtain the accurate runup height of breaking waves. The numerical settings are the same as those listed in Table 6.1, except that the combination ratio γ is set to zero.

Figure 6.3 compares the simulated particle distributions with Synolakis's experimental profile. The shape of the simulated breaking wave agreed well with the experiment results at $t^* = 15$ and 20. Similar to the results of the hybrid source term case, the crest of the wave was sharper and the height was overestimated. Nevertheless, the degree of wave's leaning forward in Figure 6.3 (a) showed better agreement compared to that shown in Figure 6.1 (a). At $t^* = 45$, the flow reached nearly the same point on the slope as the experiment. This fact implies that the resolution of the numerical settings is sufficient to simulate a thin wavefront. The simulated free surface was slightly over $y/h_0 = 0.0$.

Solitary wave

Experiment (Synolakis, 1986)

Present ISPH (Standard source term)

(a) $t^* = 15$

Solitary wave

Experiment (Synolakis, 1986)

Present ISPH (Standard source term)

(b) $t^* = 20$

Solitary wave

Experiment (Synolakis, 1986)

Present ISPH (Standard source term)
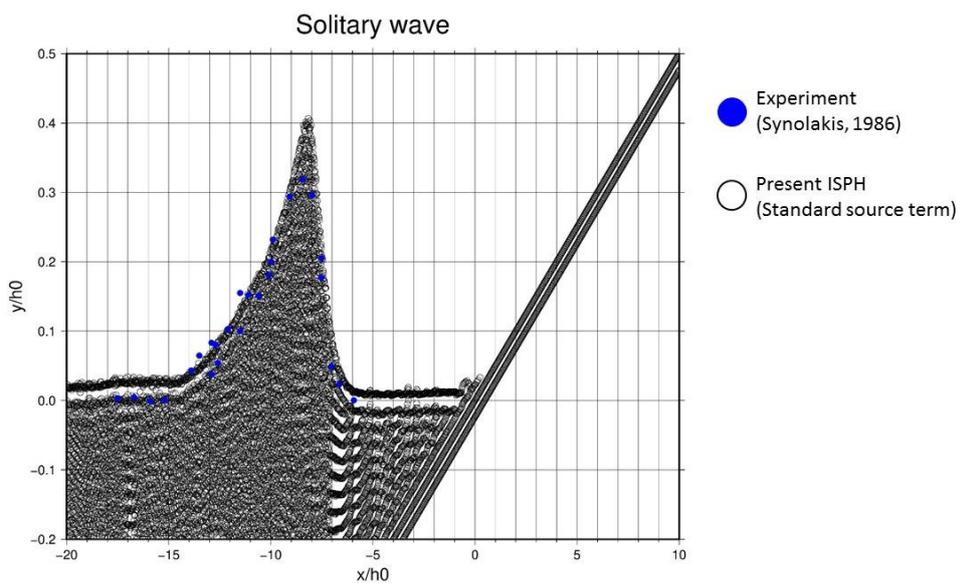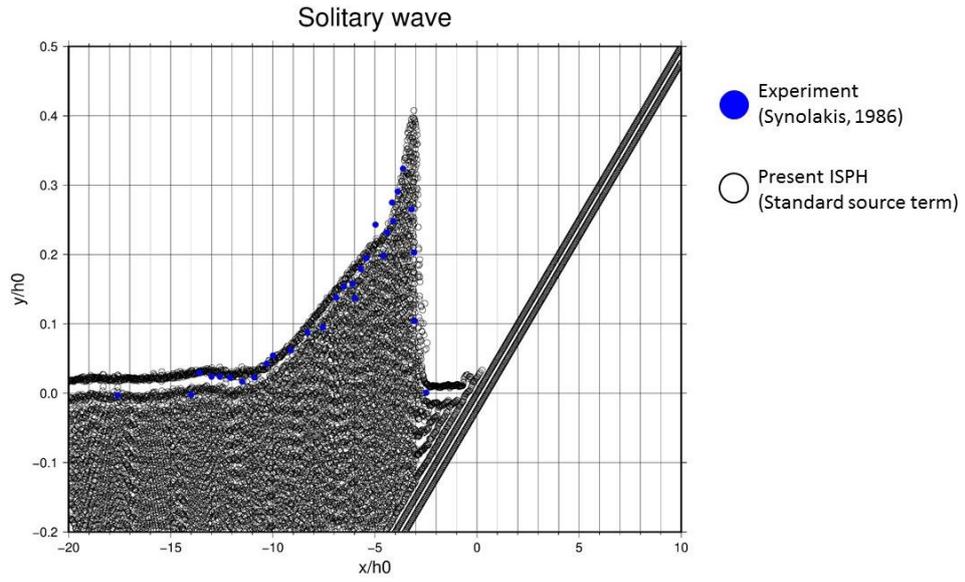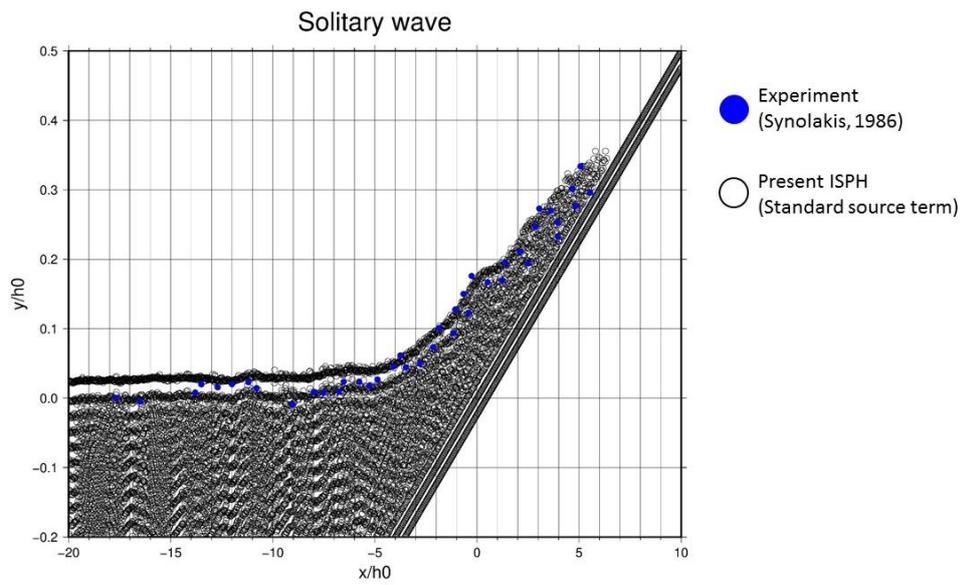
(c) $t^* = 30$
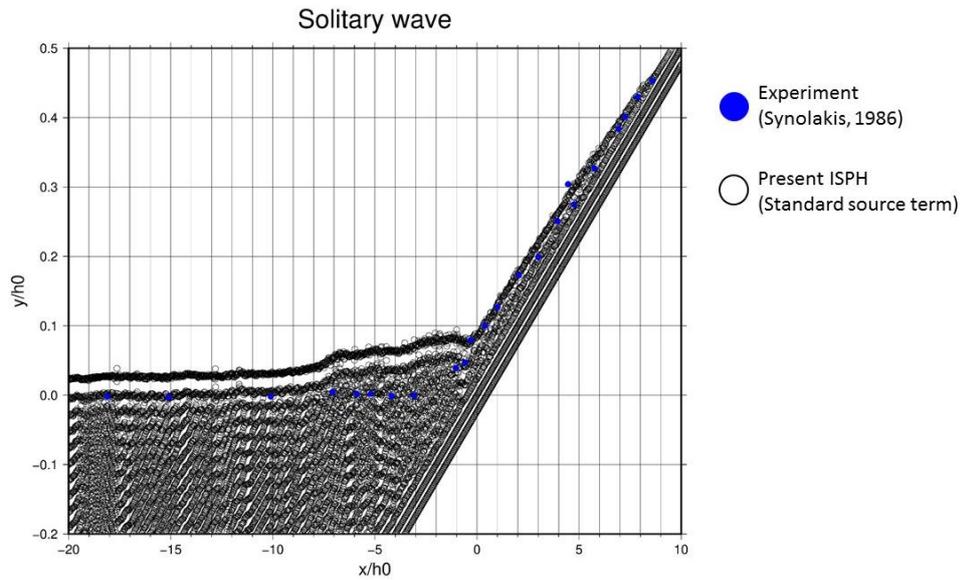
(d) $t^* = 45$

Figure 6.3 Particle distribution of wave runup and rundown on a 1:20 solid slope

obtained by the standard source term

Figure 6.4 shows the comparison of the standard deviation of the vertical surface profile between the ISPH simulation results and the experiment. The vertical surface profile of the existing experiment is regarded as the average, and the standard deviation is calculated in the hybrid and the standard source term cases. The horizontal axis t^* in figure 6.4 represents the normalised time scale. When the wave began to break at $t^* = 15$, the deviation is more significant in the hybrid source term case than in the standard source term case. However, during the breaking process, the deviation of the standard source term case becomes larger.
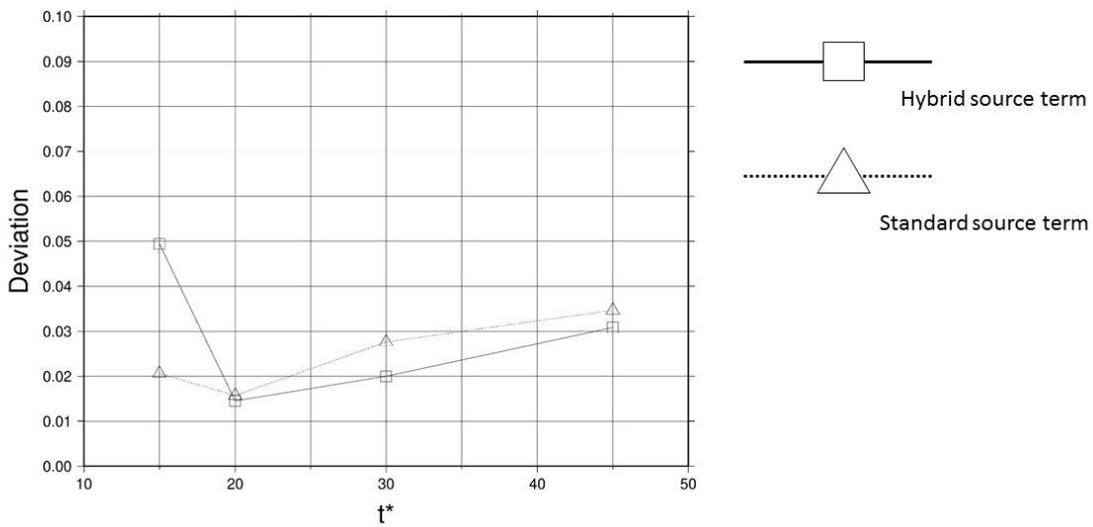
Figure 6.4 Standard Deviation of surface profile on a 1/20 slope

The simulation results of the ISPH with the standard source term only were compared with the experiments, the analytical solutions, and the ISPH results obtained by the hybrid source term in Figure 6.5. Similar to the hybrid source term case, the runup height yielded by the standard source term tends to be underestimated. As discussed in Section 4.6.2, simulations of breaking waves are prone to pressure fluctuations, and the hybrid source term can provide smooth pressure fields. Although the standard source term yields more accurate runup height than the hybrid source term, the difference is not significant. Considering smooth and accurate pressure fields, the hybrid source term is adopted in the following simulations.
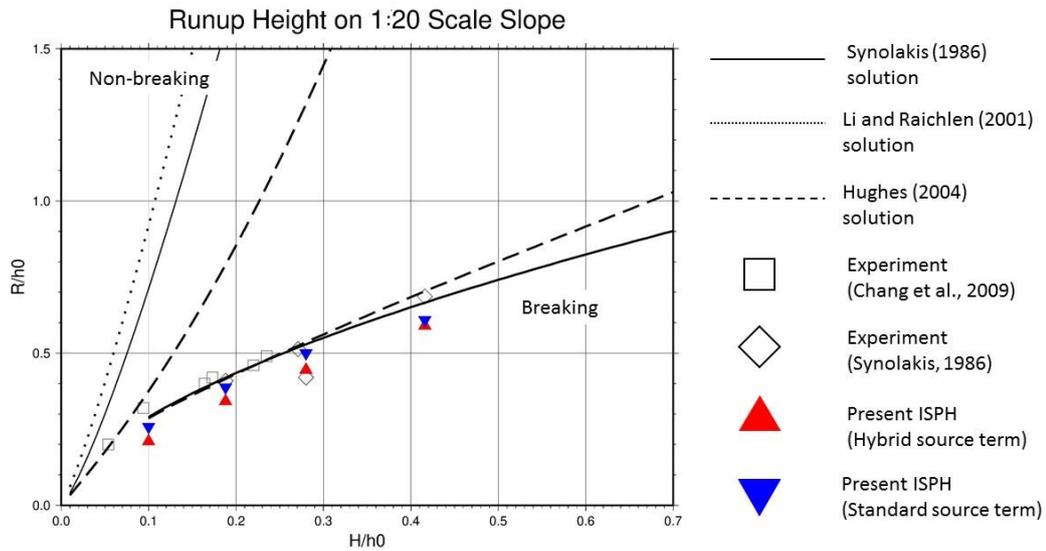
Figure 6.5 Runup height on a 1:20 solid slope obtained by the standard source term

6.4   Wave runup on a permeable beach

6.4.1   Numerical setup

In this section, the wave runup on a permeable beach is investigated. A triangle-shaped porous media is located at $x = 2.0 - 10.0$. The slope scale is 1:20.0 ($\varphi \approx 2.86°$). The schematic diagram of which is shown in Figure 6.6. Whereas the porosity of the porous media was fixed at 0.49, the mean grain diameter varied from 0.20 mm to 200.0 mm. The computational parameters are listed in Table 6.2. The initial water depth was 0.21 m, and the generated wave height was 0.0588 m ($H/h_0 = 0.28$). In these simulations, the runup height is defined as the highest point of the wave at the water-porous boundary.
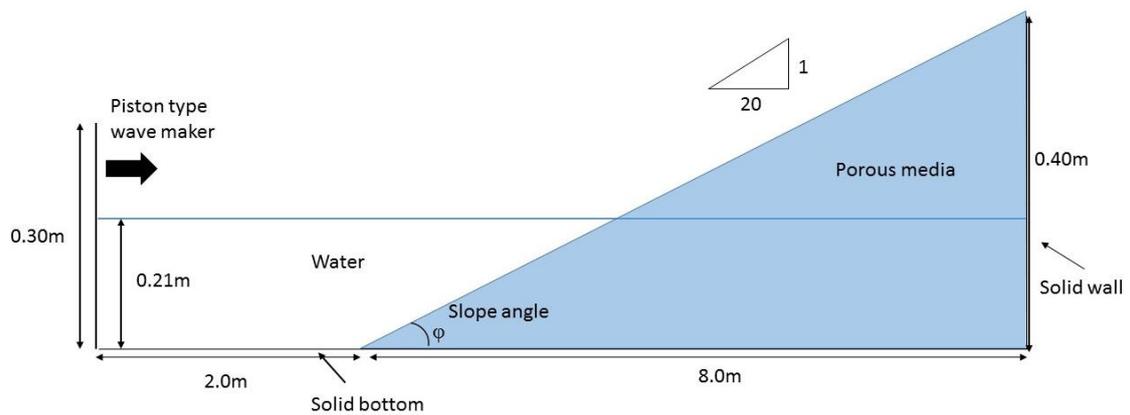
Figure 6.6 Setting of a 1:20 permeable beach flume

Table 6.2 Computational parameters for wave runup on a 1:20 porous beach

Parameters	Value
Diameter of particles	0.005 m
Initial particle spacing	0.005 m
Smoothing length	0.0085 m
Initial time step	0.00025 sec
Courant number	0.2
Smagorinsky constant	0.1
Combination ratio of the source term	0.97
Mean grain diameter of porous media	0.20 mm, 0.25 mm, 0.50 mm, 1.0 mm, 2.0 mm, 10.0 mm, 20.0 mm, 50.0 mm, 100.0 mm, 200.0 mm

6.4.2　　　　Results and analysis

Figures 6.7 and 6.8 describe the snapshots of solitary wave runup on a permeable beach, with the mean grain size of Dc = 1.0 [mm] and 0.25 [mm], respectively.
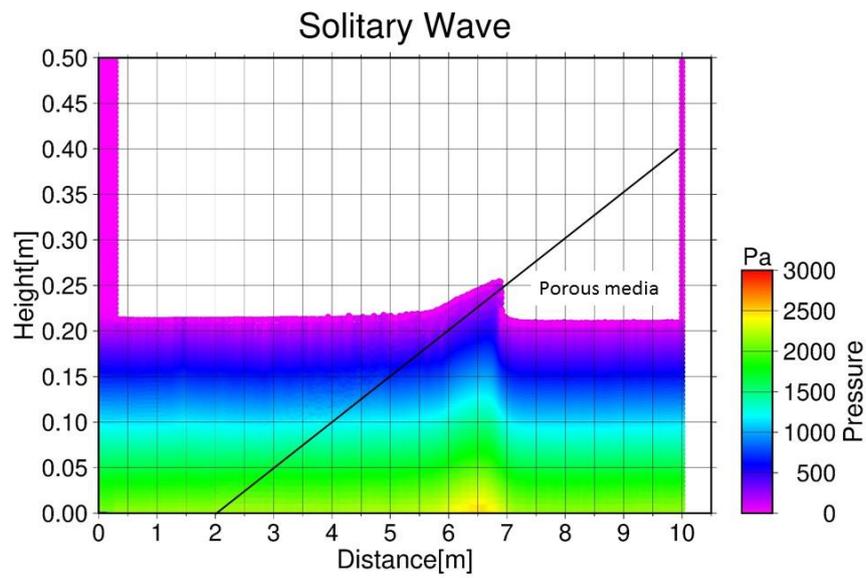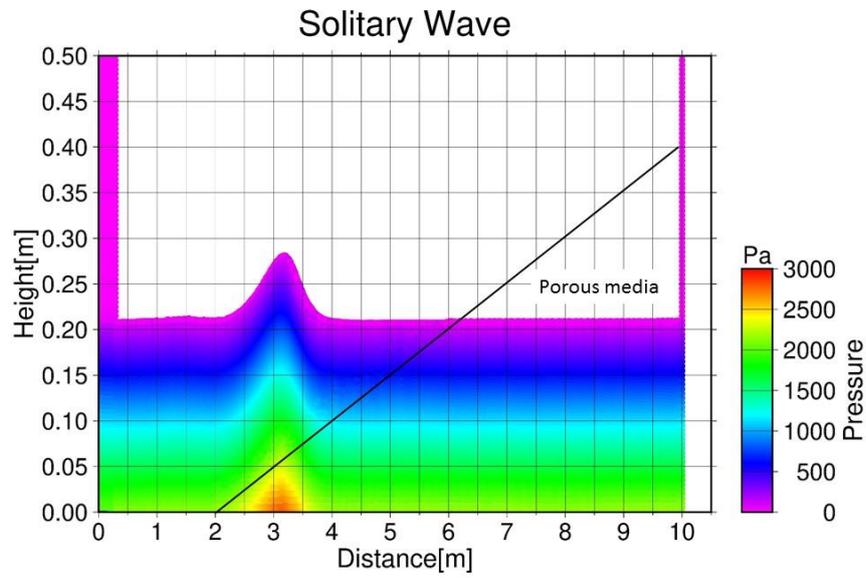
(a) $t = 6.00$ [s]

(b) $t = 10.25$ [s]

Figure 6.7 Wave runup on a 1:20 permeable beach with Dc = 1.0 [mm]
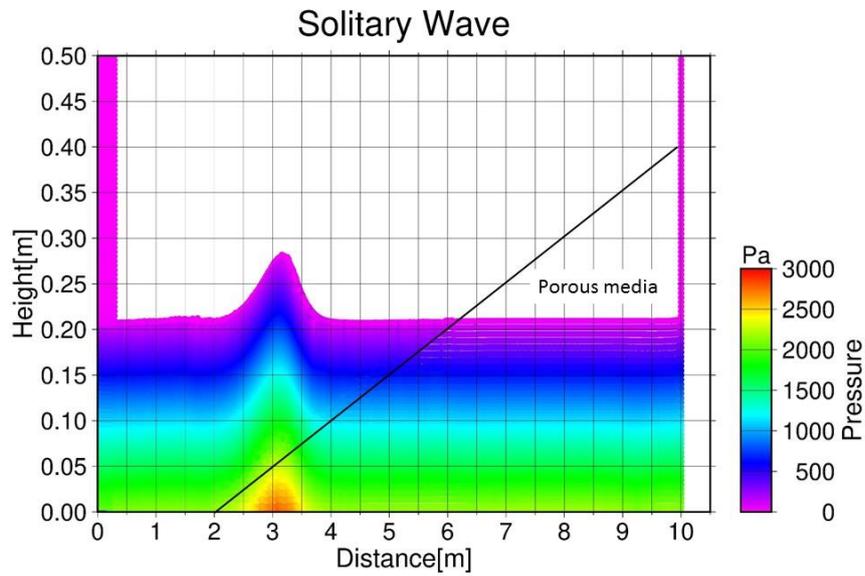
(a) $t = 6.00$ [s]
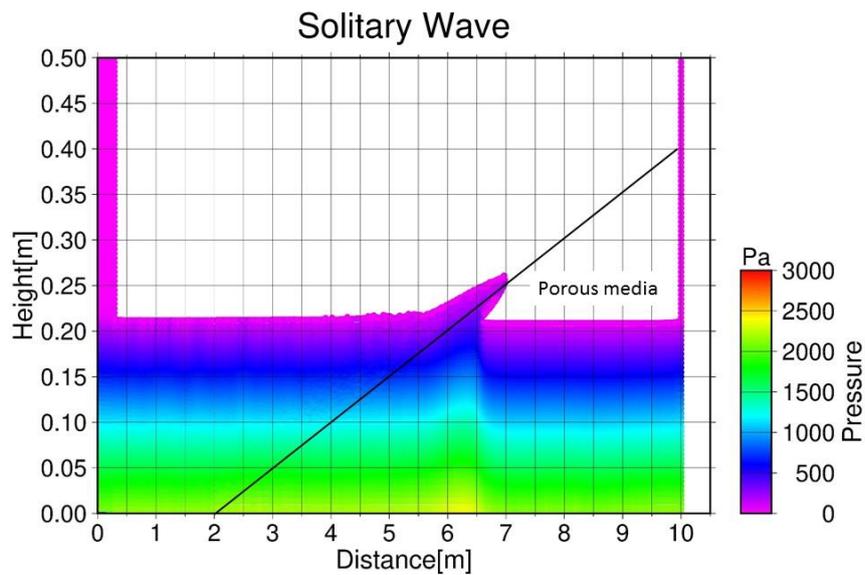
(b) $t = 10.25$ [s]

Figure 6.8 Wave runup on a 1:20 permeable beach with Dc = 0.25 [mm]

The smooth and continuous pressure fields were obtained for both grain size cases due to

the combination of the Wendland kernel and the hybrid source term. At $t = 6.00$ [s], the

incident wave reached the toe of the permeable beach and began to run up. The shape of

the wave became asymmetric at this phase. At $t = 10.25$ [s], the wavefront reached the

highest point on the beach. While the majority of the fluid particles were blocked by the porous medium, some particles could penetrate the water-porous boundary when the mean grain size of the porous medium is 1.0 mm. Conversely, if the grain diameter is 0.25 mm, fewer particles could move from the pure fluid region into the porous area.

Figure 6.9 summarises the runup height for various mean grain sizes. Notably, the horizontal axis is logarithmic. The runup height decreases nearly linearly as the mean grain diameter of the porous beach increases logarithmically, but it is absolutely impossible to reach the runup height on a solid slope even if the grain size is significantly small. Decrement of runup height is significant: When Dc = 0.25 [mm], runup height on the permeable slope decreases by 42% compared with the runup height on a solid slope.
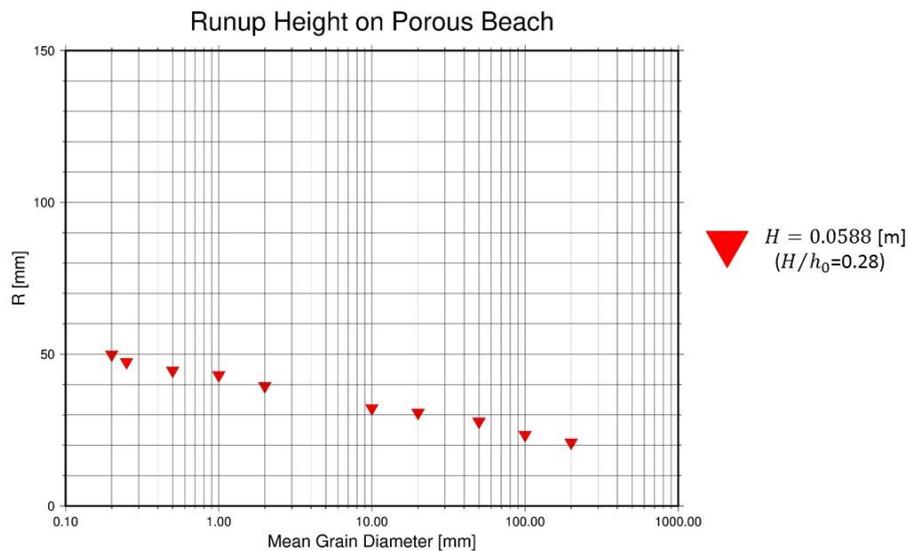
Figure 6.9 Runup height on a 1:20 permeable beach

Figure 6.10 plots the velocity fields of the wave with the mean grain diameter of 0.25 mm. Notably, the mean velocity at the grid size of 0.025 m is plotted and the dots represent the mean position of the particles. The propagating wave broke on the slope at $t = 8.50$ [s].

The fluid particles of the wavefront had a relatively large velocity. However, these particles lost their velocity due to frictional force from the permeable beach, and they had a small upper rightward velocity when the runup height was observed at $t = 10.25$ [s]. Almost no particles could move into the beach, they instead, slid on the slope. Fluid particles inside the beach had zero or nearly zero velocity, which means that they did not move during the simulation. If the grain size of porous media is sufficiently small, porous media works as if it were a solid structure.
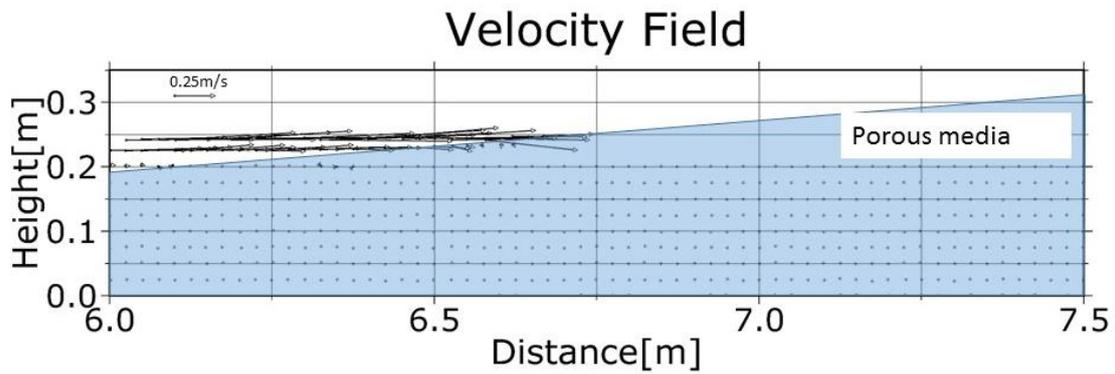
(a) $t = 8.50$ [s]
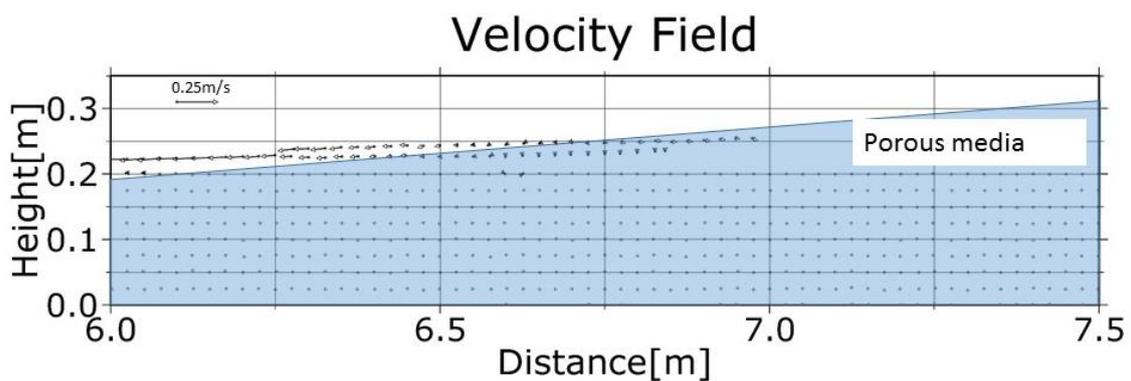
(b) $t = 10.25$ [s]

Figure 6.10 Velocity fields of the breaking wave with Dc = 0.25 [mm]

Fluid particles can move into a porous region if the mean grain size of porous media is relatively larger. The velocity fields with Dc = 1.0 [mm] are presented in Figure 6.11. The velocity fields in Figure 6.11 (a) were larger than the ones shown in Figure 6.10 (a) when the generated wave broke at t = 8.50 [s]. Some particles had the velocity in the lower-right direction when the runup height was observed (Figure 6.11 (b)). These particles moved into the porous area; thus, the runup height became smaller.
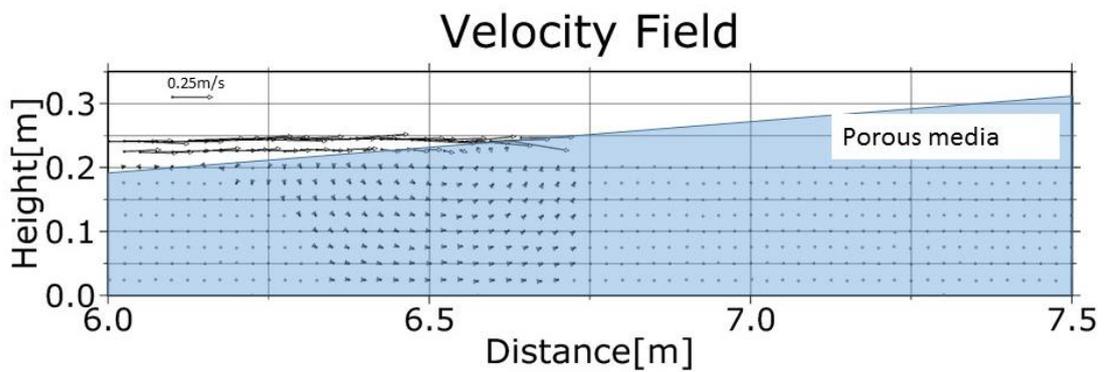
(a) t = 8.50 [s]
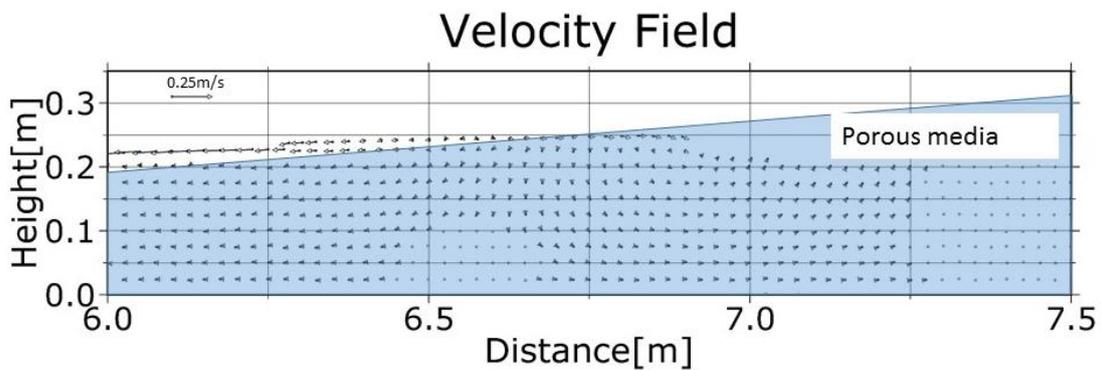
(b) t = 10.25 [s]

Figure 6.11 Velocity fields of the breaking wave with Dc = 1.0 [mm]

In Figure 6.12, the power trendline for the wave H = 0.0588 [m] can be obtained as:

$$y = 41.824x^{-0.119} \tag{6.4.1}$$

143
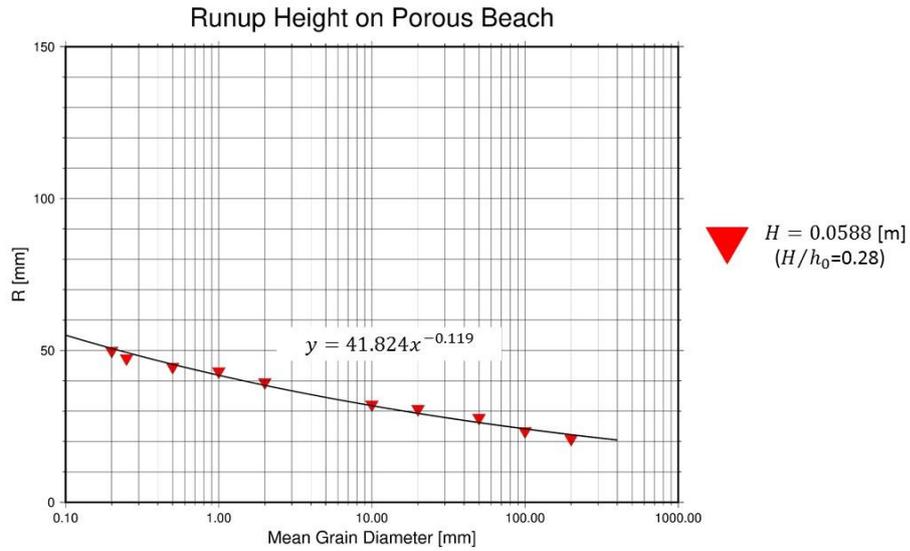
Figure 6.12 Trendline for runup height on a 1:20 porous beach

From the analysis in Section 5.4.2, the runup height on a permeable beach can be expected as

$$R = k_1 \frac{R_s}{h_0} \frac{h_0}{H^{k_2}} Dc^{k_2} \tag{6.4.2}$$

with the coefficients k_1 and k_2.

From Equation (6.4.1), k_2 is around -0.120 and k_1 can be estimated at around 0.27. The hypothetical runup law can be obtained as follows:

$$R = 0.27 \frac{R_s}{H^{-0.120}} Dc^{-0.120} \tag{6.4.3}$$

In Figure 6.13, the dashed line represents the estimated runup height on a 1:20 permeable slope obtained through Equation (6.4.3). The estimated runup height strongly agrees with the simulated runup height. This analysis implies that Equation (6.4.2) can be a consistent law for both 1:2.08 and 1:20 scale slopes even with the various wave height. This is due to the term $\frac{R_s}{h_0}$. The runup height on a solid slope is determined by the slope scale and the

144

generated wave height as presented in Equations (5.2.1), (5.2.3), and (5.3.6) for nonbreaking waves, Equations (6.1.1) and (6.1.2) for breaking waves. Equation (6.4.2) consequently includes the effects of the slope scale and the wave height.
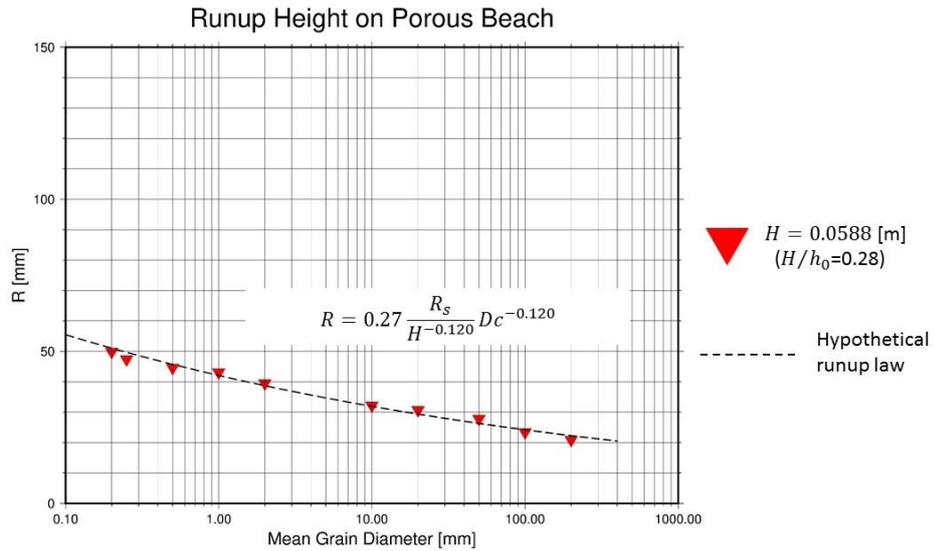
Figure 6.13 Runup law for a 1:20 porous beach

6.5   Wave runup on porous layers
6.5.1   Numerical setup

In this section, the parallelogram porous media is examined. The schematic diagram of the computational domain is presented in Figure 6.14. The porous media was placed at x = 2.0, and the slope scale was 1:20. The wave H = 0.0588 [m] was generated at the left end by the piston type wavemaker. The porosity of the porous layers was fixed at 0.49, and the mean grain size ranged from 0.20 mm to 200.0 mm. The thickness of the porous layers is varied at 7.5 cm, 20.0 cm, and 40.0 cm. The highest point of the flow at the water-porous boundary was defined as the runup hight. The numerical parameters are listed in Table 6.3.

145
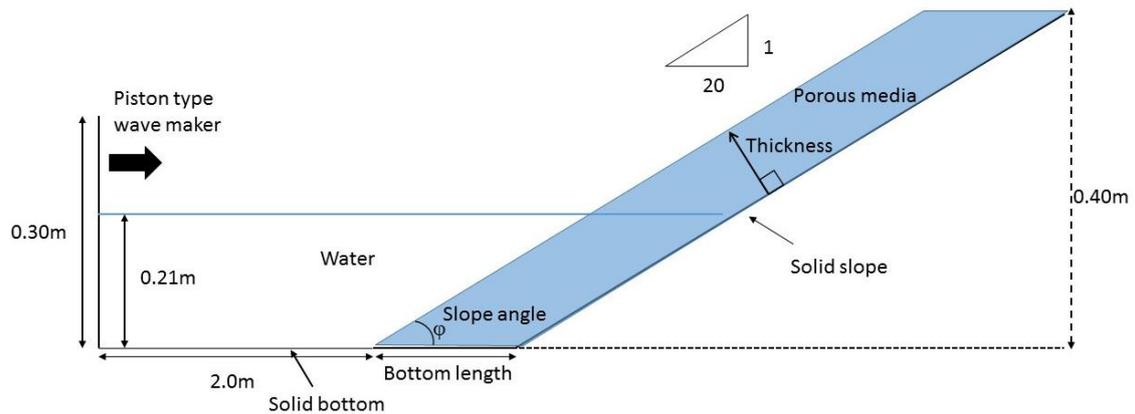
Figure 6.14 Setting of a 1:20 porous layers flume

Table 6.3 Computational parameters for wave runup on 1:20 porous layers

Parameters	Value
Diameter of particles	0.005 m
Initial particle spacing	0.005 m
Smoothing length	0.0085 m
Initial time step	0.00025 sec
Courant number	0.2
Smagorinsky constant	0.1
Combination ratio of the source term	0.97
Mean grain diameter of porous media	0.20 mm, 0.25 mm, 0.50 mm, 1.0 mmm, 2.0 mm, 10.0 mm, 20.0 mm, 30.0 mm, 40.0 mm, 50.0 mm, 100.0 mm, 200.0 mm
Bottom length of porous layers	150 cm, 400 cm, 800 cm
Thickness of porous layers	7.5 cm, 20.0 cm, 40.0 cm

6.5.2 Results and analysis

Figures 6.15 and 6.16 describe the snapshots of solitary wave runup on 7.5-cm thick porous layers, with the mean grain size Dc = 1.0 [mm] and 0.25 [mm], respectively. In Figure 6.15, the wave began to break while running up the porous layers at $t = 5.50$ [s], and it reached the highest point at $t = 8.60$ [s]. Some fluid particles plunged into the porous layers when the grain size is 1.0 mm. In Figure 6.16 (a), the wave broke at $t = 5.5$ [s] with Dc = 0.25 [mm], and the shape of the wave was nearly the same as the one with Dc = 1.0

146

[mm] in Figure 6.15 (a). Although the pressure around $x = 3.5$ dropped due to wave breaking, the overall pressure fields were acceptable. This pressure fluctuation is transients, which does not affect the overall wave evolution. It disappeared when the runup height was observed in Figure 6.16 (b).
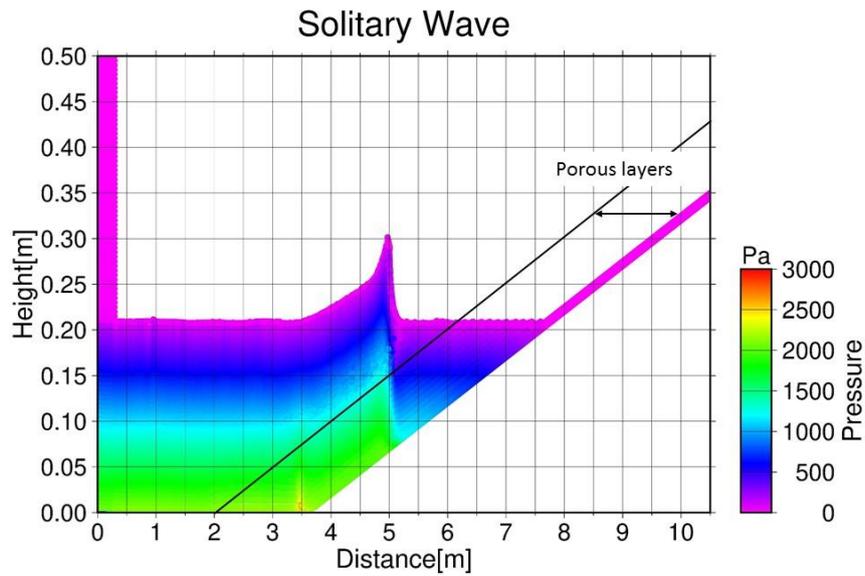
(a) $t = 5.50$ [s]
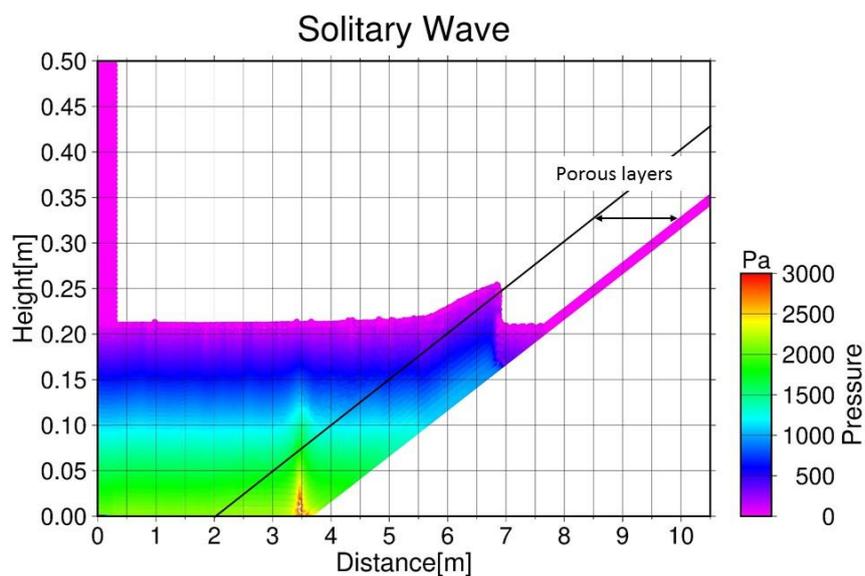
(b) $t = 8.60$ [s]

Figure 6.15 Wave runup on 7.5-cm thick porous layers with Dc = 1.0 [mm]

Solitary Wave

(a) $t = 5.50$ [s]

Solitary Wave
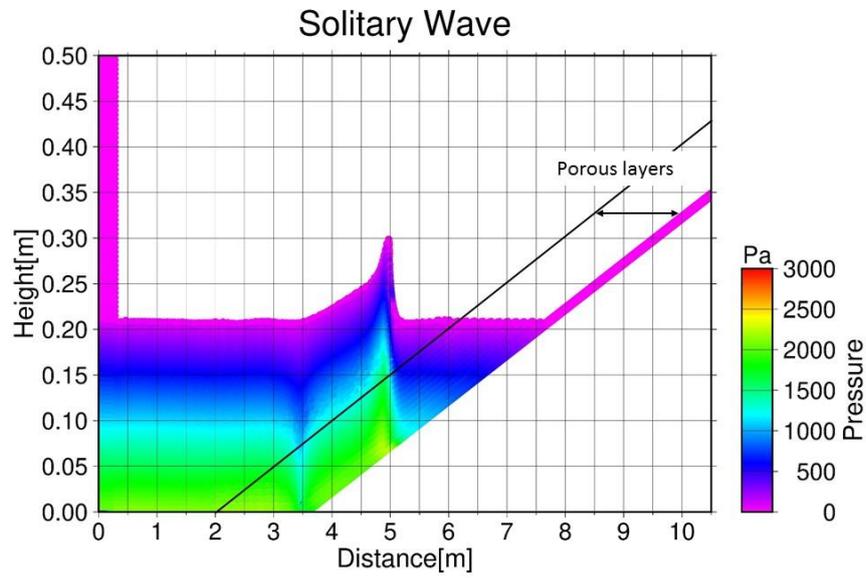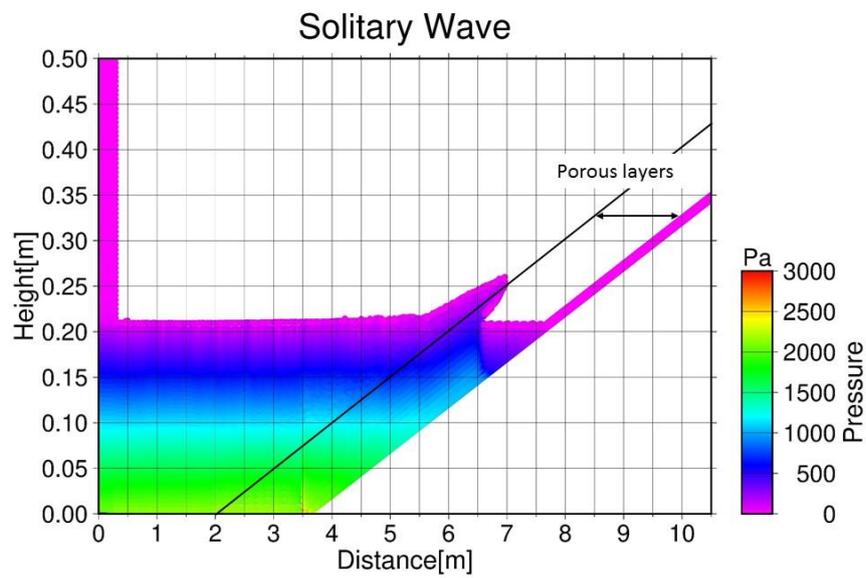
(b) $t = 8.60$ [s]

Figure 6.16 Wave runup on 7.5-cm thick porous layers with Dc = 0.25 [mm]

Figure 6.17 compares the runup height on the porous layers of three different thickness

cases with the various mean grain sizes of the porous media. Notably, the horizontal axis

is logarithmic. Similar to the results of nonbreaking wave runup on porous layers, runup height decreases nearly linearly with increasing logarithm of grain size. The maximum runup height obtained at Dc = 0.20 [mm] is significantly smaller than the runup height on a 1:20 solid slope. Nearly the same runup height was obtained in the three different thickness cases although the mean grain size became smaller. This result is different from the trend of nonbreaking wave runup on porous layers as discussed previously in Section 5.5.2.
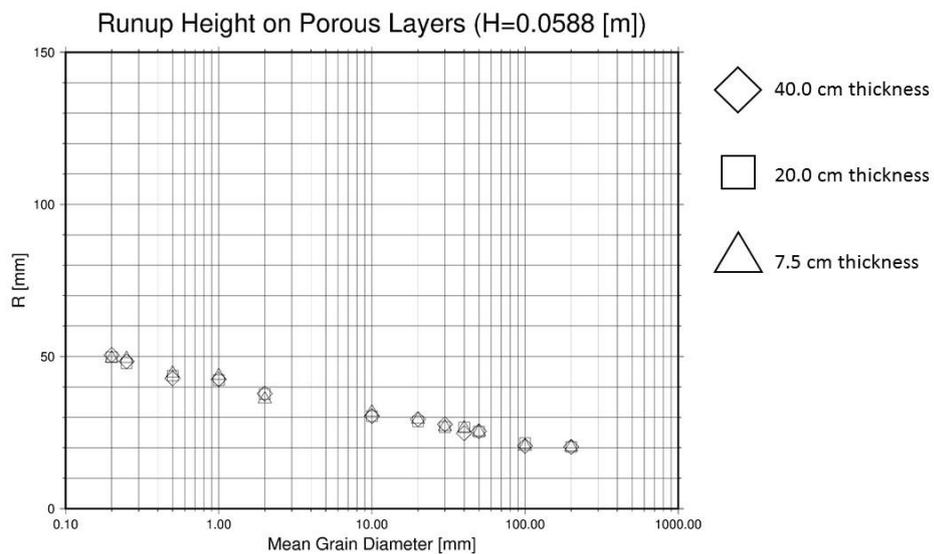
Figure 6.17 Runup height on 1:20 porous layers

Figure 6.18 describes the velocity fields of the wave when the 7.5-cm thick porous media with Dc = 10.0 [mm] is placed. The velocity of fluid particles in the left half of the wave crest pointed lower rightward and upper rightward in the right half of the wave in Figure 6.18 (a). At t = 5.50 [s], the wave began to break and showed similar velocity fields of breaking waves running on a solid slope as those presented by Lo and Shao (2002). After breaking, the fluid particles rapidly lost their velocity due to frictional force from the

149

porous layers (Figure 6.18 (b)). When the runup height was observed at $t = 8.60$ [s], the velocity of fluid particles in both the pure water and the porous regions was nearly zero. The velocity fields in the 40.0-cm thick layers are shown in Figure 6.19. Similar velocity fields were obtained during the runup process. Fluid particles lost much of their velocity while breaking, and they could not propagate freely inside porous media as they could in nonbreaking wave cases.
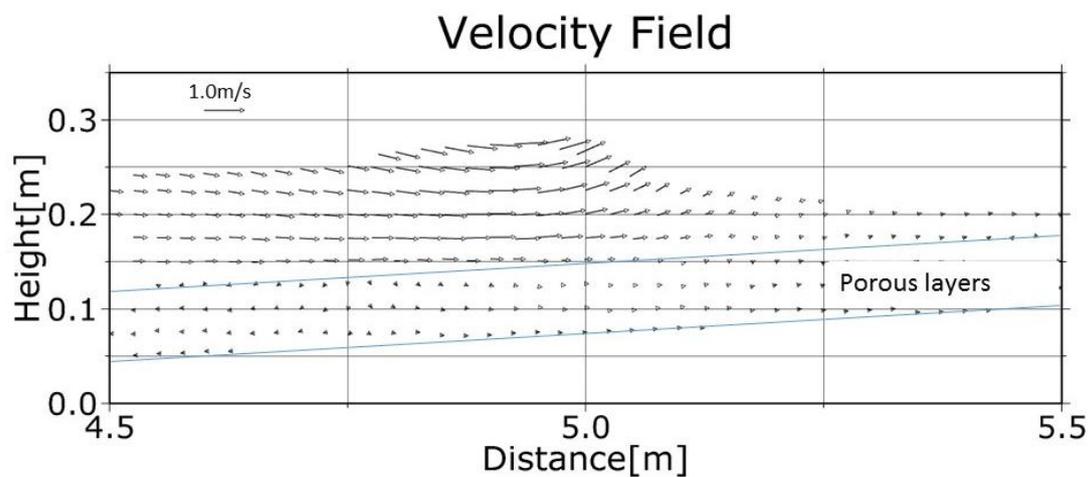
(a) $t = 5.50$ [s]
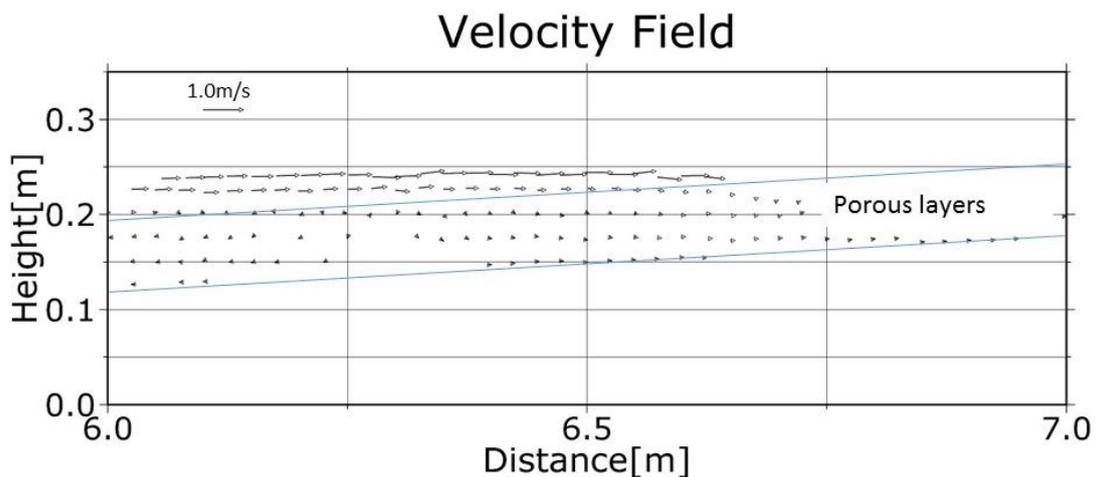
(b) $t = 7.00$ [s]

(c) t = 8.60 [s]
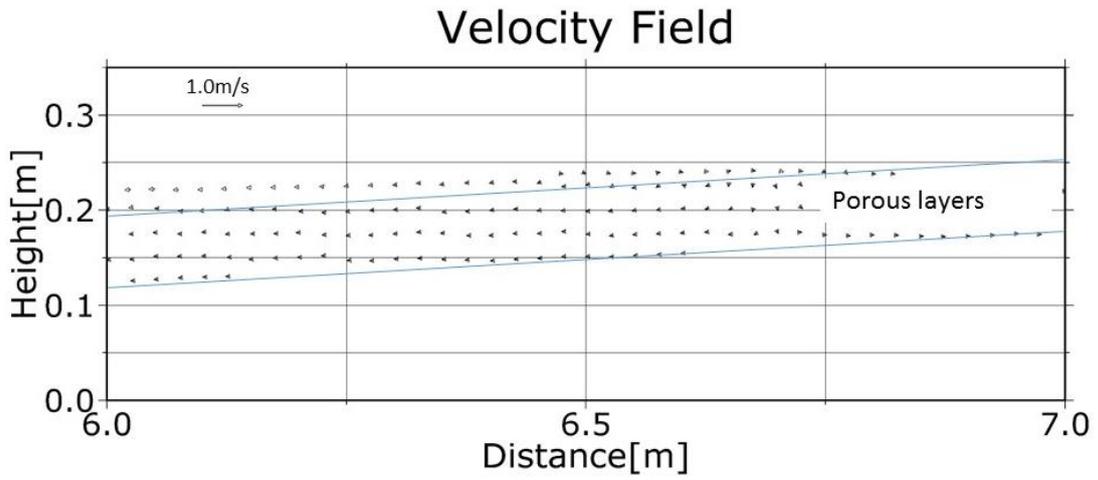
Figure 6.18 Velocity fields of wave running on 7.5-cm thick porous layers with Dc = 10.0 [mm]

(a) t = 5.50 [s]

151

Velocity Field

(b) $t = 7.00$ [s]

Velocity Field

(c) $t = 7.75$ [s]
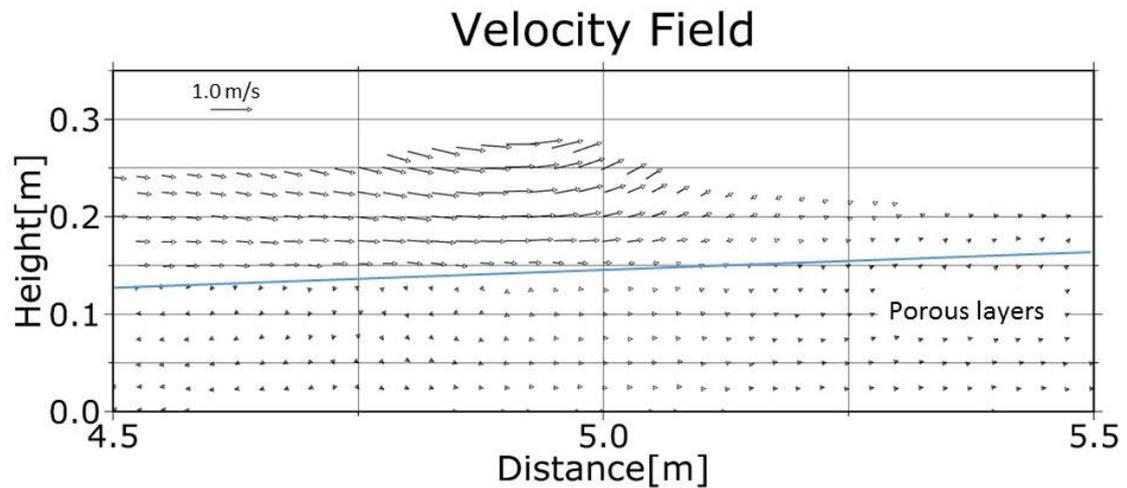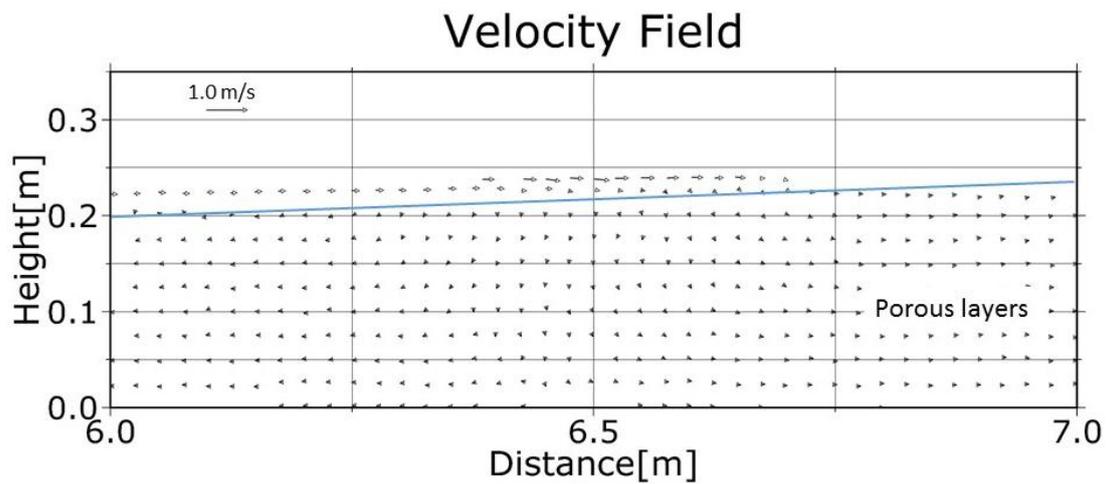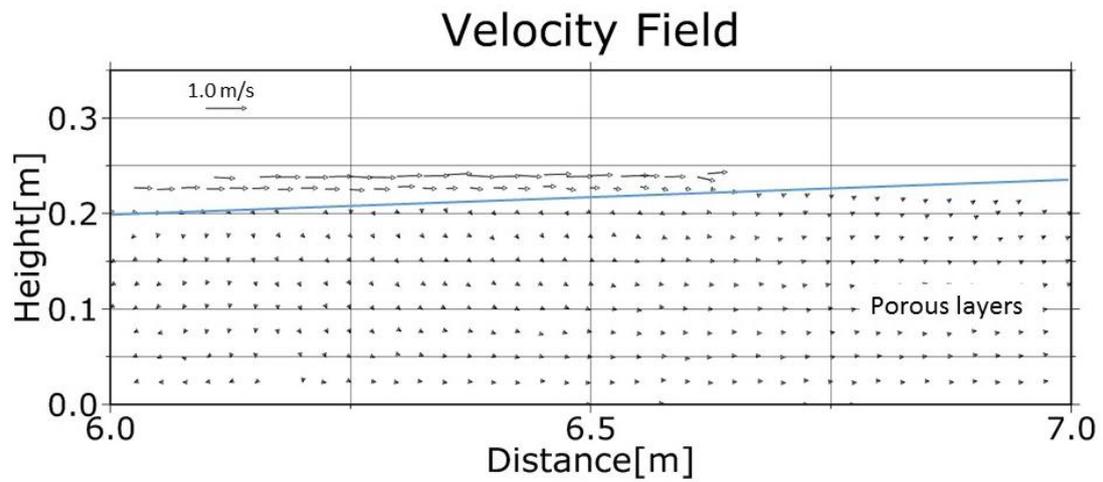
Figure 6.19 Velocity fields of wave running on 40.0-cm thick porous layers with Dc = 10.0 [mm]

Chapter 7   Conclusions

7.1   Conclusions

7.1.1   Development of the ISPH model for porous flows

This study presents an ISPH model that can simulate porous flows. The main developments are threefold:

(1) Dummy particles were used to describe porous media. Each particle has porosity information, and the same values of mass and density as fluid particles are given to porous particles.

(2) A new water-porous interface was proposed. Fluid particle porosity is determined by the amount of porous particles occupying the support domain of a target fluid particle. The porosity of fluid particles is defined linearly at the water-porous boundary; thus, a transition zone is not required in the present ISPH model. The proposed interface can be applied to various shapes of porous media.

(3) A new free surface condition was proposed. In violent porous flow simulations, particle spacing varies depending on whether fluid particles exist in a porous region or a pure fluid region. The new condition considers this spacing variation by updating the reference density of a target particle at each time step in a simulation. Free surface particles are correctly identified wherever fluid particles are.

In the present ISPH model, the apparent density method was adopted to reproduce the solid skeleton of porous structures. Although apparent density is an existing method, there are three differences in the present ISPH model from past studies. Firstly, in the past studies, background points were given porosity information and a transition zone was established at the water-porous boundary. The present model is superior in terms of the

flexibility of porous media implementation. Secondly, in the past studies, smoothing length was varied depending on porosity. Varied smoothing length can lead to an inconsistent summation of physical properties of two close particles around the water-porous boundary. In the present study, smoothing length is fixed regardless of porosity, and the symmetry principle is satisfied. Finally, the PPE was modified by combining the HS term and the standard source term in this study. Smooth and continuous pressure fields can be obtained owing to the hybrid source term. It is uncertain that satisfactory pressure was obtained in past studies since pressure fields were not necessarily presented.

The presented model was validated through the simulation of dam-break flow with a porous block. The simulated free surface agreed strongly with the experiment data. Reasonable and continuous pressure fields were obtained. The present schemes mentioned above worked successfully and the capability for porous flow simulations was validated.

7.1.2 Numerical treatments in SPH simulations

The third-order B-spline kernel and the standard source term have been conventionally used in the SPH simulations. Meanwhile, the Wendland kernel and the hybrid source term have been developed in the past a few decades. The optimal choice of kernel function and source term was examined in solitary wave simulations. As regards pressure fields, the Wendland kernel yielded more accurate pressure than the B-spline kernel. This trend was more dominant for breaking waves than for nonbreaking waves since pressure fields are complex in a breaking process, and the B-spline is not robust enough to simulate breaking waves. The hybrid source term is capable of eliminating pressure fluctuations and

smoothing pressure fields. In terms of wave runup, the hybrid source term provided consistent runup height results in the nonbreaking wave cases. For breaking waves, runup height was underestimated by both the standard source term and the hybrid source term. Accordingly, runup height is slightly closer to the analytical value when the standard source term is used. The above findings on pressure and runup height affirm that using the Wendland kernel and the hybrid source term is the optimal choice.

7.1.3   Simulations of solitary waves on soil beaches

Solitary wave runup on permeable beaches was simulated. Two different porous slopes were considered: triangle and parallelogram porous structures.

For nonbreaking waves, runup height decreased nearly linearly for porous media with increasing logarithm of grain size. Fluid particles cannot move into a porous region but slide on a permeable slope if the mean grain diameter is sufficiently small. Although porous media worked as if it were a solid wall, runup height could not reach the runup height on a solid slope due to frictional forces from a permeable slope. With large mean grain size, runup height was lower in the thickest porous layers case than the thin porous layers cases. This is because fluid particles can propagate inside the porous media, and they occupy the inner space of the porous structure. Few fluid particles consequently stayed around the water-porous boundary. This phenomenon happened when the mean grain size was larger than 40.0 mm for the wave $H = 0.03423$ [m] and larger than 20.0 mm for the wave $H = 0.0525$ [m]. For nonbreaking waves, the shape and thickness of porous media and the mean grain size can be the essential factors to determine runup height.

Similar to nonbreaking waves, runup height of breaking solitary waves decreased nearly linearly as the mean grain diameter of porous media became logarithmically larger. However, nearly the same runup height was observed in any thickness of parallelogram porous layers, even with large grain size. This is because the thickness of porous media does not affect a wave breaking process, and the velocity of fluid particles during breaking is lost in the same wave regardless of the thickness of porous structures. For breaking waves, the mean grain diameter of porous media predominantly determines runup height on permeable slopes.

From the simulation results, the runup height on permeable beaches can be estimated as

$$R = 0.61 \frac{R_s}{H^{-0.052}} Dc^{-0.052} \tag{7.1.1}$$

in a 1:2.08 scale and as

$$R = 0.27 \frac{R_s}{H^{-0.120}} Dc^{-0.120} \tag{7.1.2}$$

in a 1:20 scale.

7.2 Future work
7.2.1 Turbulence model

Turbulence around and inside porous media is of great interest in SPH simulations. As previously mentioned in Chapter 2, some experiments imply that it is not negligible. In this study, the original SPS turbulence model was combined with the present ISPH model. Nevertheless, the SPS turbulence model did not affect the simulation results and did not make significant differences. The particle diameter in this study is 0.005 m, and the

resolution is small enough to pass through sub-particle scale filtering. An improved SPS is needed to simulate the turbulence of violent porous flows.

7.2.2 Runup height on a solid slope

While accurate pressure fields can be obtained both in pure fluid and porous flows owing to the hybrid source term, runup height on a solid wall tends to be overestimated in nonbreaking waves and underestimated in breaking waves. To estimate runup height more accurately, further improvements on the present model are necessary. One possible solution is to modify the pressure gradient. The pressure gradient in the present ISPH model is obtained by the sum of two close particles' pressure only. This gradient may lead to numerical errors in integral interpolation. The pressure gradient can be modified through, for example, Tayler series expansion (Khayyer et al., 2017). Another solution is to eliminate artificial frictional force from a solid boundary. A solid slope is assumed to be smooth in simulations, but there may be unexpected friction force (Tan et al., 2015). Runup height is expected to approach the analytical solution by minimizing this friction force.

7.2.3 Model applications

The present model was applied to simulations of a solitary wave propagating over permeable beaches. Although some relationship between runup height and permeability have been found, further simulations and analysis are necessary to estimate runup height more accurately. Taking advantage of the flexibility of the water-porous interface, it is expected that the present model can be applied to simulations of wave propagation through multiple structures that have different porosities. For instance, a conventional multilayer rubble-mound breakwater consists of some different porous materials. Using

the present model, the wave evolution will be examined. The wave overtopping and impact problem can be analysed since the hybrid source term yields accurate pressure fields. As for the natural resources to mitigate coastal disasters, flows around coastal vegetation can be simulated by the three-dimensional model. Simulations in three dimension is generally expensive, and thus parallel computing technique is required. In this thesis, sediment transport was not included to focus on wave motions. Simulations of moving porous materials can be performed by the two-phase ISPH model, where the two sets of particles describe both fluid and sediments. If the present ISPH is extended to multi-phase modelling, it will also be applicable for debris flow. Accordingly, the improved model can contribute to a better understanding of violent porous flow motions, and more accurate prediction of pressure and runup height of these flows. This contributions will help engineers to design more robust and effective coastal protections.

References

Akbari, H. (2014). Modified moving particle method for modeling wave interaction with multi layered porous structures. *Coastal engineering*, *89*, 1-19.

Akbari, H., & Namin, M. M. (2013). Moving particle method for modeling wave interaction with porous structures. *Coastal engineering*, *74*, 59-73.

Altomare, C., Crespo, A. J., Domínguez, J. M., Gómez-Gesteira, M., Suzuki, T., & Verwaest, T. (2015). Applicability of smoothed particle hydrodynamics for estimation of sea wave impact on coastal structures. *Coastal Engineering*, *96*, 1-12.

Altomare, C., Crespo, A. J., Rogers, B. D., Domínguez, J. M., Gironella, X., & Gómez-Gesteira, M. (2014). Numerical modelling of armour block sea breakwater with smoothed particle hydrodynamics. *Computers & Structures*, *130*, 34-45.

Asai, Mitsuteru, et al. (2012). "A stabilized incompressible SPH method by relaxing the density invariance condition." *Journal of Applied Mathematics* 2012.

Asai, M., Fujimoto, K., Tanabe, S., & Beppu, M. (2013). Slip and No-Slip Boundary Treatment for Particle Simulation Model with Incompatible Step-Shaped Boundaries by Using a Vertual Maker. *Transactions of JSCES*, *2013*, 20130011-20130011.

Ataie-Ashtiani, B., Shobeyri, G., & Farhadi, L. (2008). Modified incompressible SPH method for simulating free surface problems. *Fluid Dynamics Research*, *40*(9), 637.

Beckmann, B., Schicktanz, K., Reischl, D., & Curbach, M. (2012). DEM simulation of concrete fracture and crack evolution. *Structural Concrete*, *13*(4), 213-220.

Berger, M. J. (1982). *Adaptive mesh refinement for hyperbolic partial differential equations* (No. STAN-CS-82-924). STANFORD UNIV CA DEPT OF COMPUTER SCIENCE.

Bonet, J., & Lok, T. S. (1999). Variational and momentum preservation aspects of smooth particle hydrodynamic formulations. *Computer Methods in applied mechanics and engineering*, *180*(1-2), 97-115.

Borthwick, A. G. L., Ford, M., Weston, B. P., Taylor, P. H., & Stansby, P. K. (2006, September). Solitary wave transformation, breaking and run-up at a beach. In *Proceedings of the Institution of Civil Engineers-Maritime Engineering* (Vol. 159, No. 3, pp. 97-105). Thomas Telford Ltd.

Boussinesq, J. (1871). Théorie de l'intumescence liquide appelée onde solitaire ou de translation se propageant dans un canal rectangulaire. *CR Acad. Sci. Paris*, *72*(755-759), 1871.

Boussinesq, J. (1872). Théorie des ondes et des remous qui se propagent le long d'un canal rectangulaire horizontal, en communiquant au liquide contenu dans ce canal des vitesses sensiblement pareilles de la surface au fond. *Journal de mathématiques pures et appliquées*, 55-108.

Brinkman, H. C. (1949). A calculation of the viscous force exerted by a flowing fluid on a dense swarm of particles. *Flow, Turbulence and Combustion*, *1*(1), 27.

Burcharth, H. F., & Hughes, S. A. (2003). Types and functions of coastal structures. In *Coastal Engineering Manual*. Coastal Engineering Research Center.

Carrier, G. F., & Greenspan, H. P. (1958). Water waves of finite amplitude on a sloping beach. *Journal of Fluid Mechanics*, *4*(1), 97-109.

160

Chan, R. K. C., & Street, R. L. (1970). A computer study of finite-amplitude water waves. *Journal of Computational Physics*, 6(1), 68-94.

Chang, Y. H., Hwang, K. S., & Hwung, H. H. (2009). Large-scale laboratory measurements of solitary wave inundation on a 1: 20 slope. *Coastal engineering*, *56*(10), 1022-1034.

Courant, R., Friedrichs, K., & Lewy, H. (1928). Über die partiellen Differenzengleichungen der mathematischen Physik. *Mathematische annalen*, *100*(1), 32-74.

Cummins, S. J., & Rudman, M. (1999). An SPH projection method. *Journal of computational physics*, *152*(2), 584-607.

Cundall, P. A. (1971). A computer model for simulating progressive, large-scale movement in blocky rock system. In *Proceedings of the International Symposium on Rock Mechanics, 1971*.

Cundall, P. A., & Strack, O. D. (1979). A discrete numerical model for granular assemblies. *geotechnique*, *29*(1), 47-65.

DESA, U. (2018). World urbanization prospects: 2018. *Nairobi (Kenya): United Nations Department for Economic and Social Affairs*.

Dao, M. H., Xu, H., Chan, E. S., & Tkalich, P. (2013). Modelling of tsunami-like wave run-up, breaking and impact on a vertical wall by SPH method. *Natural Hazards and Earth System Sciences*, *13*(12), 3457.

Darcy, H. P. G. (1856). *Les Fontaines publiques de la ville de Dijon. Exposition et application des principes à suivre et des formules à employer dans les questions de distribution d'eau, etc*. V. Dalamont.

Di Renzo, A., & Di Maio, F. P. (2004). Comparison of contact-force models for the simulation of collisions in DEM-based granular flow codes. *Chemical engineering science*, *59*(3), 525-541.

Didier, E., Neves, D. R. C. B., Martins, R., & Neves, M. G. (2014). Wave interaction with a vertical wall: SPH numerical and experimental modeling. *Ocean engineering*, *88*, 330-341.

Ebersole, B. A., Westerink, J. J., Bunya, S., Dietrich, J. C., & Cialone, M. A. (2010). Development of storm surge which led to flooding in St. Bernard Polder during Hurricane Katrina. *Ocean Engineering*, 37(1), 91-103.

Farhadi, A., Ershadi, H., Emdad, H., & Rad, E. G. (2016). Comparative study on the accuracy of solitary wave generations in an ISPH-based numerical wave flume. *Applied Ocean Research*, *54*, 115-136.

Forchheimer, P. (1901). Wasserbewegung durch boden. *Z. Ver. Deutsch, Ing.*, *45*, 1782-1788.

Fu, L., & Jin, Y. C. (2018). Macroscopic particle method for channel flow over porous bed. *Engineering Applications of Computational Fluid Mechanics*, *12*(1), 13-27.

Gingold, R. A., & Monaghan, J. J. (1977). Smoothed particle hydrodynamics: theory and application to non-spherical stars. *Monthly notices of the royal astronomical society*, *181*(3), 375-389.

Goda, Y., Kishara, Y., & Kamiyama, Y. (1975). Laboratory investigation on the overtopping rate of seawalls by irregular waves. *Report of the Port and Harbour Research Institute*, vol 14, nr. 4.

Goring, D. G. (1978). Tsunamis--the propagation of long waves onto a shelf. (Doctoral dissertation, California Institute of Technology)

Gotoh (2018) Particle methods. Morikita, Japan (in Japanese)

Gotoh, H. (2001). Sub-particle-scale turbulence model for the MPS method-Lagrangian flow model for hydraulic engineering. *Computational Fluid Dynamics Jour*, *9*(4), 339-347.

Gotoh, H., & Sakai, T. (1999). Lagrangian simulation of breaking waves using particle method. *Coastal Engineering Journal*, *41*(03n04), 303-326.

Gotoh, H., & Sakai, T. (2006). Key issues in the particle method for computation of wave breaking. *Coastal Engineering*, *53*(2-3), 171-179.

Gotoh, H., Ikari, H., Memita, T., & Sakai, T. (2005). Lagrangian particle method for simulation of wave overtopping on a vertical seawall. *Coastal Engineering Journal*, *47*(02n03), 157-181.

Gotoh, H., Shao, S., & Memita, T. (2004). SPH-LES model for numerical investigation of wave interaction with partially immersed breakwater. *Coastal Engineering Journal*, *46*(01), 39-63.

Gui, Q., Dong, P., & Shao, S. (2015, a). Numerical study of PPE source term errors in the incompressible SPH models. *International Journal for Numerical Methods in Fluids*, *77*(6), 358-379.

Gui, Q., Dong, P., Shao, S., & Chen, Y. (2015, b). Incompressible SPH simulation of wave interaction with porous structure. *Ocean Engineering*, *110*, 126-139.

Gui, Q., Shao, S., & Dong, P. (2014). Wave impact simulations by an improved ISPH model. *Journal of waterway, port, coastal, and ocean engineering*, *140*(3), 04014005.

Hall Jr, J. V., & Watts, G. M. (1953). *Laboratory investigation of the vertical rise of solitary waves on impermeable slopes* (No. TM33). ARMY COASTAL ENGINEERING RESEARCH CENTER WASHINGTON DC.

Harlow, F. H. (1964). The particle-in-cell computing method for fluid dynamics. *Methods Comput. Phys.*, *3*, 319-343.

Harlow, F. H., & Welch, J. E. (1965). Numerical calculation of time‑dependent viscous incompressible flow of fluid with free surface. *The physics of fluids*, 8(12), 2182-2189.

Higuera, P., Lara, J. L., & Losada, I. J. (2014). Three-dimensional interaction of waves and porous coastal structures using OpenFOAM®. Part I: Formulation and validation. *Coastal Engineering*, *83*, 243-258.

Hirt, C. W., & Nichols, B. D. (1981). Volume of fluid (VOF) method for the dynamics of free boundaries. *Journal of computational physics*, 39(1), 201-225.

Hsiao, S. C., Hsu, T. W., Lin, T. C., & Chang, Y. H. (2008). On the evolution and run-up of breaking solitary waves on a mild sloping beach. *Coastal Engineering*, *55*(12), 975-988.

Hsu, T. J., Sakakiyama, T., & Liu, P. L. F. (2002). A numerical model for wave motions and turbulence flows in front of a composite breakwater. *Coastal Engineering*, 46(1), 25-50.

Huang, C. J., Chang, H. H., & Hwung, H. H. (2003). Structural permeability effects on the interaction of a solitary wave and a submerged breakwater. *Coastal engineering*, 49(1), 1-24.

Huang, C. J., Shen, M. L., & Chang, H. H. (2008). Propagation of a solitary wave over rigid porous beds. *Ocean Engineering*, 35(11), 1194-1202.

Hughes, S. A. (2004). Estimation of wave run-up on smooth, impermeable slopes using the wave momentum flux parameter. *Coastal Engineering*, *51*(11-12), 1085-1104.

Hwang, S. C., Khayyer, A., Gotoh, H., & Park, J. C. (2014). Development of a fully Lagrangian MPS-based coupled method for simulation of fluid–structure interaction problems. *Journal of Fluids and Structures*, *50*, 497-511.

Iso, E. (2017). 14688-1: 2017: Geotechnical investigation and testing–Identification and classification of soil–Part 1: Identification and description. *International Organization for Standardization, Geneva*.

Jasak, H., & Gosman, A. D. (2000). Automatic resolution control for the finite-volume method, part 2: Adaptive mesh refinement and coarsening. *Numerical Heat Transfer: Part B: Fundamentals*, *38*(3), 257-271.

Jasak, H., & Tukovic, Z. (2006). Automatic mesh motion for the unstructured finite volume method. *Transactions of FAMENA*, *30*(2), 1-20.

Karunarathna, S. A. S. A., & Lin, P. (2006). Numerical simulation of wave damping over porous seabeds. *Coastal Engineering*, 53(10), 845-855.

Katell, G., & Eric, B. (2002). Accuracy of solitary wave generation by a piston wave maker. *Journal of Hydraulic Research*, *40*(3), 321-331.

Kawasaki, K. (1999). Numerical simulation of breaking and post-breaking wave deformation process around a submerged breakwater. *Coastal Engineering Journal*, *41*(3-4), 201-223.

Khayyer, A., & Gotoh, H. (2009). Modified moving particle semi-implicit methods for the prediction of 2D wave impact pressure. *Coastal Engineering*, *56*(4), 419-440.

Khayyer, A., & Gotoh, H. (2010). A higher order Laplacian model for enhancement and stabilization of pressure calculation by the MPS method. *Applied Ocean Research*, *32*(1), 124-131.

Khayyer, A., & Gotoh, H. (2011). Enhancement of stability and accuracy of the moving particle semi-implicit method. *Journal of Computational Physics*, *230*(8), 3093-3118.

Khayyer, A., Gotoh, H., & Shao, S. (2008). Corrected incompressible SPH method for accurate water-surface tracking in breaking waves. *Coastal Engineering*, *55*(3), 236-250.

Khayyer, A., Gotoh, H., & Shao, S. (2009). Enhanced predictions of wave impact pressure by improved incompressible SPH methods. *Applied Ocean Research*, *31*(2), 111-131.

Khayyer, A., Gotoh, H., Shimizu, Y., & Gotoh, K. (2017). On enhancement of energy conservation properties of projection-based particle methods. *European Journal of Mechanics-B/Fluids*, *66*, 20-37.

Khayyer, A., Gotoh, H., Shimizu, Y., Gotoh, K., Falahaty, H., & Shao, S. (2018). Development of a projection-based SPH method for numerical wave flume with porous media of variable porosity. *Coastal Engineering*, *140*, 1-22.

Kim, N. H., & Ko, H. S. (2008). Numerical simulation on solitary wave propagation and run-up by SPH method. *KSCE Journal of Civil Engineering*, *12*(4), 221-226.

Koh, C. G., et al. "Modelling of liquid sloshing with constrained floating baffle." *Computers & Structures* 122 (2013): 270-279.

Koshizuka, S., & Oka, Y. (1996). Moving-particle semi-implicit method for fragmentation of incompressible fluid. *Nuclear science and engineering*, *123*(3), 421-434.

Koshizuka, S., Nobe, A., & Oka, Y. (1998). Numerical analysis of breaking waves using the moving particle semi‐implicit method. *International Journal for Numerical Methods in Fluids*, *26*(7), 751-769.

Koshizuka, S., Takano, N., & Oka, Y. (1995). Numerical analysis of deterioration phenomena in heat transfer to supercritical water. *International Journal of Heat and Mass Transfer*, *38*(16), 3077-3084.

Kumar, P., Yang, Q., Jones, V., & McCue-Weil, L. (2015). Coupled SPH-FVM simulation within the OpenFOAM framework. *Procedia Iutam*, *18*, 76-84.

Laitone, E. V. (1963). Higher order approximation to nonlinear waves and the limiting heights of Cnoidal, Solitary and Stokes' waves. *Beach Erosion Board, US Department of the Army, Corps of Engineers, Technical Memorandum*, (133).

Lara, J. L., Garcia, N., & Losada, I. J. (2006). RANS modelling applied to random wave interaction with submerged permeable structures. *Coastal Engineering*, 53(5), 395-417.

Lara, J. L., Losada, I. J., Maza, M., & Guanche, R. (2011). Breaking solitary wave evolution over a porous underwater step. *Coastal Engineering*, 58(9), 837-850.

Lee, E. S., Moulinec, C., Xu, R., Violeau, D., Laurence, D., & Stansby, P. (2008). Comparisons of weakly compressible and truly incompressible algorithms for the SPH mesh free particle method. *Journal of computational Physics*, *227*(18), 8417-8436.

Li, Y., & Raichlen, F. (2001). Solitary wave runup on plane slopes. *Journal of Waterway, Port, Coastal, and Ocean Engineering*, *127*(1), 33-44.

Lin, P., Chang, K. A., & Liu, P. L. F. (1999). Runup and rundown of solitary waves on sloping beaches. *Journal of waterway, port, coastal, and ocean engineering*, *125*(5), 247-255.

Liu, C., & Hu, C. (2018). An adaptive multi-moment FVM approach for incompressible flows. *Journal of Computational Physics*, *359*, 239-262.

Liu and Liu (2003) Smoothed Particle Hydrodynamics: a meshfree particle method. World Scientific, Singapore

Liu, P. L. F., Lin, P., Chang, K. A., & Sakakiyama, T. (1999). Numerical modeling of wave interaction with porous structures. *Journal of waterway, port, coastal, and ocean engineering*, *125*(6), 322-330.

Lo, E. Y., & Shao, S. (2002). Simulation of near-shore solitary wave mechanics by an incompressible SPH method. *Applied Ocean Research*, *24*(5), 275-286.

Lucy, L. B. (1977). A numerical approach to the testing of the fission hypothesis. *The astronomical journal*, *82*, 1013-1024.

Martinelli, M., & Rohe, A. (2015). Modelling fluidisation and sedimentation using material point method. In *1st Pan-American Congress on Computational Mechanics*.

Matsubara H., Iribe T., & Iraha S. (2010). A Consideration on Accuracy of the Approximate Differentiation in the Particle Method and Multidimensional Moving Least Squares Method with Constraint. *Proceeding of JSCE*, *A*, *66*(4), 723-736.

Memarzadeh, R., & Hejazi, K. (2012). ISPH numerical modeling of nonlinear wave run-up on steep slopes. *Journal of the Persian Gulf, 3*(10), 17-26.

Monaghan, J. J. (1992). Smoothed particle hydrodynamics. *Annual review of astronomy and astrophysics*, *30*(1), 543-574.

Monaghan, J. J. (1994). Simulating free surface flows with SPH. *Journal of computational physics*, *110*(2), 399-406.

Monaghan, J. J., & Kos, A. (1999). Solitary waves on a Cretan beach. *Journal of waterway, port, coastal, and ocean engineering*, *125*(3), 145-155.

Monaghan, J. J., & Kos, A. (2000). Scott Russell's wave generator. *Physics of Fluids*, *12*(3), 622-630.

Monaghan, J. J., & Lattanzio, J. C. (1985). A refined particle method for astrophysical problems. *Astronomy and astrophysics*, *149*, 135-143.

Mori, N., Takahashi, T., Yasuda, T., & Yanagisawa, H. (2011). Survey of 2011 Tohoku earthquake tsunami inundation and run‐up. *Geophysical research letters*, *38*(7).

Oumeraci, H. (1994). Review and analysis of vertical breakwater failures—lessons learned. *Coastal Engineering*, 22(1-2), 3-29.

Pahar, G., & Dhar, A. (2016). Modeling free-surface flow in porous media with modified incompressible SPH. *Engineering Analysis with Boundary Elements*, *68*, 75-85.

Pahar, G., & Dhar, A. (2017). Numerical modelling of free-surface flow-porous media interaction using divergence-free moving particle semi-implicit method. *Transport in Porous Media*, *118*(2), 157-175.

Peng, C., Xu, G., Wu, W., Yu, H. S., & Wang, C. (2017). Multiphase SPH modeling of free surface flow in porous media with variable porosity. *Computers and Geotechnics*, *81*, 239-248.

Rayleigh, L. (1876). On waves. *Phil. Mag.*, *1*, 257-259.

Ren, B., Jin, Z., Gao, R., Wang, Y. X., & Xu, Z. L. (2014, a). SPH-DEM modeling of the hydraulic stability of 2D blocks on a slope. *Journal of Waterway, Port, Coastal, and Ocean Engineering*, *140*(6), 04014022.

Ren, B., Wen, H., Dong, P., & Wang, Y. (2014, b). Numerical simulation of wave interaction with porous structures using an improved smoothed particle hydrodynamic method. *Coastal Engineering*, *88*, 88-100.

Ren, B., Wen, H., Dong, P., & Wang, Y. (2016). Improved SPH simulation of wave motions and turbulent flows through porous media. *Coastal Engineering*, *107*, 14-27.

Rogallo, R. S., & Moin, P. (1984). Numerical simulation of turbulent flows. *Annual review of fluid mechanics*, *16*(1), 99-137.

Rogers, B. D., Dalrymple, R. A., & Stansby, P. K. (2010). Simulation of caisson breakwater movement using 2-D SPH. *Journal of Hydraulic Research*, *48*(S1), 135-141.

Sakai, T., Mizutani, T., Tanaka, H., & Tada, Y. (1987). Vortex formation in plunging breaker. In *Coastal Engineering 1986* (pp. 711-723).

Sakakiyama, T., & Liu, P. L. F. (2001). Laboratory experiments for wave motions and turbulence flows in front of a breakwater. *Coastal Engineering*, 44(2), 117-139.

Savage, R. P., & Fairchild, J. C. (1953). *Laboratory study of wave energy losses by bottom friction and percolation* (No. CERC-TM-31). COASTAL ENGINEERING RESEARCH CENTER VICKSBURG MS.

Sawaragi, T., & Deguchi, I. (1993). Waves on permeable layers. In *Coastal Engineering 1992* (pp. 1531-1544).

Scott-Russell, J. (1844, September). Report on waves. In *Proc. Roy. Soc. Edinburgh* (Vol. 319, No. 1844).

Shadloo, M. S., Weiss, R., Yildiz, M., & Dalrymple, R. A. (2015). Numerical simulation of long wave runup for breaking and nonbreaking waves. *International Journal of Offshore and Polar Engineering*, *25*(01), 1-7.

Shao, S. (2010). Incompressible SPH flow model for wave interactions with porous media. *Coastal Engineering*, *57*(3), 304-316.

Shao, S., & Gotoh, H. (2005). Turbulence particle models for tracking free surfaces. *Journal of Hydraulic Research*, *43*(3), 276-289.

Shao, S., & Lo, E. Y. (2003). Incompressible SPH method for simulating Newtonian and non-Newtonian flows with a free surface. *Advances in water resources*, *26*(7), 787-800.

Shimizu, N. (2011). Coastal dykes and tsunami height in Taro, *The Association of Japanese Geographers*. (in Japanese)

Smagorinsky, J. (1963). General circulation experiments with the primitive equations: I. The basic experiment. *Monthly weather review*, *91*(3), 99-164.

Sollitt, C. K., & Cross III, R. H. (1972). *Wave reflection and transmission at permeable breakwaters* (No. 147). MASSACHUSETTS INST OF TECH CAMBRIDGE RALPH M PARSONS LAB FOR WATER RESOURCES AND HYDRODYNAMICS.

Sulisz, W. (1985). Wave reflection and transmission at permeable breakwaters of arbitrary cross-section. *Coastal Engineering*, *9*(4), 371-386.

Sulsky, D., Chen, Z., & Schreyer, H. L. (1994). A particle method for history-dependent materials. *Computer methods in applied mechanics and engineering*, *118*(1-2), 179-196.

Svendsen, I. A. (1974). *Cnoidal waves over a gently sloping bottom*. Institute of Hydrodynamics and Hydraulic Engineering.

Synolakis, C. E. (1986). *The runup of long waves* (Doctoral dissertation, California Institute of Technology).

Synolakis, C. E. (1987). The runup of solitary waves. *Journal of Fluid Mechanics*, *185*, 523-545.

Tan, L. W., & Chu, V. H. (2010). Wave runup simulations using Lagrangian blocks on Eulerian mesh. *Journal of Hydro-environment Research*, *3*(4), 193-200.

Tan, S. K., Cheng, N. S., Xie, Y., & Shao, S. (2015). Incompressible SPH simulation of open channel flow over smooth bed. *Journal of hydro-environment research*, *9*(3), 340-353.

Titov, V. V., & Synolakis, C. E. (1995). Modeling of breaking and nonbreaking long-wave evolution and runup using VTCS-2. *Journal of Waterway, Port, Coastal, and Ocean Engineering*, *121*(6), 308-316.

Tsuruta, N., Khayyer, A., & Gotoh, H. (2013). A short note on dynamic stabilization of moving particle semi-implicit method. *Computers & Fluids*, *82*, 158-164.

Valizadeh, A., & Rudman, M. (2017). A numerical approach for simulating flow through thin porous media. *European Journal of Mechanics-B/Fluids*, *65*, 31-44.

Violeau, D., & Leroy, A. (2015). Optimal time step for incompressible SPH. *Journal of Computational Physics*, *288*, 119-130.

Von Glasow, R., Jickells, T. D., Baklanov, A., Carmichael, G. R., Church, T. M., Gallardo, L., ... & Raine, R. (2013). Megacities and large urban agglomerations in the coastal zone: interactions between atmosphere, land, and marine ecosystems. *Ambio*, *42*(1), 13-28.

Wei, Y., Mao, X. Z., & Cheung, K. F. (2006). Well-balanced finite-volume model for long-wave runup. *Journal of Waterway, Port, Coastal, and Ocean Engineering*, *132*(2), 114-124.

Wendland, H. (1995). Piecewise polynomial, positive definite and compactly supported radial functions of minimal degree. *Advances in computational Mathematics*, *4*(1), 389-396.

Wu, Y. T., & Hsiao, S. C. (2013). Propagation of solitary waves over a submerged permeable breakwater. *Coastal Engineering*, *81*, 1-18.

Wu, Y. T., Yeh, C. L., & Hsiao, S. C. (2014). Three-dimensional numerical simulation on the interaction of solitary waves and porous breakwaters. *Coastal Engineering*, *85*, 12-29.

Wurjanto, A., & Kobayashi, N. (1993). Irregular wave reflection and runup on permeable slopes. *Journal of waterway, port, coastal, and ocean engineering*, *119*(5), 537-557.

Yasuhara, M. & Kaihotsu, I (1981). Reviews on Non-Darcy Flow in Porous Media. *Journal of Japanese Association of Groundwater Hydrology*, 23(2), 35-43.

Yeh, H., Francis, M., Peterson, C., Katada, T., Latha, G., Chadha, R. K., ... & Raghuraman, G. (2007). Effects of the 2004 great Sumatra tsunami: Southeast Indian coast. *Journal of waterway, port, coastal, and ocean engineering*, 133(6), 382-400

Yu, X., & Chwang, A. T. (1994). Wave motion through porous structures. *Journal of engineering mechanics*, *120*(5), 989-1008.

Zelt, J. A. (1991). The run-up of nonbreaking and breaking solitary waves. *Coastal Engineering*, *15*(3), 205-246.

Zhu, Y., Fox, P. J., & Morris, J. P. (1999). A pore‐scale numerical model for flow through porous media. *International journal for numerical and analytical methods in geomechanics*, *23*(9), 881-904.

del Jesus, M., Lara, J. L., & Losada, I. J. (2012). Three-dimensional interaction of waves and porous coastal structures: Part I: Numerical model formulation. *Coastal Engineering*, 64, 57-72.

van Gent, M. R. (1994). The modelling of wave action on and in coastal structures. *Coastal Engineering*, *22*(3-4), 311-339.

van Gent, M. R. A. (1995). Porous flow through rubble-mound material. *Journal of waterway, port, coastal, and ocean engineering*, *121*(3), 176-181.

van der Meer, J. W., Petit, H. A. H., Van den Bosch, P., Klopman, G., & Broekens, R. D. (1993). Numerical simulation of wave motion on and in coastal structures. In *Coastal Engineering 1992* (pp. 1772-1784).

Violeau, D., & Leroy, A. (2015). Optimal time step for incompressible SPH. *Journal of Computational Physics*, *288*, 119-130.

Özhan, E., & Shi-Igai, H. (1977). On the development of solitary waves on a horizontal bed with friction. *Coastal Engineering*, 1, 167-184.